Journal of Materials Chemistry A

ROYAL SOCIETY OF CHEMISTRY

REVIEW

View Article Online
View Journal | View Issue

Cite this: J. Mater. Chem. A, 2022, 10, 19466

Advances in studying interfacial reactions in rechargeable batteries by photoelectron spectroscopy

Ida Källquist, [a] Ronan Le Ruyet, [b] Haidong Liu, [b] Ronnie Mogensen, [b] Ming-Tao Lee, [b] Kristina Edström [b] and Andrew J. Naylor *[b]

Many of the challenges faced in the development of lithium-ion batteries (LIBs) and next-generation technologies stem from the (electro)chemical interactions between the electrolyte and electrodes during operation. It is at the electrode–electrolyte interfaces where ageing mechanisms can originate through, for example, the build-up of electrolyte decomposition products or the dissolution of metal ions. In pursuit of understanding these processes, X-ray photoelectron spectroscopy (XPS) has become one of the most important and powerful techniques in a large collection of available tools. As a highly surface-sensitive technique, it is often thought to be the most relevant in characterising the interfacial reactions that occur inside modern rechargeable batteries. This review tells the story of how XPS is employed in day-to-day battery research, as well as highlighting some of the most recent innovative *in situ* and *operando* methodologies developed to probe battery materials in ever greater detail. A large focus is placed not only on LIBs, but also on next-generation materials and future technologies, including sodium- and potassium-ion, multivalent, and solid-state batteries. The capabilities, limitations and practical considerations of XPS, particularly in relation to the investigation of battery materials, are discussed, and expectations for its use and development in the future are assessed.

Received 21st April 2022
Accepted 16th August 2022

DOI: 10.1039/d2ta03242b

rsc.li/materials-a

1 Introduction

1.1 Challenges for rechargeable batteries

While there are many well-established and reliable rechargeable battery technologies available such as the lead acid battery or nickel metal hydride battery, there is none as energy dense or powerful as the lithium-ion battery (LIB).[1] Since their

[a]Department of Physics and Astronomy, Uppsala University, Box 516, 75120 Uppsala, Sweden

[b]Department of Chemistry – Ångström Laboratory, Uppsala University, SE-75121 Uppsala, Sweden. E-mail: andy.naylor@kemi.uu.se

Dr Ida Källquist obtained her PhD from Uppsala University in 2022. Her research has been focused on the study of Li-ion battery interfaces using advanced spectroscopic methods. Some of her work includes studying the degradation mechanism in high-energy density cathode materials, as well as evaluating the effects of different electrolyte additives and coatings in order to improve the interfacial stability. In addition, she has worked on developing a methodology for studying solid/liquid interfaces of Li-ion batteries operando using APXPS.

Ronan Le Ruyet received is bachelor degree in material science at the University of Poitiers in 2013, subsequently he obtained a Master Erasmus Mundus-Materials for Energy Storage and Conversion (MESC) in 2016. He received his PhD degree in solid state chemistry and material science in 2020 at the Université de Picardie Jules Verne within the Laboratoire de Réactivité et Chimie des Solides (LRCS). His research has been focused on the synthesis and characterization of new materials for Li-ion and next generation batteries.

commercialisation, LIBs have enabled a revolution in portable electronic devices.[2] Now, they are being manufactured at large scale, bringing down their price and positioning them as the preferred energy storage solution for electric vehicles.[3] However, many challenges remain, the most important of which are shown in Fig. 1, in the campaign to further improve their performance and to develop the next-generation of LIBs.

Several different chemistries of LIBs exist, offering a variety of energy and power densities. One of the most common cathode (positive electrode) material families, $LiNi_{1-x-y}Co_xMn_yO_2$ (NMC), encompasses materials such as NMC111 ($x, y = 1/3$) and the more recent 'Ni-rich' NMC811.[4] These high Ni content materials, as well as others with a Li excess in the transition metal layer, are well-known to demonstrate a particularly high interfacial reactivity with the liquid electrolyte and with processing solvents during electrode fabrication. The particle surfaces must be coated or doped in order to stabilise the material.[5] In the development of new high-voltage cathode materials, novel high-performance and stable electrolytes must too be developed. Electrolyte stability is also important as new anode (negative electrode) materials emerge, such as silicon composites or Li metal. These materials operate at very low electrode potentials and must form stable interfaces with the electrolyte.[6]

The introduction of more solidified electrolytes such as solid polymer electrolytes (SPEs), gel polymer electrolytes (GPEs), as well as oxide or sulphide glass/ceramic-type electrolytes, is aimed at accessing high-voltage regimes and to provide a greater degree of safety.[7] However, compared with liquid electrolytes, they often suffer from poorer wetting at the electrode interfaces leading to poorer Li-ion conductivities and inferior performance.[8] Chemical incompatibility with the electrodes can also generate interfacial resistances.

There is little doubt that LIBs will play a large role for years to come, especially in applications that require very high energy or power densities. However, for those applications where low volume or mass is not so important, there are cheaper and/or more sustainable alternatives in the pipeline.[9–11]

Sodium-ion batteries (SIBs) use analogous electrode materials and electrolytes to LIBs.[12] Despite the higher reduction potential of Na^+/Na relative to Li^+/Li, potentially leading to lower energy densities for SIBs, the high abundance of sodium could allow for cost-effective and sustainable stationary energy storage, for example in the electricity grid. Many challenges remain, however, including the need for a suitable anode material and electrolytes which form stable interfaces against the electrodes.

Potassium-ion batteries (KIBs) offer similar advantages as for SIBs, but with a K^+/K reduction potential very close to that of Li^+/Li and the possibility to use graphite as an anode. However,

Dr Haidong Liu is a researcher at the Department of Chemistry – Ångström and the Ångström Advanced Battery Centre at Uppsala University, Sweden. He was awarded his PhD in Physical Chemistry by the University of Muenster in 2016 and performed postdoctoral studies at the University of Muenster and Uppsala University. Haidong's main interest focuses on design and synthesis of electrode materials and battery interfacial chemistry for long-life and high-energy density lithium-ion batteries as well as the next-generation technologies.

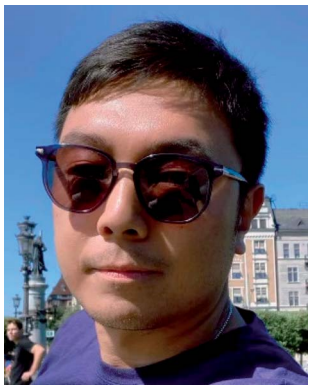

Ming-Tao Lee did his PhD works at Paul Scheer Institute (PSI). His expertise includes aerosol, battery, catalysis interfaces, and in developing and using synchrotron-based ambient-pressure X-ray photoelectron spectroscopy (AP-XPS) systems. He has carried out installation, commissioning and testing of the Bar XPS instrument (POLARIS), which is used in studies of industrially relevant catalytic reactions at pressures of several bars and at elevated temperatures at the synchrotron DESY. He has collaborated with several interdisciplinary groups/projects among chemists and physicists, academia and industry partners. He has also been responsible for synchrotron-based liquid micro-jet XPS experiments to study interfacial aqueous and non-aqueous chemistry at MAX IV.

Dr Andrew J. Naylor is a researcher at the Department of Chemistry – Ångström and the Ångström Advanced Battery Centre at Uppsala University. In 2022, Andy was appointed as Docent ('Associate Professor') with specialisation in materials chemistry. Following PhD studies in Chemistry at the University of Southampton, he held postdoctoral positions at the University of St Andrews and University of Oxford. Andy now leads a group whose research focus is to study battery interfaces, principally for next-generation technologies. Particular emphasis is put on the use and development of surface analysis characterisation techniques, especially for the investigation of new materials and electrolytes.

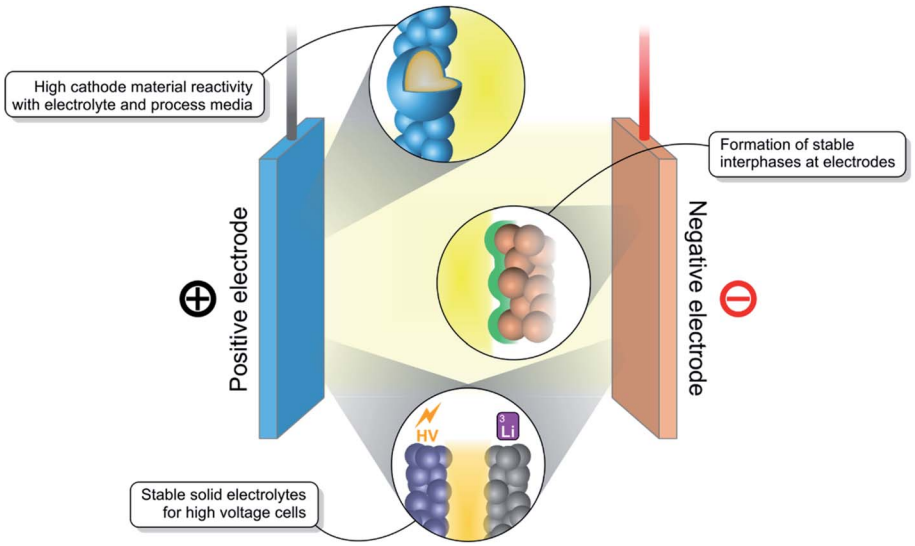

Fig. 1 Schematic diagram demonstrating the interfacial challenges generally found in rechargeable batteries. These mostly include cathode reactivity with electrolyte and process media, formation of stable interphases, and creation of stable interfaces between solid electrolytes and high-voltage electrodes.

such batteries are in very early stages of research and also experience interfacial instabilities.[13] Multivalent batteries (*e.g.* Mg^{2+}, Ca^{2+}, Al^{3+}) are yet another promising future technology, with the ability to double or triple the charge stored per metal ion,[14,15] Other interesting areas of research include lithium–sulphur (Li–S) batteries, which suffer from dissolution of polysulfide species into the electrolyte,[16] and metal–air batteries (*e.g.* Li–O_2, Na–O_2), in which oxygen gas from the atmosphere is reduced at a porous cathode.[17]

The interfacial stability and the interactivity between components are critical for high-performance batteries. However, due to their inherent inaccessibility and geometry, it is considered particularly difficult to characterise reaction interfaces within batteries. Nonetheless, this is essential when trying to understand the mechanisms underpinning such reactions and to designing protected electrode materials or more stable electrolytes, for instance.

1.2 Characterisation of battery interfaces

Numerous interfaces (*the point or area at which two phases meet*) exist in a typical Li-ion battery, between components including the electrodes, electrolyte, current collectors, binder particles, and separator.[18] The two main interfaces considered to be critical to a well-performing battery are the anode-electrolyte and cathode–electrolyte interfaces. Outside the electrochemical stability window of the electrolyte, at both low and high voltages, the formation of solid interphases (*a phase created at the interface of two existing phases, possibly displaying the properties of either or both*) can occur on the electrodes. These are the so-called solid electrolyte interphase (SEI) for the anode and most-commonly the cathode electrolyte interphase (CEI) for the cathode.[19] Aside from lithiation/delithiation of the electroactive phase, other phenomena that can occur at the anode include Li dendrite growth, particle cracking and reactions of the binder. For the cathode, transition metal redox reactions, dissolution and densification, oxygen redox, phase transitions, and current collector corrosion are of significant interest. Any of these interfacial reactions can affect performance of a battery, giving good reason to study them in detail by various characterisation methods.

When discussing battery interfaces, it is the surface regions of components making up the battery that are often referred to. Therefore, surface-sensitive and chemistry-sensitive techniques are commonly employed to probe changes at these surfaces, with respect to the pristine surface, after or during electrochemical testing of the battery.[18,20–25]

Imaging techniques such as scanning electron microscopy (SEM) and transmission electron microscopy (TEM) provide information on the morphology, particle size, and porosity.[26,27] Energy-dispersive X-ray spectroscopy (EDS) or electron energy loss spectroscopy (EELS) are frequently-used complimentary techniques for chemical analysis during the microscopy experiment. *In situ* or *operando* TEM experiments can capture interface transformation during heating, cooling or application of an electrical bias, probing the chemical composition and structure of particle surfaces in contact with an electrolyte. These techniques allow for a comprehensive understanding of structure, chemistry and geometry, but are not generally considered as surface-sensitive and provide only elemental compositional analysis. X-ray photoemission electron microscopy (XPEEM) may be considered an alternative imaging technique with greater surface-sensitivity.[28]

A technique growing in popularity for battery component analysis is time of flight – secondary ion mass spectrometry (ToF-SIMS), which combines the sputtering of a sample surface by a focused primary ion beam and detection of the emitted ions by mass spectrometry.[29,30] Despite being a destructive and

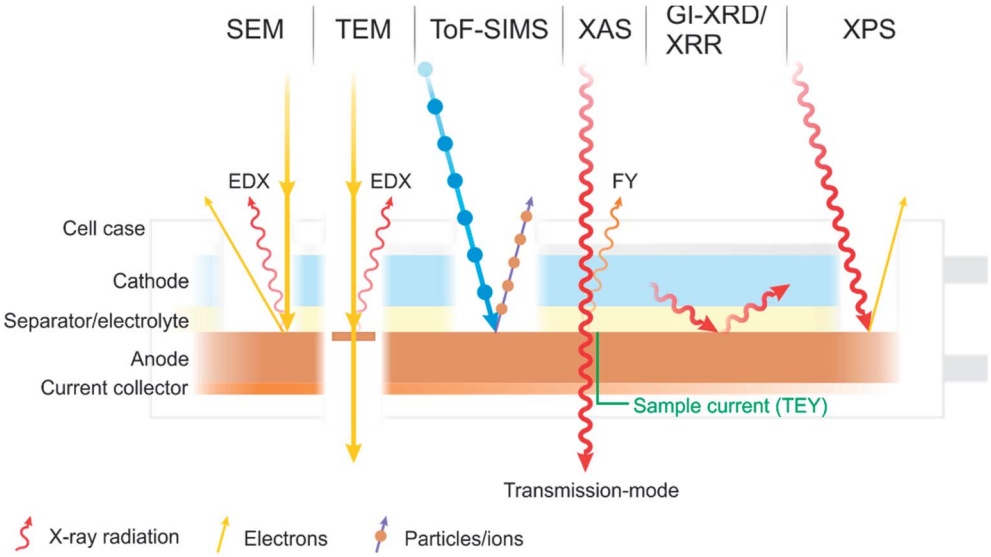

Fig. 2 A diagram summarising some of the most common characterisation techniques used to study the interfaces and interphases in batteries.

mainly qualitative technique, ToF-SIMS offers very high surface- and detection-sensitivity including isotope determination.

X-ray absorption spectroscopy (XAS) techniques, or more specifically X-ray absorption near-edge structure (XANES) and extended X-ray absorption fine structure (EXAFS), in transmission mode are bulk techniques that can determine oxidation states of elements in an electrode or whole system.[31,32] However, XAS in total electron yield (TEY) or fluorescence yield (FY) modes offer the possibility to obtain information only from the surface regions, typically up to 10's of nanometres depth for TEY or 1 μm for FY.

Other techniques relevant to studying battery interfaces include grazing incidence X-ray diffraction (GI-XRD),[33,34] X-ray reflectivity (XRR),[35] and various types of scanning probe microscopy (SPM) such as atomic force microscopy (AFM).[23]

There is one technique, however, which has become a characterisation technique at the forefront of battery research and is now commonplace in the characterisation of battery interfaces. That is X-ray photoelectron spectroscopy (XPS), sometimes referred to as photoelectron spectroscopy (PES), or historically and occasionally still as electron spectroscopy for chemical analysis (ESCA). Some of the various techniques described are summarised in Fig. 2.

1.3 X-ray photoelectron spectroscopy

XPS is a highly surface- and chemically-sensitive characterisation technique, traditionally performed, but more recently not always, under ultra-high vacuum (UHV).[36] A sample is irradiated with X-ray radiation of a fixed energy ($h\nu$), which if the energy is sufficient, causes excitation and ejection of electrons to the vacuum level. The kinetic energy (E_K) of the electrons is determined by an electron analyser, which can then be used to determine the binding energy (E_B, BE) according to eqn (1), where ϕ is the spectrometer work function. The binding energies of electrons are element specific and are further shifted according to oxidation state and bonding environment of the probed element.

$$h\nu = E_B + E_K + \phi \quad (1)$$

The surface-sensitivity of XPS stems from the fact that electrons are easily scattered by the sample itself after excitation.[37] Therefore, only those ejected from close to the surface of the sample will make it out of the sample and to the analyser. The escape depth is defined by the inelastic mean free path (IMFP) of electrons, where the probability of escape decreases exponentially with greater depth. The IMFP is highly proportional to the electron kinetic energy but is also dependent on the material density, molecular weight, band gap energy and number of valence electrons.[38] As a result, the use of X-ray sources of different energies allows for a non-destructive probing of varying analysis depths. This can be an attractive alternative to sputter-etching for depth profiling, which is addressed later. Higher energy sources may also give the possibility to access high energy core level transitions. By far the most common X-ray source on laboratory instruments is an aluminium anode (Al Kα, 1486.7 eV), which is often combined with a monochromator to achieve good energy resolution (~0.5 eV). Other sources are sometimes used including Mg (Kα, 1253.6 eV), Ag (Lα, 2984.3 eV), Cr (Kα, 5414.7 eV), and even Ga liquid jet (Kα, 9251.7 eV), each offering different flux and line width.[39,40]

Alternatively, synchrotron radiation sources can offer the possibility to tune the energy of the incident beam, allowing for hard X-ray- (HAXPES) or soft X-ray photoelectron spectroscopy (SOXPES) experiments to be performed.[41,42] This gives the experimentalist the option to choose energies corresponding to a variety of probing depths, allowing for a depth profile to be performed. Much higher beam flux can often be achieved with synchrotron sources. However, it is often acknowledged that battery electrodes, especially after cycling, are highly sensitive to radiation.[43] Therefore, care must be taken to attenuate or

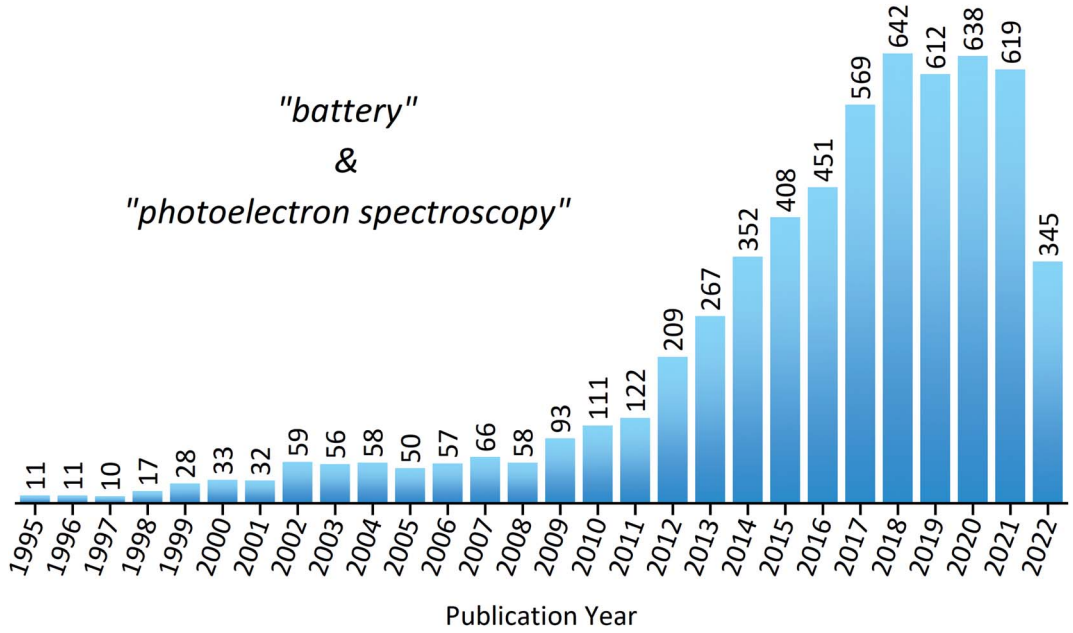

Fig. 3 The number of publications mentioning both phrases 'battery' and 'photoelectron spectroscopy' between 1995 and 2022, as determined through a search in Web of Science. Search phrase on 1 August 2022: TS = (battery and photoelectron spectroscopy).

defocus the beam, or to not irradiate the same analysis spot for too long. As is typical with synchrotron measurements, access is competitive, experimental time is limited, extensive sample preparation occurs before the beamtime, and the process of analysing the data can be a long one.

To put into perspective how important XPS is within the field of battery research, a statistical analysis of the literature reveals the substantial increase in publications over the last decade (Fig. 3). However, despite XPS being a powerful technique in materials characterisation, with the ability to determine surface layer thickness and perform quantitative composition analysis, there are many potential pitfalls to be made during measurements or analysis.[44,45] This is particularly true in the case of battery materials, which often exhibit complicated chemistry and structure. These practical issues, as well as tips and tricks to achieve success, will be discussed throughout the article.

Previous articles have provided detailed reviews of the use of XPS in studying LIBs and vanadium redox flow batteries.[46,47] Here, however, we provide an holistic overview of the use of XPS in studying an extensive variety of modern rechargeable batteries. Our aim is to collect examples of relevant and impactful work in this field to enhance understanding of interfacial chemistry in batteries and how XPS can be used to understand battery interfaces. Such understanding may in addition be applicable to other devices or fields of research.

In the next section, we focus on how XPS is used to characterise the surface regions of electrodes from rechargeable batteries, typically investigating the surface layers built up through decomposition of the electrolyte at the interfaces. However, practical considerations for measurements and data analysis are also discussed, since they are particularly important not only for battery materials but for XPS experiments in general. Following on, we address some of the bulk processes occurring for the battery components and how XPS can, for example, help further the understanding of charge compensation or degradation mechanisms. Then we review some of the latest studies using advanced XPS techniques, employing *operando* or *in situ* methodologies to uncover the phenomena in real-time during electrochemical analysis of rechargeable batteries. This section covers both solid-state cells and the development of ambient-pressure systems to study solid–liquid interfaces relevant to batteries. Finally, the state of the field will be summarised and our perspectives on the direction for the use of XPS in studying rechargeable batteries will be offered.

2 The electrode–electrolyte interface

2.1 An introduction to interphases and practical considerations when characterising them

The electrolyte used in commercial LIBs is typically composed of the salt $LiPF_6$ dissolved in a mixture of organic carbonate solvents such as ethylene carbonate (EC) and ethyl methyl carbonate (EMC). In addition, a large number of additives exist and are used to enhance the interfacial stability, cell safety, and/or performance of the electrolyte to transport Li-ions between the two electrodes.[48] The exact electrolyte recipes are of course closely-guarded corporate secrets; however, some typical additives, particularly those used in a research laboratory, are known to be fluoroethylene carbonate (FEC), and vinylene carbonate (VC).

The organic electrolyte used in modern rechargeable batteries (or, for that matter, any type of electrolyte) has an electrochemical window within which it is considered stable. Below potentials of approximately 0.8 V *vs.* Li^+/Li, organic solvents, such as ethylene carbonate or diethyl carbonate, are known to be thermodynamically unstable towards reduction.

This results in their decomposition and formation of the passivating SEI layer, as a new phase on the anode surface.[49] The SEI ideally passivates the electrode surface, prohibiting electron transfer, to avoid continuous electrolyte decomposition and consumption. In the ideal case, this results in a kinetically stable system, in which Li^+ ions can still diffuse rapidly between electrode and electrolyte. The SEI is generally composed of inorganic and organic, polar and non-polar species, with a high dependency on the electrolyte composition and with thicknesses typically in the range of tens of nanometres. The structure of the SEI, though, has been a topic of much debate over the past three decades, with a double-layered structure and 'mosaic' models often referred to.[50–53] The CEI is often determined as being even thinner than the typical SEI thickness, making it even more difficult to characterise. In general, it forms through the high-voltage oxidation of the electrolyte at the cathode electrode surface, but some cathode material surfaces are particularly reactive (*e.g.* Ni-rich, Li-rich materials) and can react in ambient air or in contact with the electrolyte.[19,54,55] The nano-length-scales of the interphases formed at battery electrodes, and their intricate chemical structure are the main reasons why their properties and relations to performance remain so elusive, but also why XPS is commonly the chosen technique to characterise them.

In this section, we discuss in broad terms the challenges of characterising such surface layers as the SEI and CEI. Issues of sample preparation, storage, fundamental experimental methodologies and data treatment are considered. In the following parts, we will review specific examples of these phenomena that occur in various types of rechargeable batteries.

2.1.1 Sample preparation

2.1.1.1 Exposure to reactive environments. One of the most important things to realise is that lithium and the other alkali metals, often present in elemental form in lab-scale batteries or as compounds in the electrode, electrolyte or SEI/CEI, are highly reactive, even with O_2, N_2, CO_2 and moisture in the air. Schroder *et al.* performed a study to investigate the effects of exposing silicon electrodes after electrochemical processes to the ambient atmosphere, before using XPS to analyse the surface.[56] Fig. 4 demonstrates how the composition of the SEI layer can change quite remarkably over a short period of exposure to the ambient atmosphere. The authors propose LiF dissolution in moisture, and the generation of carbonates and oxides (lithium) as the major mechanisms, through various reactions with oxygen and carbon dioxide in the air.

Other studies have shown similar phenomena, in particular for the SEI on lithiated graphite electrodes, or the reactivity of the solid electrolyte $Li_7La_3Zr_2O_{12}$ (LLZO) with moisture and its effect on interfacial resistance.[57,58] Studies of Li metal in various organic carbonate-based electrolytes have also revealed the reactivity of alkyl carbonates ($ROCO_2Li$), very often considered a major component of the SEI, with water to form Li_2CO_3, CO_2, and ROH.[59]

Therefore, to prevent chemical reactions of the samples, especially those extracted from cells after electrochemical testing for *ex situ* characterisation, it is necessary to transport air-sensitive samples under a protective atmosphere to the load lock of the XPS instrument. This is often achieved using a gas-tight sample transporter containing argon (or other inert gas) or that is under vacuum, to transfer samples from a glovebox where the batteries were disassembled. Where there is no dedicated solution for transfer of air-sensitive samples to an instrument, often a glovebag can be attached to the load-lock entry port of the instrument, flushed several times with argon, and used to load samples into the instrument. However, this rarely provides the same level of reassurance that the samples are unaffected as would a dedicated solution. Fig. 5 shows an array of various devices employed for the transfer of samples between an inert environment (*e.g.* a glovebox) and an XPS instrument.

While we do not wish to point out specific instances, there are studies in the literature which do not use such devices to prevent air-exposure of sensitive battery samples. Such studies often rely on transferring samples quickly from a glovebox with minimal air-exposure over the course of 10's of seconds. However, in reality it is likely that there is quite significant

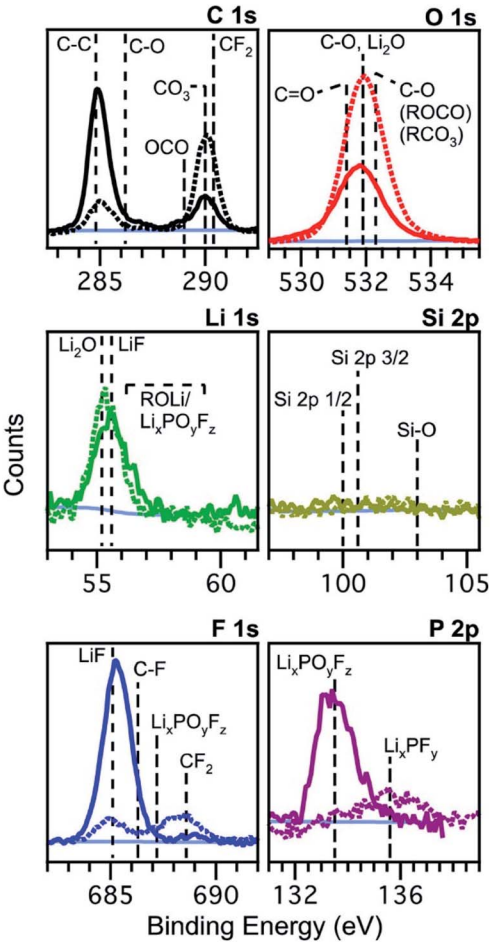

Fig. 4 XPS spectra of silicon (001) wafer electrodes after preparation by chronoamperometry at 0.01 V *vs.* Li^+/Li for 300 s in an electrolyte of 1 M $LiPF_6$ in ethylene carbonate (EC) and diethyl carbonate (DEC), 1 : 1 w/w. Solid lines: measured without exposure; dashed lines: measured after exposure to the atmosphere for 10 minutes. Reprinted with permission from ref. 56. Copyright 2012 American Chemical Society.

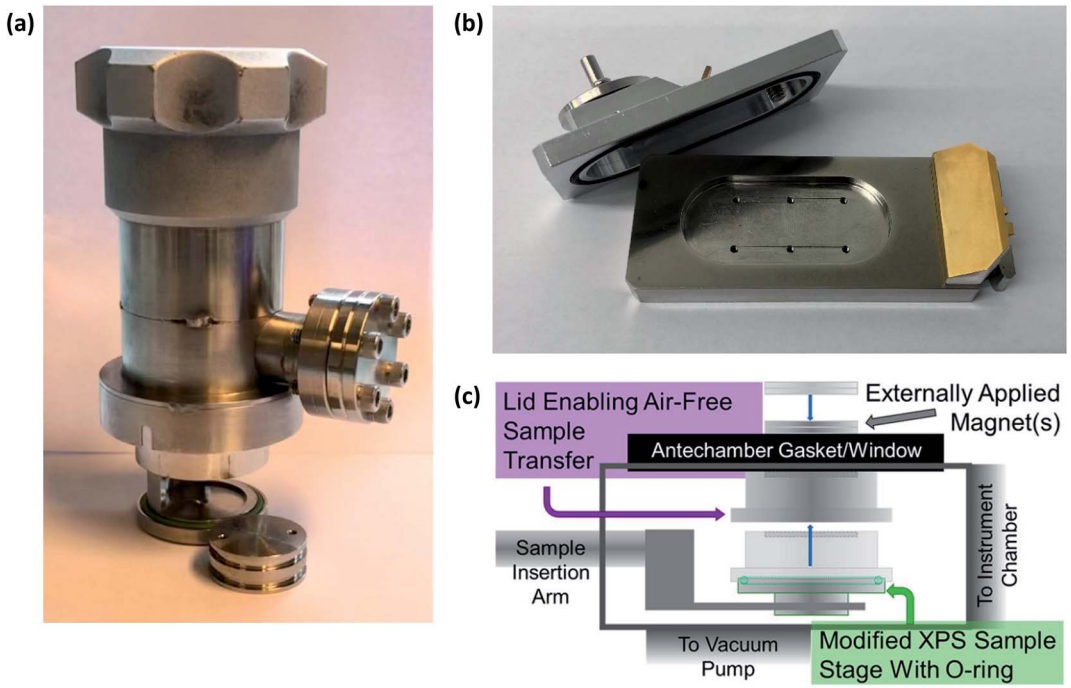

Fig. 5 Devices for air-sensitive transfer of samples to XPS instruments. (a) Sample transfer cup for PHI 5500 XPS instrument. (b) Air-sensitive sample shuttle for Kratos AXIS Supra+. (c) A magnetic sealing sample holder: Reprinted with permission from ref. 60. Copyright 2020 American Chemical Society.

exposure, especially due to instrument load-lock chambers often taking several minutes to pump down to acceptable pressures. Now with such high competition in the research field, through the production of high-quality science, it is absolutely necessary to always handle air-sensitive battery samples under an inert atmosphere.

Equally important is the way in which samples are stored or shipped before measurements take place. In our experience, the less time there is between removing electrodes from cells and making the measurements, the better. This will give fewer opportunities for reaction of the sample with any potential impurities in the glovebox atmosphere, including oxygen, moisture, and other contaminants. Furthermore, the materials used to package samples for shipping can also contaminate them. For example, many plastics or adhesive tapes contain silicones, which can easily migrate to the sample surface.[61] However, sometimes it is necessary to prepare samples days in advance of a synchrotron beamtime or to ship samples to a collaborator's lab for analysis, in which case it is difficult to avoid the necessity to disassemble batteries beforehand and package the samples. One particularly important study, though, demonstrated that the best method to preserve the SEI chemistry is to transport the unopened cells and perform the measurements as soon as possible after opening them.[62] It should be noted, however, that this study was performed on lithium-ion batteries where the SEI may remain stable in contact with the electrolyte for several days or weeks. It has been demonstrated that other chemistries, such as SIBs, can suffer from SEI dissolution over relatively short timescales, in which case it may be preferable to remove electrodes from cells as soon as possible after electrochemical testing.[63–65] Overall, the general advice is often to avoid plastics and adhesive tapes as much as possible, transport unopened cells if the interfaces are known to be stable; otherwise, use clean glass or metal containers, each containing individual samples to avoid cross-contamination. The same advice is valid for samples stored in the home laboratory for future measurement; storage under ultra-high vacuum or in an inert environment (*i.e.* a glovebox) is recommended, while trying to avoid contamination from nearby substances.

2.1.1.2 To wash or not to wash? That is really the question. The question of how to store and transport samples without contaminating or exposing them is one that can be addressed relatively easily with the correct understanding and equipment. However, the 'age-old' question of whether to wash a battery electrode sample, or not, before performing XPS measurements is somewhat trickier to answer. Through the authors' experiences, and based on a limited literature on the topic,[49,57,66–69] several advantages can be suggested to washing a sample, which has the effect of removing the excess electrolyte on the surface of the electrode:

(1) There will be little electrolyte salt residue after drying the electrode that could block the signal from the 'region of interest' (*e.g.* the SEI or CEI), beneath.

(2) There will be less chance of observing 'charging' in the XPS spectra during measurement, due to the presence of electronically insulating salt residues (potentially avoid using charge neutralisation).

(3) The salt residues can be highly-prone to beam damage during XPS measurements, therefore limiting the possibility to obtain a suitable spectrum.

(4) The surface will be chemically homogeneous (assuming little contribution to inhomogeneity from electrochemical processes or cell assembly); salt residues could crystallise only in particular areas of the sample.

(5) If using a highly volatile solvent for washing, the sample will dry more quickly, and will avoid the need for elevated temperatures to drive off low vapour pressure electrolyte solvents.

(6) Salt residues from the bottom of the sample will be removed, which otherwise could have prevented electrical conductivity to the spectrometer if performing grounded measurements.

There are also many disadvantages:

(1) The SEI, CEI or other interfacial region of interest may be partially/fully dissolved and removed by the washing solvent.

(2) Washing may lead to some chemical reaction with the solvent, altering the interfacial chemistry.

(3) There may be impurities in the washing solvent which could react with the interfacial species.

(4) A potentially useful 'internal reference' (*i.e.* an electrolyte component, for which one knows the expected binding energy for calibration) may be removed through washing.

Of course, a lot depends on the method used for washing, including its severity, the washing solvent and its purity, the duration, as well as how the residual solvent is removed before measurements (*i.e.* drying in ambient glovebox conditions, under vacuum, or elevated temperature).[57] Somerville *et al.* investigated the effects of washing graphite electrode after cycling against $LiCoO_2$ with varying amounts of vinylene carbonate (VC) in the electrolyte.[66] As can be observed in Fig. 6, the washed electrode exhibited only one fluorine environment, corresponding to the decomposed $LiPF_6$ salt, Li_xPF_y, while the spectra for unwashed electrodes showed peaks for LiF and the intact salt. The authors concluded that washing with DMC would result in the removal, not only of the electrolyte salt, but also of LiF and Li_xPF_y species from the SEI layers.

Washing of the electrodes is sometimes said to be the 'better of two evils', since you might not gain any information when a thick salt residue forms on an unwashed sample. However, it depends on the system one is investigating and the measurement instrumentation available. It is advisable to make measurements of samples which are washed and some which are unwashed, compare the results and determine what works best in a particular case.

2.1.2 Depth profiling. Depth profiling XPS experiments are particularly important in the study of battery interphases, due to their often-complex layered structure. There are three typical methods that can be used to create depth profiles of samples by X-ray photoelectron spectroscopy: tuning the photon energy of the incident X-ray beam, changing the take-off angle to the detector by tilting the sample, and, using ion sputter etching. Only the latter one is a destructive technique, while the former two are non-destructive.

2.1.2.1 Energy-tuned XPS: SOXPES and HAXPES. Through varying the photon energy of the incident X-ray beam, the kinetic energy of the photoelectrons is therefore varied for a given core level at a particular binding energy, according to eqn (1) and as described in Section 1.3. A higher kinetic energy results in a greater IMFP for a given sample material, and therefore leads to a deeper probing depth. Modern laboratory instruments often offer the option of multiple fixed energy sources, as described previously. Using synchrotron facilities, one can often tune the photon energy to almost any value within the operating range. However, this is dependent on the beamline setup and may result in lower flux or a greater line width at particular energies. Synchrotron-based XPS depth profiling is often referred to by two different terms: SOXPES which usually described measurements with photon energies below about 1500 eV, and, HAXPES which describes anything above 2000 eV.[46,70–73] These are neither strict definitions, nor are they defined definitively anywhere; some also refer to the range between them (~1000–3000 eV) as the tender X-ray regime. The advantages of tuning the photon energy to perform depth profiling on battery interfaces are:

(1) It is a non-destructive technique.

(2) One can often choose the desired energy based on the intended probing depth, calculated using, for example, the TPP-2M equation.[38]

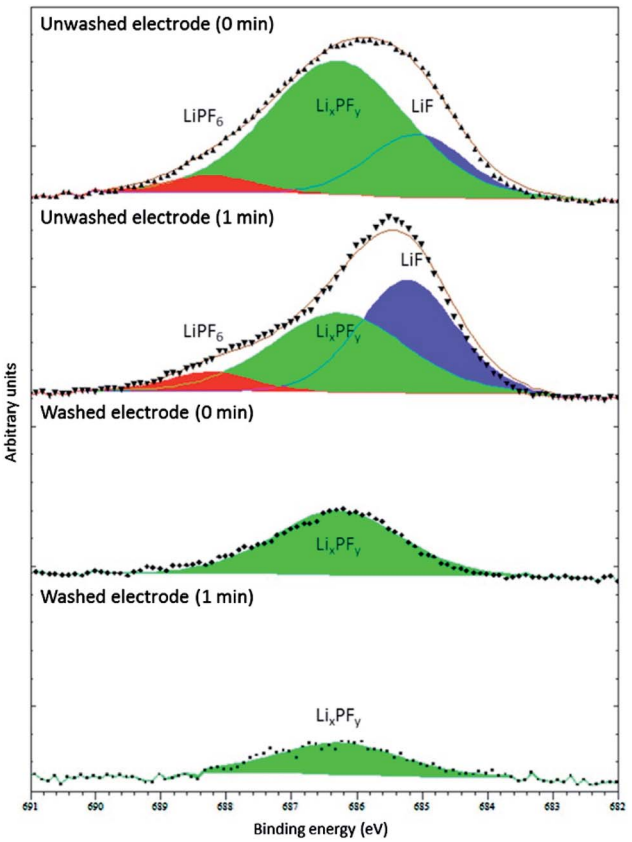

Fig. 6 F 1s XPS spectra (Al Kα, 1487 eV) from washed (dimethyl carbonate (DMC), 2 min, dried in argon) and unwashed graphite anode from full cells with $LiCoO_2$ cathode and electrolyte of 1 M $LiPF_6$ in ethylene carbonate (EC)/ethyl methyl carbonate (EMC), 3 : 7 w/w. The minutes in the figure refer to the duration of Ar^+ sputtering before XPS measurement. Reproduced under CC-BY licence from ref. 66.

(3) Auger peaks, which have fixed kinetic energies, can be strategically shifted on the binding energy scale to avoid overlapping with photoelectron peaks.

(4) Higher cross-section values are achieved using higher photon energies for some core levels, thereby improving the signal from those elements when compared to using Al Kα radiation.

One disadvantage of using this technique, however, is that spectra contain information from the whole probed depth, including the surface, while the contribution drops off exponentially with greater depth. This can result in misinterpretation of data. A technique that does not experience this issue is ion sputter etching.

2.1.2.2 Ion sputter etching. A well-known method for depth profiling of samples by XPS is to employ monatomic argon ion (Ar^+) sputter etching, in which spectra are recorded between regular sample etching periods. In contrast to tuning the photon energy to achieve depth profiling, sputter etching is a destructive technique that removes the top layers of a sample by rostering over a specified area. While this technique works well for metallic samples and some inorganic samples, it is considered chemically damaging for organic materials. Ion-implantation can occur within the surface of the sample and the high ionisation potential can lead to the surface chemistry being substantially altered, leading to unreliable results. For example, it has been demonstrated to cause reduction of transition metals, which could pose a problem for many battery electrodes which contain transition metals.[74,75] In general, monatomic argon ion sputter etching is not an appropriate technique for battery electrode samples due to their inhomogeneous nature. Electrodes are almost always composites of an inorganic active material, conductive carbon additive and polymeric binder, and often comprise sensitive SEI/CEI layers. The etching rate depends to a high degree on the hardness of the material; therefore, hard materials (metals/inorganics) will have lower etching rates than for soft materials (organics). Not all materials of the composite will be etched at the same rate, thus leading to preferential sputtering of some materials and resulting in an unreliable depth profile.[76,77]

To circumvent some limitations posed by monatomic ion etching, one can use a more 'gentle' sputtering technique such as argon cluster ion (Ar_n^+) or C_{60} sputtering.[78–80] Gas cluster ion sputtering (GCIS), as the technique is commonly known, can be quite often found as an option on modern XPS instruments. While there are so far few examples for the use of GCIS in battery research, it offers promise due to its ability to sputter etch soft materials without leaving much chemical damage.[81,82] This is a result of using large clusters of argon atoms (up to several thousand atoms) with large incident energies (up to tens of thousands eV), giving a low average energy per atom. The low energy prevents significant chemical damage, but the large clusters allow for the removal of material from the sample at appreciable rates (though often not so high rate as for monatomic sputter etching).

GCIS is a technique that is particularly interesting for battery samples, especially when attempting to map the structure of the sensitive SEI layer. There is much work still to be done in this area and we can expect to see an increase in the systematic use of GCIS to study battery materials.

2.1.2.3 Angle-resolved XPS. Finally, the non-destructive technique, angle-resolved XPS (ARXPS) can be considered as another alternative for depth profiling of samples.[83,84] A higher take-off angle (*e.g.* 90°), more of the bulk sample is probed with photoelectrons detected from greater depths. At lower take-off angles (*e.g.* 30°), photoelectrons from shallower depths are detected resulting in a more surface-sensitive measurement. Particularly for thin-film layered samples, this technique can be useful for determining layer thickness and composition. However, for samples with high roughness and porosity such as battery electrodes, this technique may not give very reliable results.

2.1.3 Measurement and analysis considerations

2.1.3.1 Charging. A well-known and common phenomenon for users of XPS is so-called 'charging' of a sample surface. Charging can cause large shifts to higher binding energies, broadening and distortion of peaks.[85] This can occur when a source of electrons is not available to replenish those ejected through the photoemission process. This is often the case, for example, when the material under investigation has poor electronic conductivity, is an insulator, or is not properly grounded *via* the sample holder and stage. There are several methods to largely prevent charging including the use of conductive adhesive tapes, conductive silver paint, mixing the sample with a conductive additive (*e.g.* carbon black), sputtering a thin conductive layer on the surface, employing a charge neutraliser, or reducing the X-ray power.

Battery electrodes, which are most often composite materials as described previously, can experience differential charging. This is where the different components with varying conductivities cause parts of the sample to have different electron electrochemical potentials. It is therefore recommended to electronically isolate the sample from the instrument ground and use a well-functioning and optimised charge neutraliser to maintain a constant surface potential. This is often called a 'floating' configuration. Unfortunately, it is not always possible for instruments where there is not a suitable charge neutralisation system, such as at some synchrotron beamlines. Then, the next best solution is to ground the sample to the instrument and attempt to prevent extensive charging through effective sample preparation.

2.1.3.2 Radiation damage. Battery electrodes, particularly those that have sensitive surface layers after electrochemical cycling, can be susceptible to radiation damage during XPS measurements.[43] This can occur due to a high dosing of the sample when the X-ray beam has a high flux or a particular area of the sample is analysed for long period of time. This can result in chemical damage, typically observed for organic or polymeric compounds and can be characterised by comparing spectra of the same core level (*e.g.* F 1s or C 1s) at the beginning and end of a measurement run. Possible remedies may include reducing the X-ray power, defocusing or attenuating the beam, or measuring for shorter durations on multiple spots (the available options may depend on which instrument is being used).

2.1.3.3 Data analysis. The assignment of peaks to particular atomic environments in XPS data is an incredibly important process for accurate interpretation of the results. The development of an appropriate model with a good quality fit to experimental data requires an exact understanding of the sample, the possible surface reactions that could have occurred and a full overview of binding energy reference values from reference samples, related experiments or from literature. However, binding energy values available in the literature can vary extensively for any element in a specific chemical environment, due to the multiple experimental setups and data analysis methodologies employed. This makes analysis of XPS data challenging for any sample, not only for battery samples. However, for battery samples, the formation of surface layers with unknown chemistry, structure, and their potentially high reactivity adds an extra dimension to the difficulty. In spite of this, XPS is becoming one of the most commonly used techniques for battery electrode characterisation, and there is a large literature with which to compare experimental data.[68]

There are many potential pitfalls when it comes to background fitting, peak fitting and assignment, as well as presentation of the data and model in a publication.[86] One of the most important steps in the data analysis procedure is energy calibration. As was eluded to previously, this can be achieved in multiple ways. If the sample is conductive, a fermi energy calibration should be performed, for example by measuring a known metallic peak. Alternatively, a species with known binding energy is chosen as an internal reference. Often for XPS data, the adventitious carbon (C–C, sp^3-hybridised) peak at 284.8 eV is used for energy calibration since it is present very often on the surface of samples that have been in air.

However, for battery samples that may not have been exposed to the air and which may have formed a surface layer containing similar such carbon environments, it may not be useful as a reliable reference. A species that is present in most electrodes and that does not tend to undergo reaction is the conductive carbon additive. This is often referred to as carbon black, but can be any of a number of different products available. The sp^2-hybridised carbon environment in these materials usually is observed at approximately 284 eV but can vary depending on the product. Therefore, a reference measurement of the carbon black should be made to help with interpretation and calibration of the sample of interest. Peaks for other species present in the sample can also be used for energy calibration, such as a metal which is known to have a stable oxidation state, or lithium for which there exists absolute binding energies for various compounds.[87]

Energy calibration for spectra from battery samples often comes with complications. Aside from charging, shifts in binding energy can occur for several reasons. These include the electrode state of charge, electrode electrochemical potential and the presence of an SEI or other surface layer, and can affect peak positions by several eV.[88] This is often considered to be the result of an interfacial dipole layer between 'surface' and 'bulk' components, which causes binding energy shifts between species in the sample.[89] Such phenomena can significantly affect the interpretation of results, particularly when binding energy shifts due to lithiated or oxidised phases are also common in battery samples. It is suggested to perform energy calibration to either a surface species or a bulk species, or compare the two different calibrations.

Transition metal spectra are particularly difficult to interpret, especially for battery materials where the metals (*e.g.* Ni, Mn, Co, Fe, Ti, V, Nb) may be in unusual chemical environments. The determination of oxidation states for these metals is not trivial, particularly when there may be mixtures of states near the surface region of samples. It can be that the peak shape is more indicative of the oxidation state than the binding energy, which can seem counter-intuitive when attempting to analyse the spectra. This is demonstrated in one study that measured spectra for a Ni, Co, and Mn-containing oxide thin film (Fig. 7).[90] There are, however, a series of useful literature sources to aid in such analysis.[90–92]

2.2 Surface phenomena in lithium-ion batteries

2.2.1 The anode solid electrolyte interphase. The formation of the SEI on various anode materials, in particular graphite and lithium metal, has been well-reported and reviewed previously.[46] It has typically been determined, by XPS experiments, to exhibit a layered structure. Inorganic species (*e.g.* LiF, Li_2O, LiOH, Li_2CO_3) reside close to the electrode material surfaces, with organic species (*e.g.* alkyl carbonates, polymers) closer to the electrolyte. However, the species are still arranged in a mosaic fashion rather than a well-ordered discrete layered manner. This has been the prevailing theory for many years and is reaffirmed by many XPS studies of LIB anodes.[6,23,51,52,93] Therefore, the following sections focus more on the cathode interfaces, which are not so well understood.

2.2.2 The cathode surface. One of the key issues hindering the adoption of Ni-rich NMC/NCA ($LiNi_{1-x-y}Co_xAl_yO_2$) materials is their high air/moisture sensitivity and rapid reaction in such media. These reactions can lead to the formation of Li_2CO_3/LiOH surface impurities and a spontaneous reduction of Ni^{3+} to Ni^{2+} in the surface region of particle.[94–98] The surface chemistry of cathode materials is especially important when considering production, processing, compatibility with other cell components, such as the electrolyte, as well as device performance. The formation of adventitious Li_2CO_3 on the surface of NCA particles during exposure to air was investigated by in-house XPS and hard X-ray photoelectron spectroscopy (HAXPES, $h\nu \approx 5940$ eV) measurements.[98,99] Measurement of the O 1s, C 1s and Ni 3p/Li 1s core levels confirmed the presence of surface Li_2CO_3 and was supported by infrared spectroscopy. O 1s core-level spectra of NCA stored under ambient conditions for a variety of durations showed a peak at 531.5 eV, which was attributed to the presence of Li_2CO_3 on the surface, alongside the peak at 529 eV for the metal oxide. The Li_2CO_3 thickness was approximated as 2 and 4 nm for NCA stored under inert and ambient conditions, respectively, calculated using the surface oxygen signal assuming a continuous surface layer.

XPS analysis was used to probe the surface changes of various NMC materials when exposed to water. Wood *et al.*

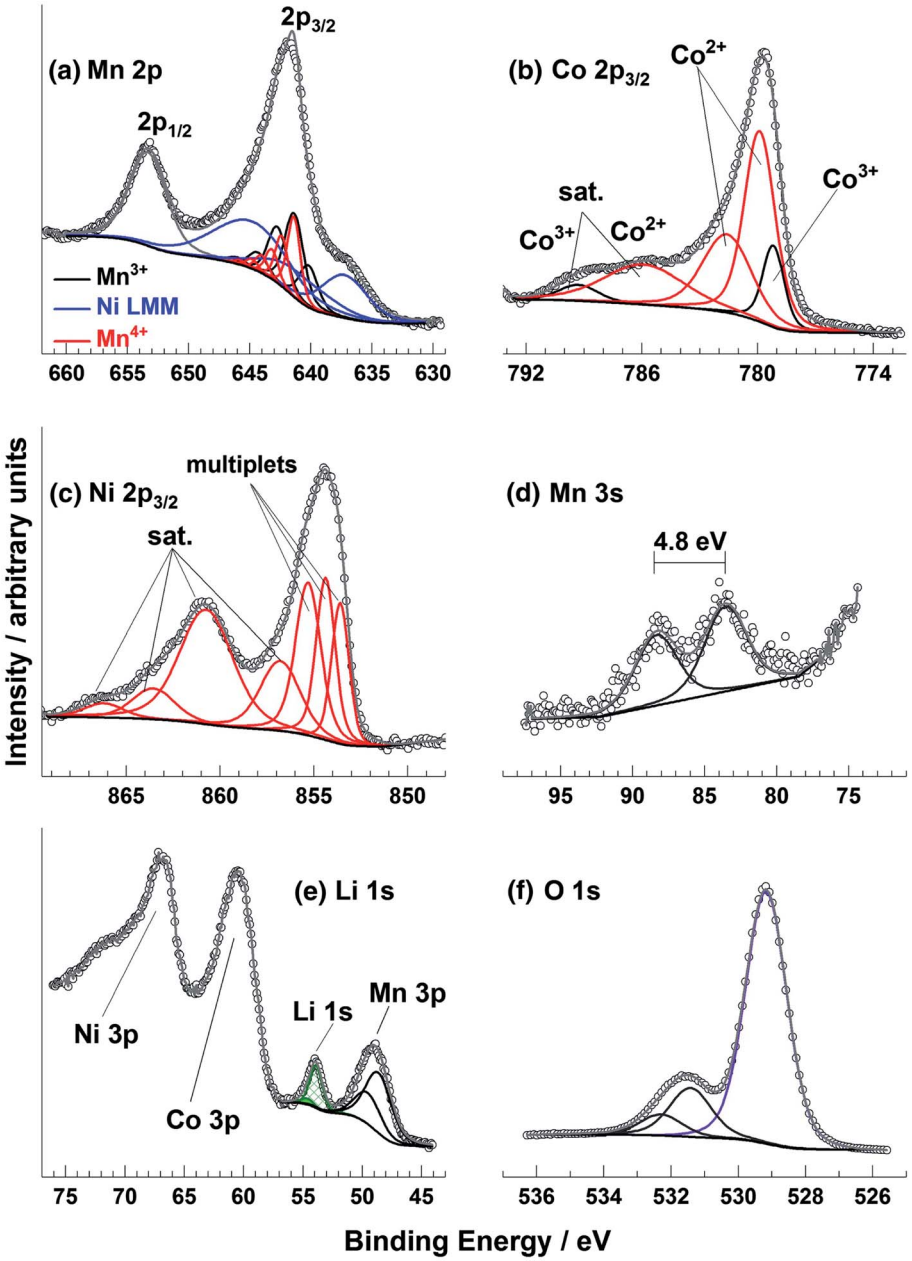

Fig. 7 Mn 2p, Co 2p, Ni 2p, Mn 3s, Li 1s, and O 1s XPS spectra for a radio frequency magnetron sputter deposited Li–Ni–Mn–Co–O thin film sample. Reprinted with permission from ref. 90 Copyright 2017 John Wiley & Sons, Ltd.

evaluated the water compatibility of four different NMC powders with increasing Ni content during water-based processing, which is aimed at reducing cost and environmental impact.[100] Only a minor change was observed in carbon and oxygen spectra for the Li_2CO_3 layer on the surface of NMC after aqueous processing. The layer remains quite thin, characterised by the continued presence of the transition metal oxide peak.

2.2.3 The cathode electrolyte interphase. Similar to the anode, the reactions occurring at the interface between the cathode and electrolyte can directly determine the overall performance of the battery. The cycle life and reliability of the battery is not only strongly dependent on the SEI properties as discussed above, but also determined by the so-called cathode-electrolyte interphase (CEI). Again, here we use the term *interphase* to indicate the growth of a new phase on the electrode surface, similar to for the SEI. At least when discussing state-of-the-art LIBs, their degradation and failure mechanisms are closely related with the cathode itself and the processes it undergoes during operation. However, the detailed mechanisms of CEI formation and evolution are not yet fully understood, even for well-established LIB technologies.[101] A deep understanding of the crucial roles played by the cathode material and the electrolyte in interactions at the interface during cycling, is of paramount importance to enhance the electrochemical performance and reliability of batteries.

With a similar nanometre thickness range to the SEI on the anode, XPS is a powerful tool in analysing the electronic structure, chemical composition, and geometry of the CEI and/or the cathode surface. While energy-tuned XPS often allows for characterisation of the entire surface, interphase, and some part of the bulk, in this section we will focus on the surface and interphase phenomena, but exploring the bulk in a later section. XPS can contribute in a unique way to understanding the chemical/electrochemical reactions during charge/discharge processes, and can be effective in helping to understand the formation and evolution of the CEI layer but also the complex reactions occurring from the cathode itself.

2.2.3.1 Structure, composition and formation mechanisms. The CEI forms as a result of electrochemical reactions at the cathode surface where it is in contact with the electrolyte. These reactions can include the precipitation of solids at the surface. The dominating factors that affect the CEI formation can be mainly ascribed to the initial surface specific adsorption behaviour and solvated coordination behaviour as illustrated in Fig. 8.[102,103] The specific adsorption on the electrode determines the initial structure and chemical composition of the interface, while the solvated coordination structures of the electrolyte serve as a method for repair of the interphase during cycling.

Demonstrating some parallels to the SEI formation, carbonate-based electrolytes undergo oxidation reactions to form the CEI at the cathode surface during charge.[104] The composition of the CEI is a highly debated subject and is very much dependent on numerous factors. As a result, the proposed composition of the CEI varies from one publication to the next, as operating conditions and other parameters such as electrolyte composition, can be very different.[105,106] Thus, it is not possible to give a general composition or structure of the CEI. However, there are some ideal properties that it is thought the CEI should exhibit, including low thickness, high density, low ionic resistivity and electron conductivity, as well as good electrochemical and mechanical stability. Fig. 9 presents a schematic diagram for the composition and structure of the CEI thought to form on an NMC cathode in LIBs. As is shown, a large number of different inorganic compounds and a complex mosaic structure are formed at the NMC material surface.

It is understood that the surface chemistry of the cathode material can play a significant role in the CEI formation and its composition. Huang *et al.* suggested that the stability of the CEI on NMC811 could be influenced by the synthesis method employed (rapid co-precipitation and spray-drying routes to produce spherical NMC811).[108] The chemical composition of the formed CEI on the NMC811 from different synthesis methods before and after cycling were determined by XPS. In comparison to the pristine materials, the cycled electrodes had a greater surface content of oxygen, fluorine, and phosphorus, while a decrease in carbon was observed. From peak fitting of the data, the increase in the above elements mainly originates from the formation of electrolyte decomposition products, such as LiF, LiP_xO_y, Li_2CO_3, and various organic compounds, that make up the CEI. Comparing the cycled NMC materials synthesised by the different routes, the surface layer of rapid co-precipitation-NMC has much larger amounts of the CEI products, which is ascribed to the more severe interfacial reactions. These reactions consume a large amount of active transferable

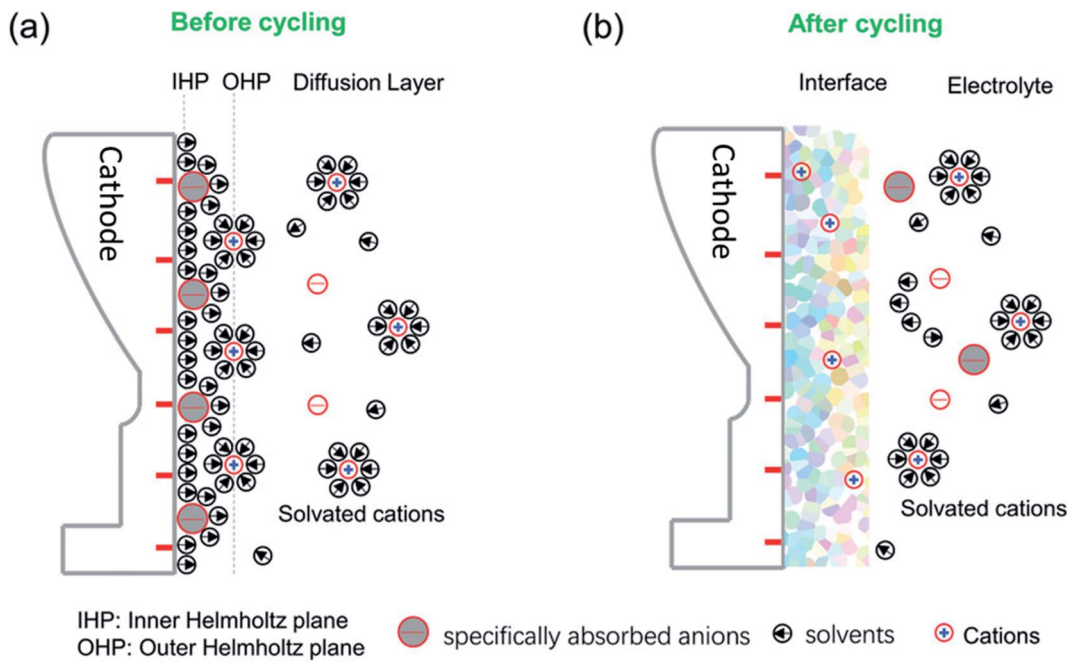

Fig. 8 A schematic diagram of the cathode–electrolyte interface before and after cycling and the formed CEI after cycling. (a) The ions and solvents will be specifically absorbed on the inner Helmholtz plane (IHP) before cycling. (b) The specific species of the IHP and the solvated groups become oxidized or otherwise decomposed during cycling, along with the disappearance of the IHP. Reproduced under CC-BY licence from ref. 103.

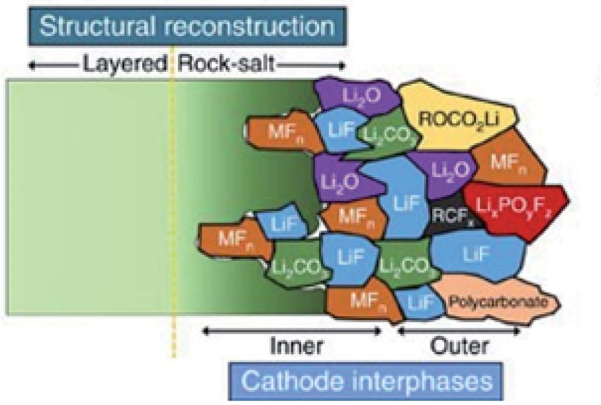

Fig. 9 A schematic diagram of the microstructure and chemical composition of the CEI at the interface between a typical NMC cathode and carbonate-based electrolyte. Reproduced under CC-BY licence from ref. 107.

lithium, leading to an increase in the interfacial resistance and a loss in capacity.

The CEI is a very dynamic entity, changing in chemistry and structure during long-term cycling of the battery. XPS analysis of cycled $LiNi_{0.7}Co_{0.15}Mn_{0.15}O_2$ electrodes, presented in Fig. 10, reveals the CEI composition after calendar ageing and after 100 cycles.[107] While the pristine material shows that a native film of Li_2CO_3 exists on the particle surfaces, upon ageing in the electrolyte and cycling, various electrolyte degradation products are formed. Such products are thought to include semicarbonates, LiF, MF_x, $Li_xPO_yF_z$ and RCF_x. There is a noticeable increase in the thickness of the CEI for the aged electrode when compared with the cycled electrodes, characterised by the relative intensities of peaks for CEI species against the peaks for bulk components (*i.e.* O^{2-} and C–C). Furthermore, an effect of the secondary particle size was reported; the CEI appears to have a greater thickness for the larger particle size. The authors also find that the conductive carbon additive in the electrode can have a significant effect on the CEI evolution. The CEI formed initially on the carbon additive can be exchanged readily with the cathode particle surface, suggesting closely intertwined interactions between the cathode material and the carbon. Therefore, it is not necessarily accurate to study CEI formation in model systems in the absence of carbon additives or binders.

The use of electrolyte additives is an important strategy to improve the electrochemical performance of batteries. Such compounds added to the electrolyte, typically in concentrations of <10%, are often designed to improve interfacial chemistry.[109–113]

The role of tris(trimethylsilyl) phosphite (TMSPi) as an electrolyte additive to improve the electrochemical performance of NMC811/Si–graphite cells was investigated by synchrotron-based XPS depth profiling.[114] The morphological and compositional differences of the CEI and SEI were probed for the cathode and anode, respectively. As shown in Fig. 11, the formed CEI with TMSPi on the NMC811 cathodes displayed an increased amount of alkyl carbonates/carboxylates, with a decreased amount of PF_xO_y species. Moreover, this TMSPi-derived CEI on the cathode can effectively suppress the polyvinylidene fluoride (PVDF) binder degradation and the cathode to anode "cross-talk" of the migration of the decomposed CF_x species.

In another study, it was found using synchrotron XPS that the Li-rich disordered rocksalt oxyfluoride material Li_2VO_2F reacted very strongly with the organic electrolyte, resulting in

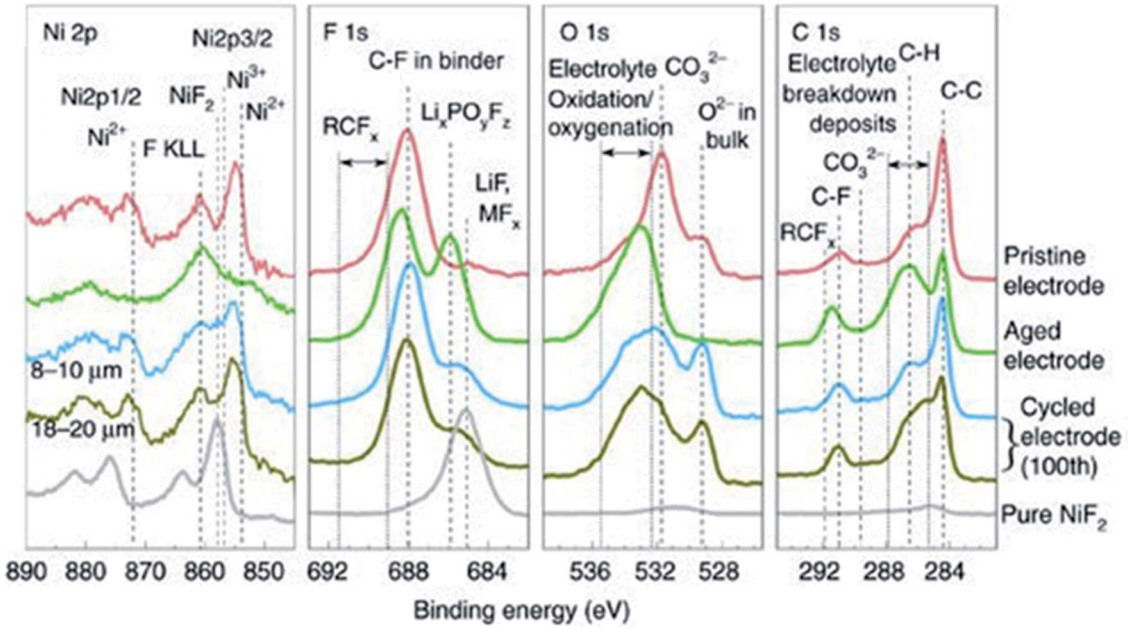

Fig. 10 XPS spectra (Ni 2p, F 1s, O 1s, C 1s) of $LiNi_{0.7}Mn_{0.15}Co_{0.15}O_2$ electrodes (pristine, aged, and cycled electrodes with 8–10 and 18–20 μm particle sizes) and pure NiF_2. Reproduced under CC-BY licence from ref. 107.

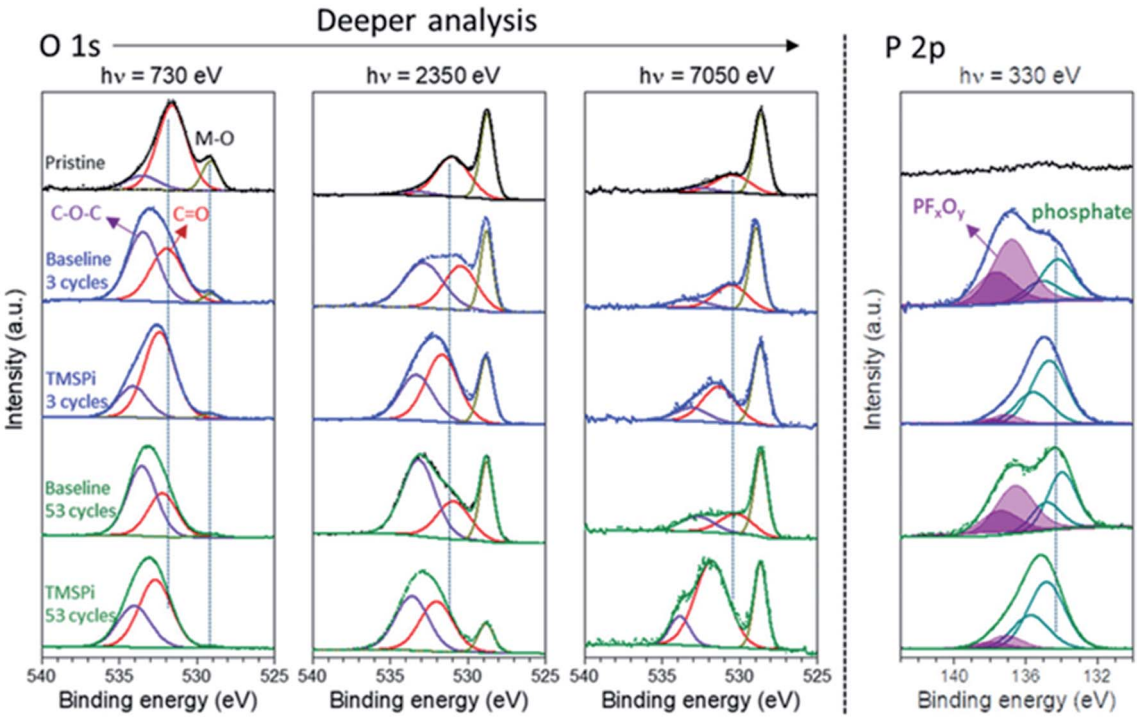

Fig. 11 O 1s and P 2p XPS spectra (at three photon energies) of the pristine and cycled NMC811 electrodes taken from discharged cells after up to 53 cycles with and without 2 wt% TMSPi as an electrolyte additive. Reproduced under CC-BY licence from ref. 114.

a rapid degradation of the material and its capacity to store charge.[115] To mitigate this detrimental issue, electrolyte additives including lithium bis(oxalato)borate (LiBOB), lithium difluoro(oxalato)borate (LiODFB), and glycolide were employed.[116] Through further XPS studies it was found that the improved capacity retention was due to the formation of a protective CEI at the cathode surface, preventing excessive degradation of the oxyfluoride material. Other strategies including doping of the oxyfluoride material with either titanium or iron, or employing AlF_3 particle coatings, also proved effective in boosting capacity retention through stabilisation of the cathode surfaces.[117,118]

2.2.3.2 Cross-talk. Electrolyte additives are also useful in preventing transition metal dissolution from cathode materials. The transition metal ions in cathodes act as the redox centres through which the storage of Li^+ ions is charge compensated. One of the biggest challenges for many cathode materials, especially those next-generation high-capacity materials containing elements such as manganese, iron or vanadium, is transition metal dissolution. The loss of these redox centres from the material itself inherently leads to a capacity fading.[119–121] This process not only alters the surface structure of the cathode material particles, but equally as important, can affect the structure and composition of both the CEI and the SEI on the anode. This occurs through a process known as 'cross-talk', where species migrate from one side of the cell to the other, for example transition metals from the cathode dissolving in the electrolyte then depositing on the anode. XPS can again be used as an effective technique to detect the transition metals deposited at either electrode surface, even in small concentrations, and perform a quantitative analysis.

Ochida *et al.* demonstrated, using XPS measurements of graphite anodes, the deposition of metallic manganese and subsequent oxidation to MnO under open-circuit conditions.[123] This work suggested that the deposition of Mn metal on the graphite could be largely affected by the selected additives. At the same time, the slight differences of the deposited Mn or Mn-based compounds on the graphite electrode could be identified by XPS. Similar with no additive, the cyclic ether additive, 1,4,7,10,13,16-hexaoxacyclooctadecane (18C6), could not suppress the deposition of Mn since a peak at around 639 eV (640 eV for without additive) could be identified as Mn metal. On the other hand, 1.4 wt% 4,7,13,16,21,24-hexaoxa-1,10-diazabicyclo hexacosane (C222) additive were found to effectively suppress the Mn deposition due to no peak in the Mn 2p spectrum as observed by XPS shown in Fig. 12. In addition, some other transition metal dissolution phenomena on the cycled electrodes were confirmed by the XPS spectra, such as V (V 2p) and Fe (Fe 2p).[122,124] For example, the V 2p spectra in Fig. 10b indicated that the dissolved vanadium from the $Li_{2-x}VO_2F$ cathode was deposited on the anode surface during cycling. The deconvolution of vanadium gives the V $2p_{3/2}$ peak at 516.1 eV and the V $2p_{1/2}$ peak at 523.5 eV, respectively, and indicates the deposited vanadium has a +4 oxidation state.

In summary, sustained efforts have achieved a fundamental understanding in terms of the components, structure, and the formation mechanisms of the CEI layers, as well as how they influence the overall properties of the cells. It has been found

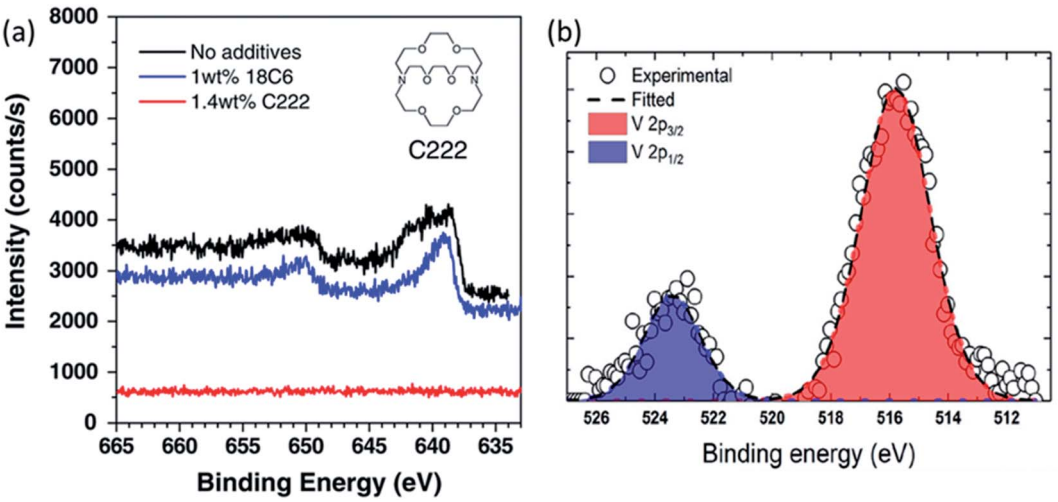

Fig. 12 (a) Mn 2p spectra of graphite electrodes after 5 cycles with $LiMn_2O_4$ cathodes in 1 M $LiClO_4$/EC + DEC with and without the 18C6 or C222 cyclic ether additives. Reproduced from ref. 119 with permission from the Royal Society of Chemistry. (b) V 2p core level of the vanadium deposited on the anode. Reprinted with permission from ref. 122. Copyright 2019 American Chemical Society.

that electrolyte additives, surface coatings, particle size and the chemistry of the cathode material itself can have a large influence on the CEI properties and hence on the overall performance of a cell.

2.2.4 Interfacial reactions with gel and polymer electrolytes. While many XPS studies of battery interfaces involve the use of liquid electrolytes, as has typically been present in commercial lithium-ion batteries, an interesting area of research now moves towards gel or polymer electrolytes. Such electrolytes can offer safety benefits and increased stability, allowing the use of high voltage cathodes or lithium metal anodes for greater energy density.[125,126] Just as for liquid electrolytes, electrochemical side-reactions occur between electrode and gel/polymer electrolyte during operation, often forming an interphase. This can be probed by XPS; however, sample preparation can be even more challenging for such investigations, especially when there is strong adhesion between the electrode and electrolyte.

Xu *et al.* studied the interfaces within SPE-based graphite half cells using XPS.[127] Samples were prepared by dissolving the polyethylene oxide (PEO)-based SPE from the cell in acetonitrile. It was found that the SPE contained up to 2300 ppm H_2O, depending on the preparation method, which resulted in extensive LiOH formation on the graphite electrode surface after one discharge (lithiation). For the same interface, evidence of LiTFSI (lithium bis(trifluoromethanesulfonyl)imide) decomposition was also presented. At the Li-SPE interface, mostly LiF and lithium alkoxides were formed. The SEI products in the SPE cell were vastly different to the carbonate or PEO-type polymers typically found at electrode interfaces after cycling with a liquid electrolyte.

The use of gel/polymer electrolytes often show a greater degree of stability towards high-voltage cathode materials, compared with liquid electrolytes. The poly(vinylene carbonate-acrylonitrile)-based gel polymer electrolyte (PVN-GPE), which was synthesised through copolymerisation of vinylene carbonate and acrylonitrile, exhibited a large electrochemical stability window.[128] This "5 V class" polymer electrolyte was used to demonstrate excellent cycling performance of $LiNi_{0.5}Mn_{1.5}O_4$/Li metal cells. The authors used XPS to characterise the cathode electrolyte interface (CEI) on the LNMO after 200 cycles, finding generally less intense signals for the peaks attributed to electrolyte decomposition, when compared with a similar experiment using a liquid electrolyte. It is thought that the strong adhesion of the GPE to the electrode reduces the available active sites for electrolyte decomposition. Furthermore, the high oxidation stability of the GPE and its compatibility with the cathode suppresses the formation of the CEI.

The removal of liquid from the electrolyte conveniently allows the development of *in situ* and *operando* methodologies still under ultra-high vacuum and investigation of potential next-generation all-solid-state battery technologies. XPS is also an essential tool in the investigation of many other potential next-generation technologies, particularly those not based on lithium.

2.3 Interfacial reactions in 'beyond Li-ion' technologies

Similar principles are applied when employing XPS to study battery types other than LIBs. This is especially true for chemistries that similarly rely on kinetic stabilization by surface layer formation but as some selected examples will show the use of XPS goes beyond SEI studies.

A very closely related system is the KIB that often use graphite anodes.[129,130] SIBs constitute another active field of battery science; however, these are unable to use graphite without the co-intercalation of solvents.[131,132] XPS has been found to be a valuable tool in studying both SIBs and KIBs.[133–138] Going even further into novel systems, we find multivalent-ion batteries based on magnesium and calcium that present further unique challenges and require some unique solutions.[139,140]

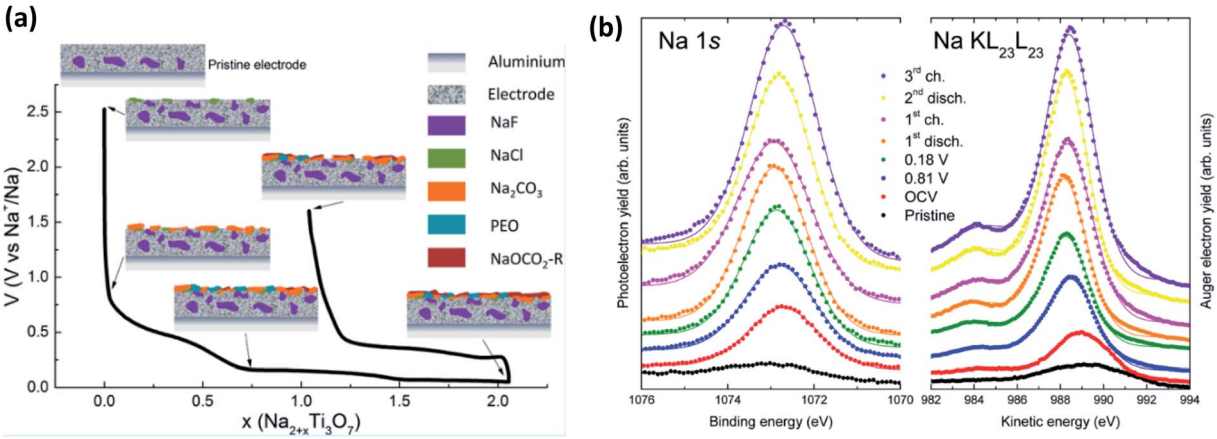

Fig. 13 (a) The composition and evolution of the SEI on $Na_2Ti_3O_7$ electrodes as determined by XPS. (b) Na 1s XPS spectra and Na $KL_{23}L_{23}$ Auger transition spectra for electrodes at different states of charge. Reprinted with permission from ref. 143. Copyright 2015 American Chemical Society.

2.3.1 Sodium-ion batteries. SIBs primarily use hard carbon as the anode, though alloy anodes are common as well. SIB anodes have the advantage of usually giving an intense Na 1s peak and a Na KLL Auger peak close to the binding energy of O 1s although this is often sufficiently shifted to binding energies which do not interfere with the O 1s peak. Unfortunately, most XPS work done on sodium anodes is still performed using carbonate electrolytes in half-cell configuration and thus the results are likely influenced by the highly reactive sodium electrode.[141,142] Further complicating the issue of XPS measurements on sodium anodes is the issue of SEI solubility; it has been shown by XPS measurements that the SEI composition is affected by leaving the electrode at open circuit voltage (OCV) in EC:DEC electrolytes.[63]

This being said, a notable example of the use of XPS for SIB studies is from Muñoz-Márquez *et al.*,[143] that investigated the SEI formation on $Na_2Ti_3O_7$ anodes (Fig. 13a). In their work they describe several important points to SIB-XPS measurements: (1) they reaffirm that the SEI in SIB consists mostly of inorganic compounds, (2) they show that there are organic compounds formed that are being dissolved during the charging of the anode, and (3) they show that PVDF binder reacts with sodium to form NaF. The energy calibration for XPS studies of SIBs can often be done using the graphitic carbon peak at ~284 eV that is commonly present due to the carbon active material or conductive carbon additives. However, in SIB systems this peak is not always visible as the SEI grows beyond the probing depth of most in-house XPS instruments. This issue, combined with the surface charging effects that results, are somewhat mitigated by analysis of the Auger parameter (α) for Na, by determining the energy shift between the Na 1s photoelectron line and the Na $KL_{23}L_{23}$ Auger signal (Fig. 13b).

Ether and carbonate electrolytes result in significantly different SEI composition and function, which is well described in investigations where glymes and carbonates are used in conjunction with TiO_2 and hard carbon anodes.[144,145] They use XPS measurements combined with ion-sputtering to reveal that ethers have a significantly higher proportion of inorganic compounds in the inner SEI layer than carbonates (Fig. 14). This is shown by the rapidly decreasing carbon signal with sputtering depth as compared to the carbonate electrolyte in the TiO_2 system while the hard carbon showed a continual rise in NaF content during sputtering. The large difference in SEI properties between ethers and carbonates are also evident in alloy systems. Wang *et al.*[146] utilized XPS to characterise bismuth anodes where the SEI from G2-glyme was found to contain polyethers and sodium alkoxides, whereas the carbonate instead formed polyesters and sodium alkylcarbonates.

Ethers enable the use of graphite as an anode for SIB through the co-intercalation of the solvent, albeit at the cost of capacity and energy. This co-intercalation of solvent is however quite interesting from an SEI analysis perspective since any SEI must allow solvent molecules to pass through in order for the system to function. The initial investigations of this system by Maibach *et al.*[147] makes use of synchrotron-based depth profiling. The authors describe a system where the NaFSI salt decomposes to form a thin (<8 nm) passivation layer below 0.5 V *vs.* Na^+/Na that allows the solvent and Na-ions to pass through. It cannot be ruled out that the ethers participate in the SEI formation in these systems although their reduction stability should allow them to endure the cycling environment.

2.3.2 Potassium-ion batteries. Most work performed for KIBs has been performed on graphite and hard carbon although just as with sodium, some interesting work is performed on alloy and polyanionic anodes. The SEI on graphite anodes has been investigated using both carbonates and ethers such as G2-glyme. XPS measurements confirm that in these two different solvent classes, the surface layer is quite different. This is not surprising for graphite since the ethers alter the electrochemistry significantly by co-intercalation into graphite providing a voltage profile akin to that of sodium systems, as shown in Fig. 15.

In the case of carbonate electrolytes and graphite, it has been reported that significant SEI formation occurs during the first

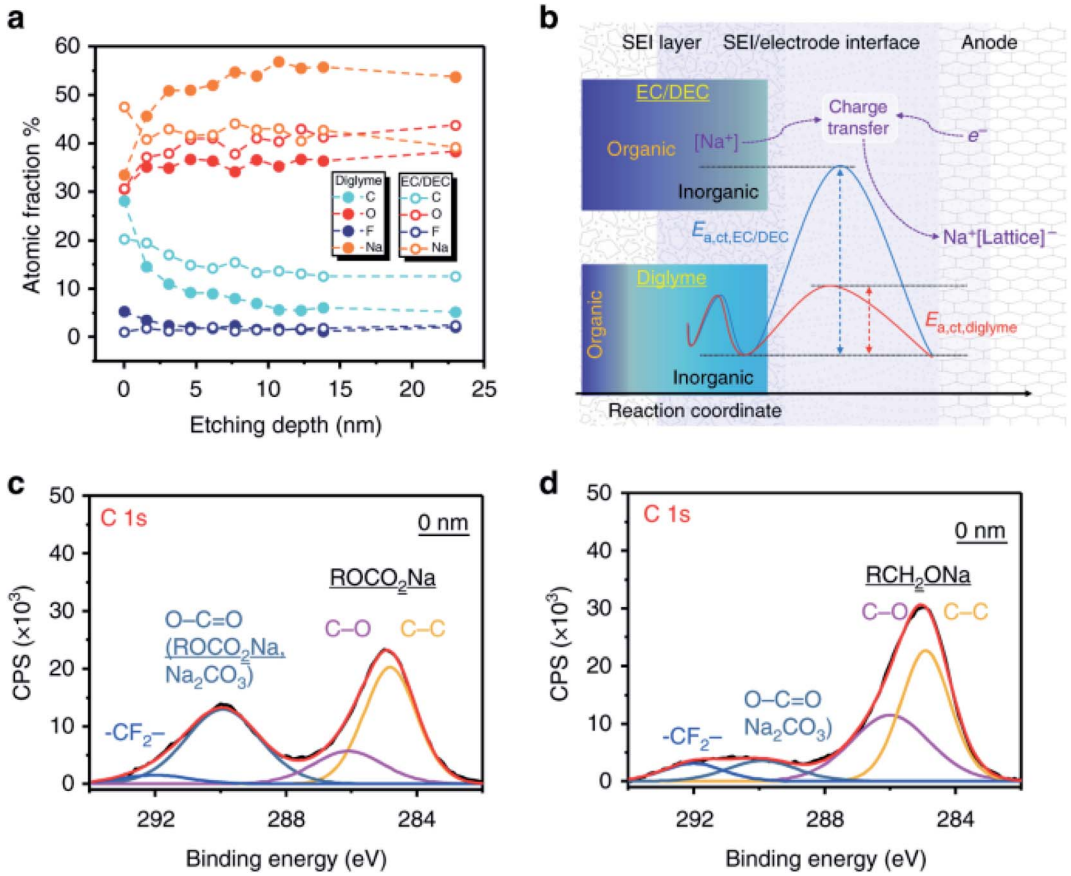

Fig. 14 (a) Quantitative analysis of XPS data from sputtering depth profiling of the SEI formed from ether and carbonate electrolytes. (b) Schematic diagrams for the SEI composition. (c) C 1s spectrum for the electrode with carbonate-SEI before sputter-etching. (d) C 1s spectrum for the electrode with ether-SEI before sputter-etching. Reproduced under CC-BY licence from ref. 144.

discharge and that it forms organic alkoxides, potassium alkyl carbonates and potassium carbonate with subsequent increases in fluorine contains species as cycling progresses.[148,149]

There is, however, some disagreement as to the composition and thickness of the SEI. Lei *et al.*[148] report that the SEI thickness is less than 4 nm after the first discharge based on high resolution TEM measurements, supported by XPS measurements where a signal at 285 eV is attributed to the K–C species. In contrast, Naylor *et al.*[149] use SOXPES and HAXPES to describe the SEI in a very similar system and found that it would reach up 50 nm in thickness based on the complete disappearance of the graphite/KC_x peaks (Fig. 16). The authors also report that the thickness depends on the state of charge with

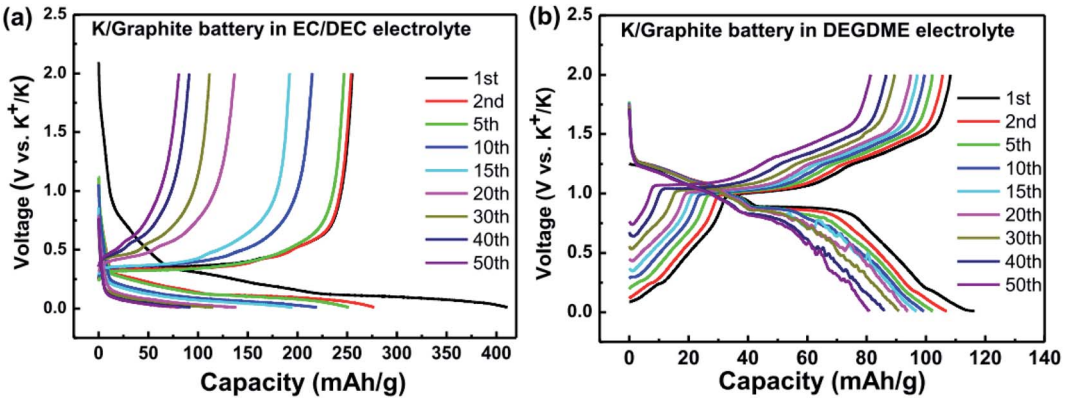

Fig. 15 Galvanostatic voltage profiles for K/graphite cells using (a) carbonate, and (b) ether electrolytes. Reprinted from,[148] with permission from Elsevier.

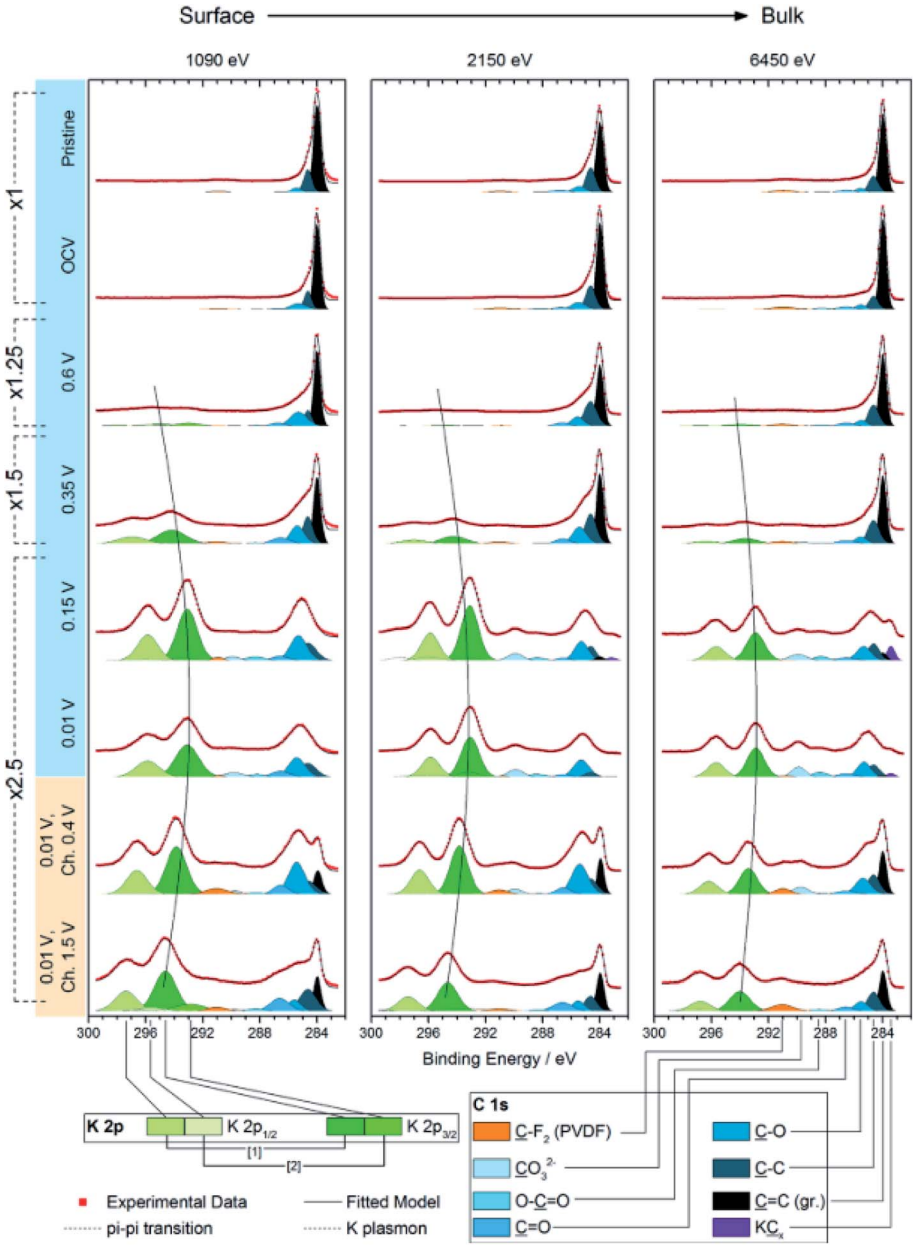

Fig. 16 K 2p – C 1s XPS spectra measured using SOXPES/HAXPES for graphite electrodes at various states of charge from carbonate-based electrolytes. Reprinted with permission from ref. 149. Copyright 2015 American Chemical Society.

a clear increase of the SEI thickness during discharge and subsequent thinning during charge.

As in the case of sodium metal, the potassium electrode is also reported to be problematic as it decomposes carbonate electrolytes. Lei *et al.*[148] shows that the SEI formed on the potassium metal in carbonates is continually growing with detrimental effects on the performance of the graphite electrode. In fact, a lot of the degradation seen in half-cells can be reversed simply by replacing the potassium counter electrode (CE). This shows just like in the case of sodium half-cells that investigators must be very careful to not let the influence of the metallic alkali counter electrode skew their results.

While potassium graphite systems are usually compared to LIB system, potassium hard carbon finds its most relevant comparison in sodium. Unfortunately, there has been very little work on using hard carbon anodes for potassium systems. XPS measurements by Chen *et al.*[150] indicate that the SEI goes through the same processes of thickness variation as described for the K-graphite system, as presented in Fig. 17. This can be inferred by the intensity shift of the substrate carbon peak, though the authors make no such claim.

2.3.3 Multivalent batteries. Multivalent battery chemistries are not new in concept but the research into Mg-ion and especially Ca-ion batteries has increased rapidly in the last few

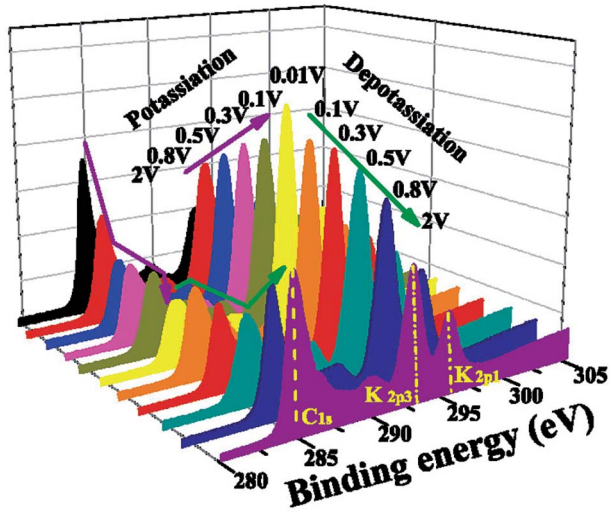

Fig. 17 K 2p – C 1s XPS spectra of hard carbon electrodes at various states of charge from potassium systems, showing the increase and subsequent decrease in the substrate signal. Reprinted from ref. 150, with permission from Elsevier.

years.[151] For a long time, progress was held back by issues such as non-permeable SEI formation on the metallic anodes, and lack of suitable electrolytes and cathode materials. Even though these issues are still major obstacles there has been progress made and XPS is an invaluable tool for characterising and developing these systems.[152–154]

In magnesium-ion batteries, the blocking nature of the SEI formed on Mg metal anodes can be overcome by several strategies. One compelling example is by Matsui *et al.*[155] that uses intermetallic compounds such as Mg_3Bi_2 to facilitate the deposition of Mg^{2+}. In this work XPS is used to show that the passivation layer consists of MgF_2 from the decomposition of the bis(trifluoromethylsulfonyl)amide ($TFSA^-$) anion (Fig. 18a). The authors detect little difference in the SEI layer between the electrochemically inactive Mg_3Sb_2, pure Mg anodes and the active Mg_3Bi_2 anode. However, the Mg 2p XPS spectra show that Mg exists as Mg^{2+} in Mg_3Bi_2 and this is claimed to lead to fast reaction kinetics and could thus explain the striking difference in electrochemical performance.

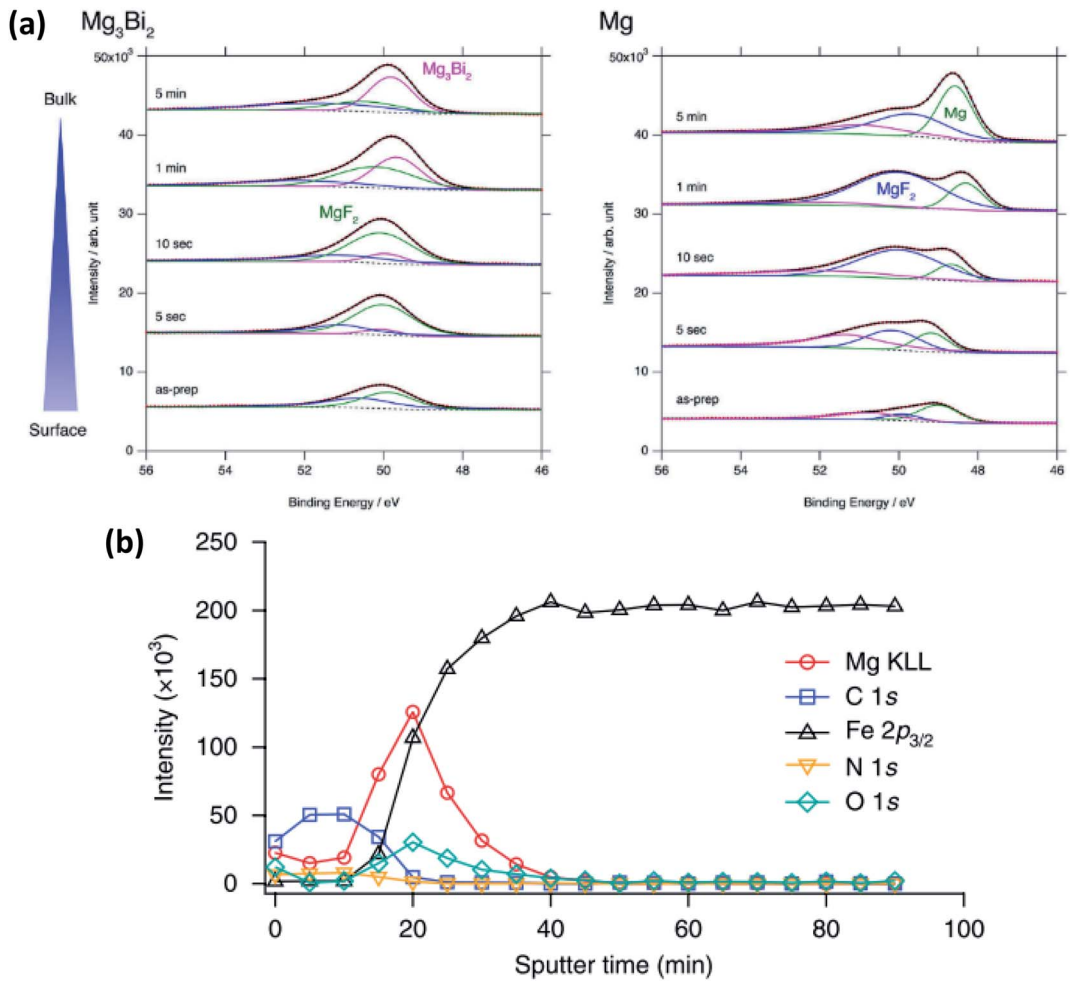

Fig. 18 (a) Mg 2p XPS spectra after sputter-etch depth profiling for Mg_3Bi_2 and Mg thin films immersed in 0.5 mol L^{-1} $Mg(TFSA)_2$ in BuMeG3 solution for 24 h. Reproduced under CC-BY licence from ref. 155. (b) XPS sputter-etch depth profiles of a Mg-coated stainless-steel electrode in 0.5 M $Mg(TFSI)_2$-PC electrolyte. Reprinted by permission from Nature Chemistry[156] Copyright 2018.

Another example, from Son *et al.*,[156] uses artificial passivation layers to avoid the blocking nature of the Mg metal in carbonate electrolytes by applying a thin layer of thermal-cyclized polyacrylonitrile (cPAN) and magnesium triflate. This layer allows for impressive stripping and plating performance in propylene carbonate (PC) and even allows for stable cycling with water present in the electrolyte. The use of XPS provides insights into the nature of the passivation layer and combined with sputter-etching confirms that the Mg is actually deposited below the artificial SEI (Fig. 18b).

Calcium has many of the same issues as magnesium and these challenges are exacerbated by the low reduction potential of Ca metal that is very close to that of lithium. Although it has been proven possible to plate and strip calcium in carbonates at moderate temperatures,[157] there is a need to improve the Ca diffusion through the SEI. This can be done in several ways. In the work of Wang *et al.*,[158] tin is used as an alloying anode for Ca in a strategy reminiscent of the intermetallic compounds used for Mg. The surface layer formed on the Sn anode consist of CaF_2 and $Ca(PF_6)_2$ originating from the salt used in the electrolyte. The fluorine compounds appear together with organic species such as $(RCOCO_2)^-$ formed by a ternary mixture of carbonates used as the solvent. As we have seen earlier, graphite can be used together with ethers to promote intercalation of ions by wrapping them in a solvation sheath. Prabakar *et al.*[159] used this strategy and found that G4-glyme would lead to reversible intercalation of Ca^{2+} in graphite. The authors used XPS to show that G1–G3 glymes did insert Ca ions but that they were trapped in the structure. Further measurements at different stages of charge of the graphite showed that, not only did the calcium signal intensify during the insertion, but the carbon signal from G4 was seen to appear as well (Fig. 19).

In summary, the chemistries proposed for technologies beyond LIBs come with many issues and a lot of these are surface related. XPS experiments can be useful in addressing many of these challenges. The most common use is of course for SEI analysis, but we have also seen examples where oxidation states of the bulk anodes as well as co-intercalated solvents in graphite have been detected and proved instrumental for the analysis.

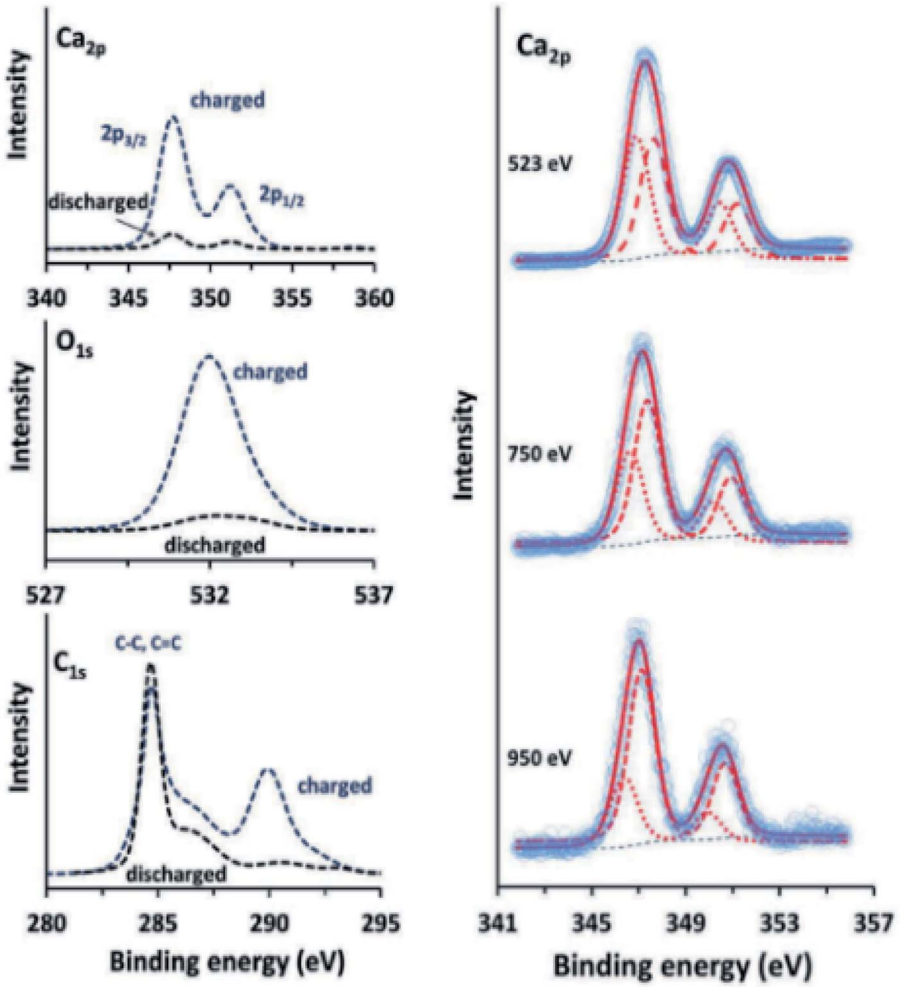

Fig. 19 Ca 2p, O 1s, and C 1s XPS spectra (left) of charged and discharged (−2.9 and −0.2 V *vs.* SHE, respectively) graphite electrodes in a calcium system using G4-glyme electrolyte. Ca 2p XPS spectra (right) of charged graphite electrodes, measured using synchrotron radiation at different photon energies, showing the presence of surface Ca^{2+}. Reproduced under CC-BY licence from ref. 159.

3 Bulk material phenomena characterised by XPS

Where the surface layers on an electrode material are thin enough or when using a high enough photon energy (HAXPES measurements), it is possible to probe the 'bulk' electronic structure of the material. Depending on the size of particles making up a composite electrode, this may still, though, be considered as very surface sensitive. For battery materials in particular, it is interesting to study the oxidation states of the transition metals, which are most often the redox centres involved in charge compensation when charging or discharging the battery.[160,161] However, in recent years oxygen redox activity has become an interesting topic to investigate, especially since such activity can lead to greater capacities.[162,163]

3.1 Transition metal redox activity

The redox activity of V in Li_2VO_2F cathodes was reported to be analysed by XPS as displayed in Fig. 20.[115] The binding energy difference between the MO peak (~530 eV) and the V $2p_{3/2}$ peak can be used as a measure of the vanadium oxidation state, where a larger energy difference corresponds to a lower oxidation state. The values expected for the V^{3+}, V^{4+}, and V^{5+} are 14.7, 14.2, and 12.8 eV, respectively. The oxidation state in the fully delithiated state is expected to be 5+, and in the fully lithiated state, it is expected to be 3+. A combination of these two extremes was used as a first approximation to fit the data. Using SOXPES and HAXPES, it was shown the vanadium was gradually oxidized to a non-redox active V^{5+} state during cycling, starting from the surface and extending further into the bulk after 50 cycles.

3.2 Oxygen redox activity

The Li-rich layered oxides are attractive cathode materials for next-generation LIBs due to their high reversible specific capacity (>250 mA h g^{-1}). However, the origin of their abnormal capacity of the Li-rich layered oxides is still ambiguous; oxygen loss and/or oxygen redox reactions have been proposed to

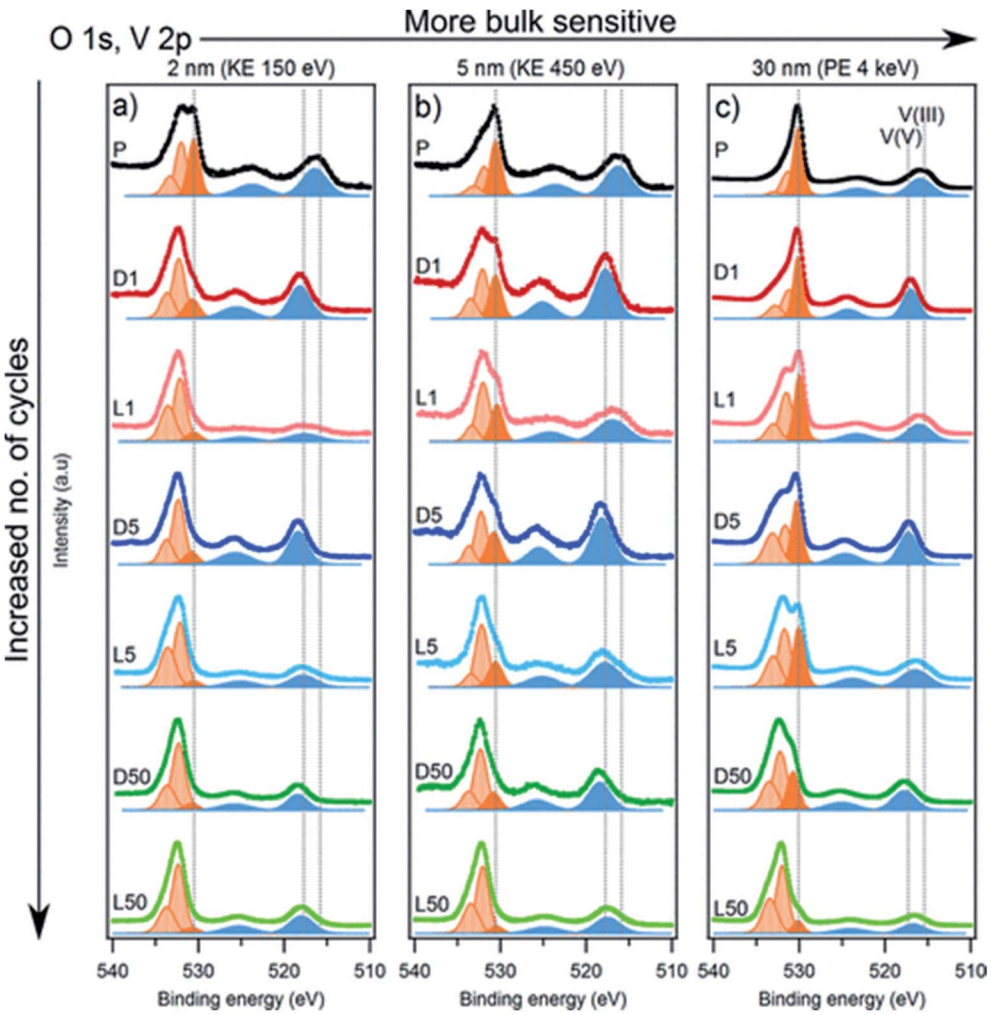

Fig. 20 The spectra of O 1s, V 2p with the tuned photon energies aiming at detecting the different depths ranging from interphase layer to bulk part. Vanadium contribution is indicated by blue peaks while dark orange corresponds to the MO and light orange to surface oxygen compounds. Reproduced under CC-BY licence from ref. 115.

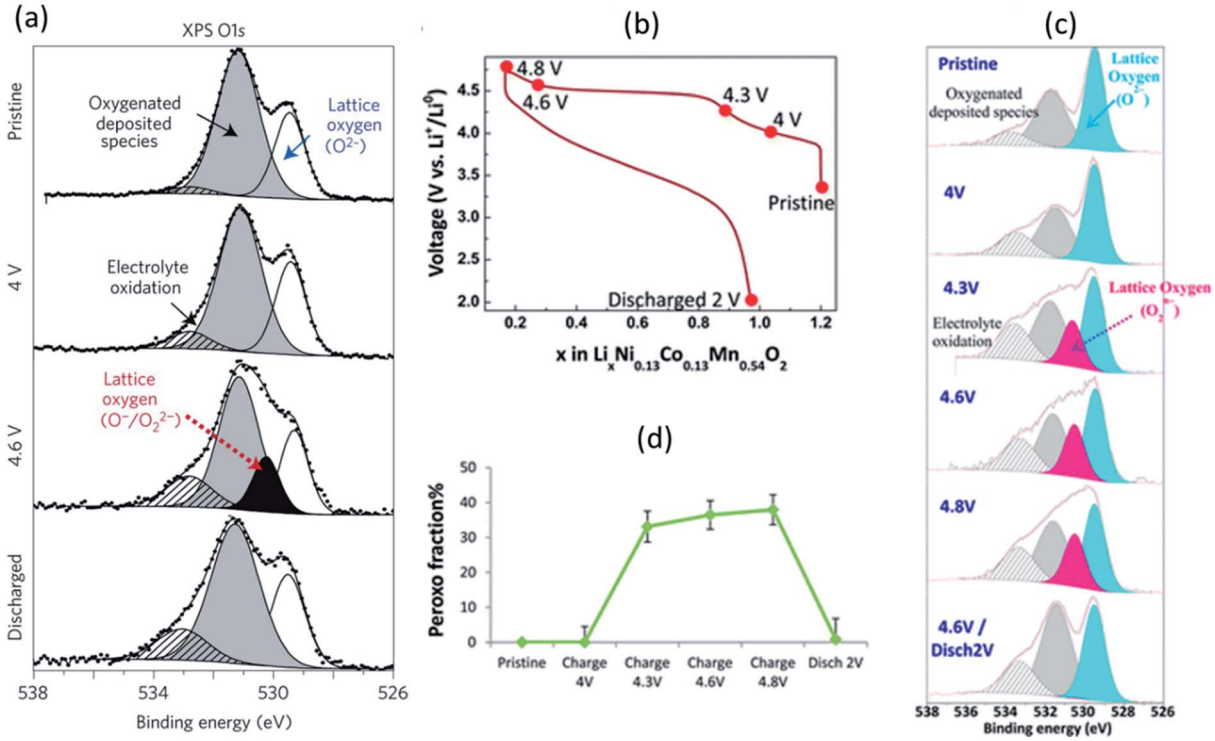

Fig. 21 XPS spectra ($h\nu = 1487$ eV) of (a) O 1s core level for $Li_2Ru_{0.5}Sn_{0.5}O_3$ with, from top to bottom, the spectra collected for the pristine electrode and the electrodes charged to 4 V, 4.6 V, and discharged to 2.0 V. The first charge/discharge of $Li_{1.2}Ni_{0.13}Co_{0.13}Mn_{0.54}O_2$: (c) voltage profile over the first cycle, (b) XPS core peaks O 1s, (c) fraction of lattice oxygen attributed to peroxo-like species. Reprinted by permission from Nature Materials (Copyright 2013) ref. 169. Reproduced under CC-BY licence from ref. 166.

explain the phenomenon.[164,165] XPS has been employed to reveal the evolution process of oxygen in various Li-rich materials.[89,166,167]

A systematic XPS study combining core and valence spectra at different stages of the charge/discharge process was performed to analyse the redox chemistry of Li-rich $Li_2Ru_{1-y}Mn_yO_3$ and $Li_2Ru_{1-y}Sn_yO_3$ where electronic changes affect both oxygen and the transition metals.[168,169] Fig. 21a shows the O 1s core spectrum with two peaks at 529.5 and 531.6 eV corresponding to O^{2-} anions belonging to the crystalline network and corresponding to weakly adsorbed surface species, respectively, the latter being also responsible for the weak signal at ~533.2 eV. The component at 530.5 eV reappears/disappears on subsequent charges/discharges, demonstrating the redox activity of oxygen. Consequently, such a mechanism is proposed with help of XPS results for Li-rich oxides. On oxidation, the reaction Ru^{6+}–$O^{2-} \rightarrow Ru^{5+} + O^-$ (*i.e.* hole in the oxygen) ultimately ends by the condensation of O_2^{2-} (peroxo-like) species, instead of releasing O_2 gas.

The anionic redox process alongside the first cycle of Li-rich layered oxide $Li_{1.2}Ni_{0.13}Co_{0.13}Mn_{0.54}O_2$ at different states of charge/discharge (Fig. 21b) was also investigated by XPS.[166] The evolution of O 1s core peaks are shown in Fig. 21c. No change from the pristine electrode to 4 V occurs, while the characteristic peroxo-like component (a new peak at 530.5 eV) is identified at 4.3, 4.6, and 4.8 V. Upon discharge, the peroxo-like signature disappears and, as compared to the pristine, a similar shape of the spectrum is restored, with only some more oxygenated deposited species. These results are consistent with a redox activity of oxygen and support that oxidation of oxide ions occurs just before and during the high-voltage plateau. It can be seen that a significant involvement of the oxygen lattice is observed through XPS for $Li_{1.2}Ni_{0.13}Co_{0.13}Mn_{0.54}O_2$ electrode with a peroxo contribution, and the relative portion of peroxo-like species is provided in Fig. 21d.

Apart from in-house XPS measurements, HAXPES is a very helpful technique to understand the redox evolution of the lattice oxygen, since the chemical state information on the lattice structure buried beneath the surface-oxygenated products can be effectively detected due to its deeper probing depth.[170,171] By virtue of HAXPES analysis, Shimoda *et al.* confirmed the formation of O^- ions as bulk oxygen species in the Li-rich $Li[Li_{0.25}Ni_{0.20}Mn_{0.55}]O_{1.93}$ material during initial charge/discharge processes.[172] Overall, all these works demonstrate that XPS is a powerful tool for understanding cationic/anionic redox mechanisms in high-capacity electrode materials.

4 *In situ* and *operando* XPS measurements

4.1 All-solid-state batteries

4.1.1 Interfaces in all-solid-state batteries. The concept of all-solid-state batteries (ASSBs) is attracting a lot of interest nowadays. Indeed, the safety of such batteries would be largely

enhanced as no flammable or toxic liquid electrolyte would be used. It is also expected that the use of purely metallic anodes (Li, Na, Mg, *etc.*) could be facilitated as the solid electrolyte would potentially inhibit the propagation of dendrites and thus greatly increase the specific capacity of such devices. Lastly, solid electrolytes were assumed to be more chemically and electrochemically stable than liquid electrolytes which turned out to be a poor assumption as the many chemistries developed nowadays come with a broad range of stability.[173,174]

As described in the previous sections, the interfaces between the electrolyte and the electrodes and the formed interphases are crucial in the battery function and durability. In the case of solid electrolytes, four kinds of interphases can be described:

- The stable interphase: an interface between the solid electrolyte and the electrode where no reactions occur.
- The mixed conducting interphase (MCI): in this case the solid electrolyte reacts with the electrode and forms an interphase having both good electronic and ionic conductivity. It can be considered unstable as electron transfer will allow a continuous growth of the interphase.
- The solid electrolyte interphase (SEI): in this case the solid electrolyte also reacts with the electrode but the formed interphase has a poor electronic conductivity and an ionic conductivity high enough to allow a good functioning of the battery. The low electronic conductivity generally makes this interphase electrochemically stable, but not necessarily mechanically or chemically stable.
- The blocking interphase: an interphase with a too low ionic conductivity that would lead to the battery failing.

From these four interphases, only three are functional: the stable interphase, the MCI and the SEI, which are illustrated in Fig. 22. It is clear that the interfaces in ASSBs need to be well understood but they are difficult to access by surface-sensitive techniques and their analysis is mainly restricted to electrochemical measurements which are chemically unspecific. XPS is therefore a technique of choice to characterise them. Indeed, the advantage of ASSBs compared to standard batteries using liquid electrolytes is that they can be stable under ultra-high vacuum that is often needed for XPS analysis. In this part we review various XPS studies as applied to ASSBs.

4.1.2 *Ex situ* measurements. The interphases between the solid electrolyte and the electrodes can be observed *ex situ* by disassembling cells. For instance, to study the reaction of a solid electrolyte with Li metal, one of the most common techniques is to put both in contact for a certain time, subsequently remove the Li metal and analyse the interphase. Yang *et al.* studied the reaction of $La_{0.56}Li_{0.33}TiO_3$ (LLTO) with Li. They observed the same spin–orbit splitting of the La $3d_{5/2}$ and La $3d_{3/2}$ binding energies in LLTO before and after reaction. The binding energies of the Li 1s electrons (61.69 eV) before and after the reaction were the same too. After reaction with lithium, they observed the reduction of Ti^{4+} to Ti^{3+} with the $2p_{3/2}$ core level shifting to lower energy. The amount of Ti^{4+} stabilised because it was limited to a certain amount of A-sites in the stable perovskite structure.[176] Auvergniot *et al.* also studied a solid electrolyte with *ex situ* XPS. They studied the argyrodite Li_6PS_5Cl electrolyte interphase in different cells. They had to mechanically etch the cells to expose the areas of interest. They showed that in a $LiCoO_2$ (LCO)/Li_6PS_5Cl/$Li_4Ti_5O_{12}$ (LTO) full cell, no electrolyte degradation happens at the interface with LTO. On the contrary, at the interface with LCO, the electrolyte is oxidised to form LiCl and P_2S_5 (see Fig. 23).[177] They also studied full cells using NMC and $LiMn_2O_4$ cathodes and Li–In anode. The oxidation of argyrodite was also observed but this time they determined that it decomposes into different P_2S_x species and LiCl. In the case of the cell using NMC cathode, the electrolyte decomposition seemed to stabilise after a few cycles and the capacity remained stable up to 300 cycles.[178] They observed that this oxidation of the electrolyte was partly reversible as also observed by Han *et al.* with $Li_{10}GeP_2S_{12}$.[179] Wu *et al.*, tested the stability of Li_3PS_4 with Li, Li–In alloy and LTO electrodes.[180] They observed the reduction of Li_3PS_4 with both Li and Li–In alloy. This reduction formed mainly Li_2S. They also determined that Li_3PS_4 was stable with LTO. Koerver *et al.* also tested the stability of Li_3PS_4 but they tried with NMC that has a higher potential than LTO. They observed the formation of a redox active interphase. The thickness of that interphase changed depending on the cut-off voltage. The interphase was made by polymerization of the electrolyte and possible formation of $Li_2P_2S_6$, $Li_4P_2S_7$ and $Li_4P_2S_8$.[181]

These examples show that *ex situ* XPS is interesting to understand the interphases in ASSBs. However, *ex situ* analyses suffer from experimental limitations. Various relaxation processes can occur after the reaction of the electrolyte with the

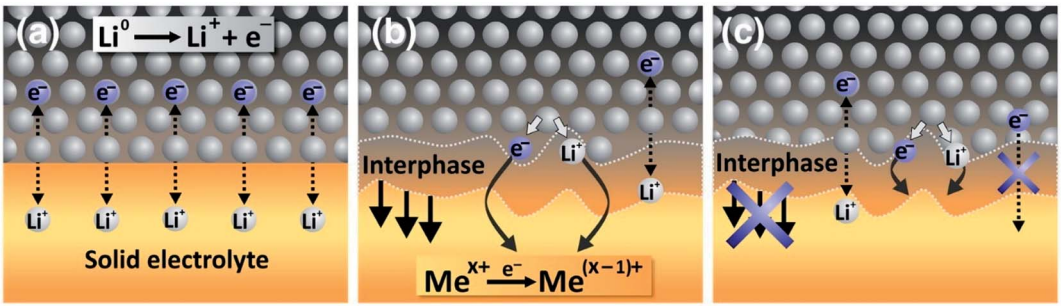

Fig. 22 Interphases in ASSBs. (a) The stable interphase. (b) The mixed conducting interphase (MCI). (c) The solid electrolyte interphase (SEI). Reprinted from ref. 175, with permission from Elsevier.

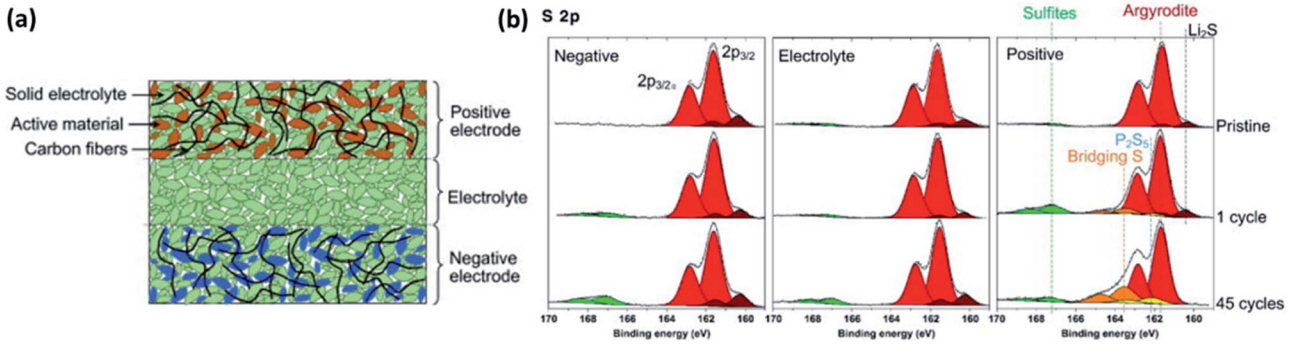

Fig. 23 (a) Scheme of a typical all-solid-state cell. (b) XPS measurements of the different parts of all-solid-state cell after different number of electrochemical cycling. Reprinted from ref. 177, with permission from Elsevier.

electrode material. The samples can also be contaminated during their preparation. Finally, using several samples for different states of charge or time of contact with an electrode, may lead difficulties in energy calibration and component assignment.[182] To overcome these drawbacks, different strategies are available as follows.

4.1.3 ***In vacuo*** **measurements.** An efficient and clean way to study the interphase between a solid electrolyte and an electrode is to form this interphase and analyse it *in vacuo*. This kind of measurements can be done with systems combining deposition chambers for electrode material that are directly connected to the analysis chamber, such as DAISY-BAT (DArmstadt Integrated SYstem for BATtery Research) illustrated in Fig. 24. This technique cannot be defined exactly as *in situ* XPS because the samples still need to be transferred from the deposition chamber to the analysis unit and the interphase can already change during this time. Jacke *et al.* studied the interphase between $LiCoO_2$ and LiPON (lithium phosphorus oxynitride) with *in vacuo* XPS.[183] They used the DAISY-MAT (DArmstadt Integrated SYstem for MATerials Research) system that is similar to the DAISY-BAT. Their work showed that an interphase was formed between $LiCoO_2$ and LiPON and contained species such as NO_2^- and NO_3^-. They could determine that the thickness of this layer was about 10 Å. The same group

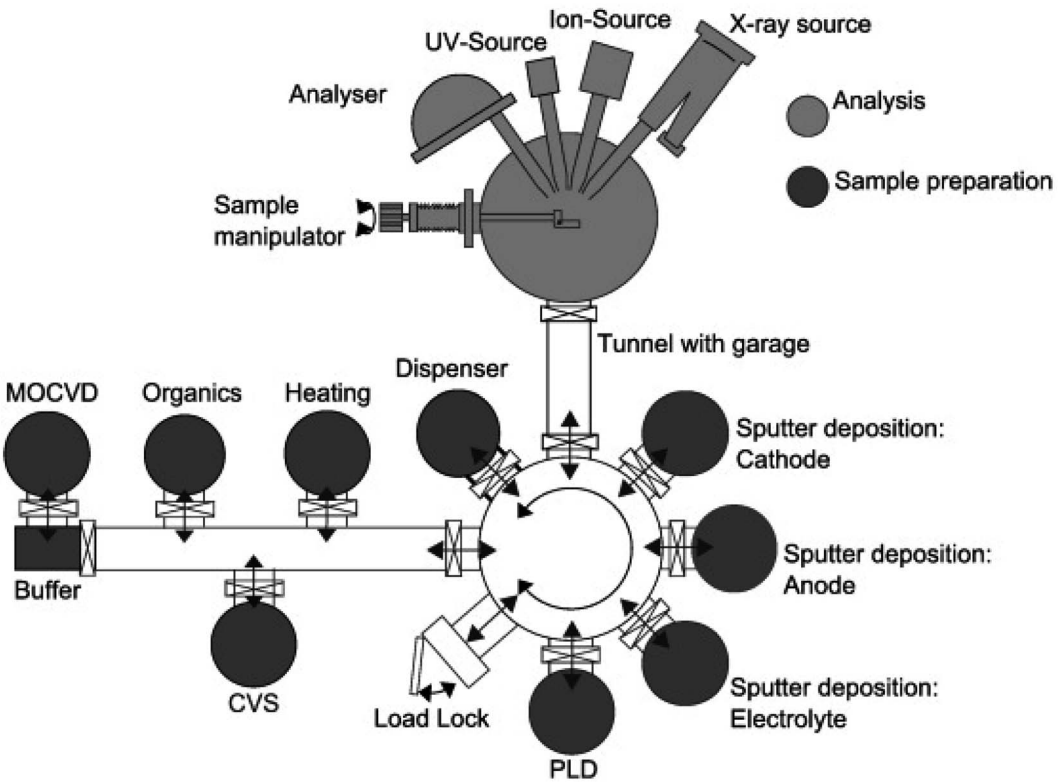

Fig. 24 Example of *in vacuo* system with the DAISY-BAT having its deposition chambers connected to an XPS analysis unit, all being under vacuum. Reprinted from ref. 188, with permission from Elsevier.

observed that by deposing the LiPON layer at different temperatures, the valence band offset changed from 0.65 eV at 200 °C to 1.15 eV at room temperature. This change was attributed to different valence band edges due to a different chemical structure of LiPON when deposited at different temperature.[184] Schwöbel *et al.* used DAISY-BAT to study the interphase between LiPON and Li metal.[188] They showed that LiPON reacted with Li to form Li_3PO_4, Li_3P, Li_3N and Li_2O. Other groups have been using similar *in vacuo* systems to characterise the different layers of micro-batteries during their fabrication.[185] Liu *et al.* studied the interface of Ga-doped LLZO ($Li_{6.4}Ga_{0.2}La_3Zr_2O_{12}$) with Li. To study this interface, they vapour-deposited a thin layer of Li metal (~1 nm) on a pellet of Ga-doped LLZO. They observed the reduction of the solid electrolyte and the formation of Li_2O. They also observed that Li metal did not react extensively, meaning that the interface is very stable.[186] Andersson *et al.* also used an *in vacuo* system at BESSY synchrotron. They could use a deposition chamber to deposit a fresh layer of Li at the surface of three different polymer electrolytes: PEO:LiTFSI, polycaprolactone (PCL):LiTFSI and poly(trimethylene carbonate) (PTMC):LiTSI. They observed similar decomposition products for the different electrolytes, such as Li–O–R (where R is an alkyne chain), $Li_xS_yO_z$ Li_2O, LiF and Li_3N. However, these decomposition products exhibited varying ratios, depending on the electrolyte composition. Polymer degradation is preferred for PCL:LiTFSI, while degradation of the salt dominates for PEO:LiTFSI and PTMC:LiTFSI.[187]

4.1.4 ***In situ* measurements.** The idea behind *in situ* XPS for ASSBs is to sputter a thin layer of an electrode active material on a fresh sample of solid electrolyte in the same chamber as where the analysis is performed. A first report of this technique was made by Hartmann *et al.* in 2013.[189] The experimental set-up to perform *in situ* XPS can be applicable to most standard spectrometers, it is illustrated in Fig. 25. An ion gun, typically used for depth profiling, is employed in this case to sputter a target material onto the surface of a sample. The sample holder is modified to add a target holder angled at 85° relative to the sample surface. First, the position for sputtering has to be found. The sputtering gun is initially targeting the centre of the sample holder. With a geometrical calculation, the position needed to sputter the target can be found. Of course, the layer that will be deposited on the sample will have an inhomogeneous thickness and the sputtering rate is very low so some calibration is needed to optimize the measurements. In the work by Wenzel *et al.*, Li was sputtered onto a MgO substrate to estimate the thickness and the deposition rate of the Li layer. They could confirm the successful deposition of Li, as the signal

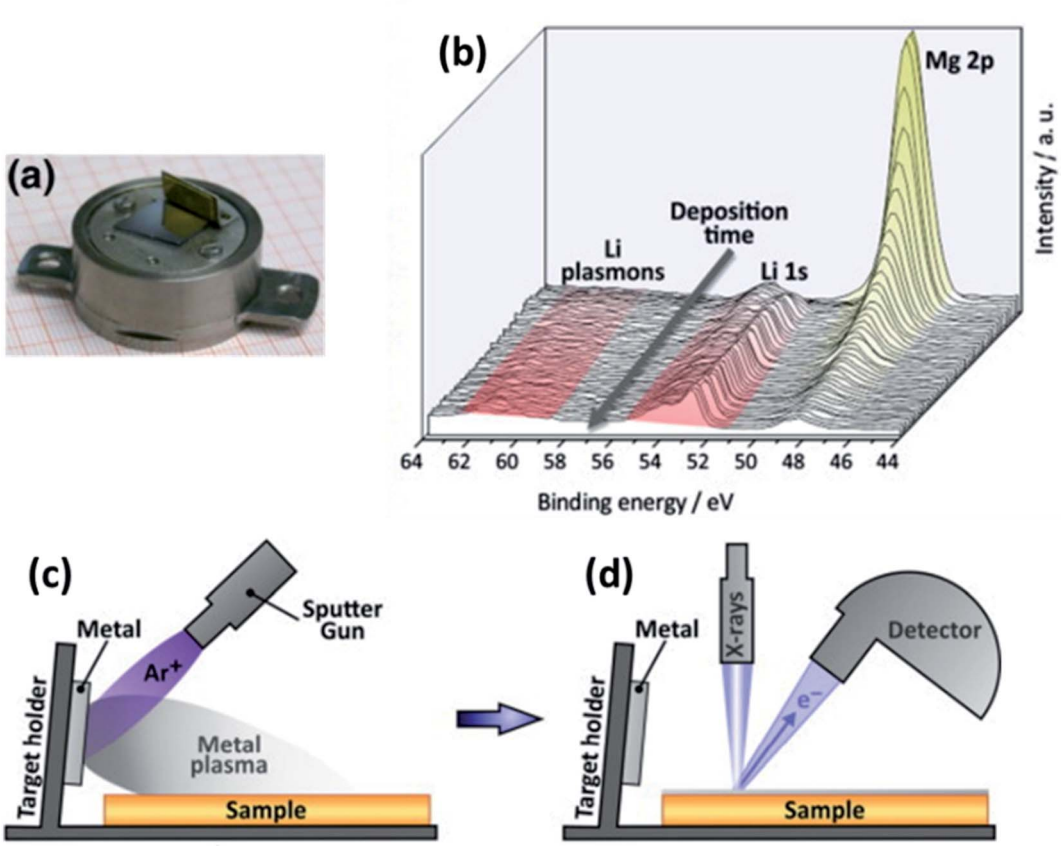

Fig. 25 An experimental set-up for *in situ* XPS. (a) Modified XPS sample holder with electrode active material target. (b) Calibration XPS measurement of Li sputtering onto MgO substrate. (c) Illustration of the *in situ* sputtering using an ion gun. (d) Illustration of the XPS analysis after *in situ* sputtering. Reprinted from ref. 175, with permission from Elsevier.

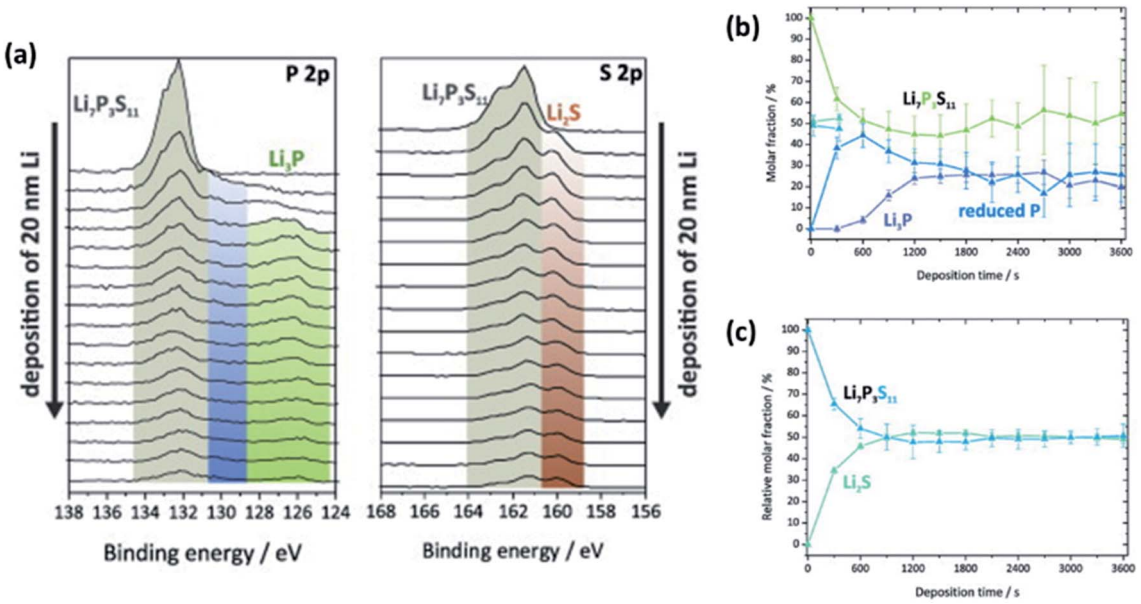

Fig. 26 (a) *In situ* XPS measurements of $Li_7P_3S_{11}$ solid electrolyte on which Li is deposited. Relative molar fractions of (b) phosphorus and (c) sulphur species for different times of Li deposition. Reprinted from ref. 192, with permission from Elsevier.

of Li 1s increases and that of Mg 2p decays. Using the practical electron effective attenuation length for Mg 2p electrons in Li they could determine the thickness of the Li layer obtained, and its deposition rate (see Fig. 25).[175]

Wenzel *et al.* studied LLTO by the described *in situ* methodology. They first observed the intensity of the signal from LLTO decreasing because of the deposition of a thin layer of Li. Nevertheless, the signal of Li 1s from Li metal was not detected meaning that the atoms of Li reacted rapidly with the solid electrolyte. Only the Ti 2p signal was affected during the Li deposition. The modification of the Ti 2p signals was due to the reduction of Ti passing from Ti^{4+} to lower oxidation states Ti^{3+}, Ti^{2+} and Ti^0. They could quantify each of these species and show that while Ti^{3+} and Ti^{2+} were reaching a maximum, Ti^{4+} was constantly decreasing and Ti^0 increasing. It confirmed the solid electrolyte reduction by Li metal. The *ex situ* observation of the solid electrolyte reduction showed only the formation of Ti^{3+}, meaning that the simple contact of LLTO with Li was insufficient to observe the complete reaction. The reduction of LLTO leads to the formation of an interphase with higher electronic conductivity; this was confirmed by alternating current impedance spectroscopy. This interphase is an MCI and it explained why LLTO is so unstable *versus* Li.[175] It is line with previous observation from Yang *et al.*[176] This first example shows that *in situ* XPS coupled with other techniques such as impedance spectroscopy is powerful to determine the stability of an interphase. Wenzel *et al.* studied also $Li_{10}GeP_2S_{12}$ (LGPS).[190] They first used electrochemical measurements, including time-resolved impedance spectroscopy, to observe the evolution of the interphase between the solid electrolyte and the Li electrode. Two resistance-constant phase element (R//CPE) components were used in series to model the ionic conductivity of the solid electrolyte and the interphase. When they extracted the resistance of the interphase they saw that it increased very fast at the beginning, and thereafter slowing down. This observation indicated a fast formation of the interphase. With cyclic voltammetry, they measured the polarisation resistance at different times and observed the same behaviour as with impedance spectroscopy. They also performed *in situ* XPS to get more information about the interphase. The sample was cooled done to between −80 °C and −90 °C to avoid release of sulphur in the ultra-high vacuum environment and also to slow down the interfacial reactions. They could clearly see the reduction of Ge, P and S. Ge might be reduced to Ge metal or Li–Ge alloy, but the lack of data on these compounds made it hard to be conclusive. P was reduced forming Li_3P which is unstable. S was forming Li_2S which is the most common degradation product of sulphide-based electrolytes. Interestingly, they could quantify the amount of the different species upon Li deposition. The amount of reduced P was constantly increasing while Li_2S increased at first before stabilising. With the combination of time-resolved electrochemical measurement and *in situ* XPS, they could determine the formation rate and the composition of the interphase of LGPS with Li. They could say that this interphase grew fast and was thick because of the formation of metallic species enhancing the electronic percolation through it. It formed an MCI. An MCI was also observed for $Li_{1.6}Al_{0.5}Ge_{1.5}(PO_4)_3$ (LAGP), $Li_{1.6}Al_{0.5}Ti_{0.95}Ta_{0.5}(PO_4)_3$ (LATTP), and a commercial Ti- and Ge-containing material for the same reasons.[189,191] Similarly, Wenzel *et al.* studied $Li_7P_3S_{11}$. Performing time-resolved impedance spectroscopy on a $Li/Li_7P_3S_{11}/Li$ symmetrical cell, a resistance increase was seen, indicative of interphase formation. However, the resistance eventually reaches a stable value meaning that the interphase reached a kinetic equilibrium. To perform the XPS measurements, the sample was cooled down to −80 °C to

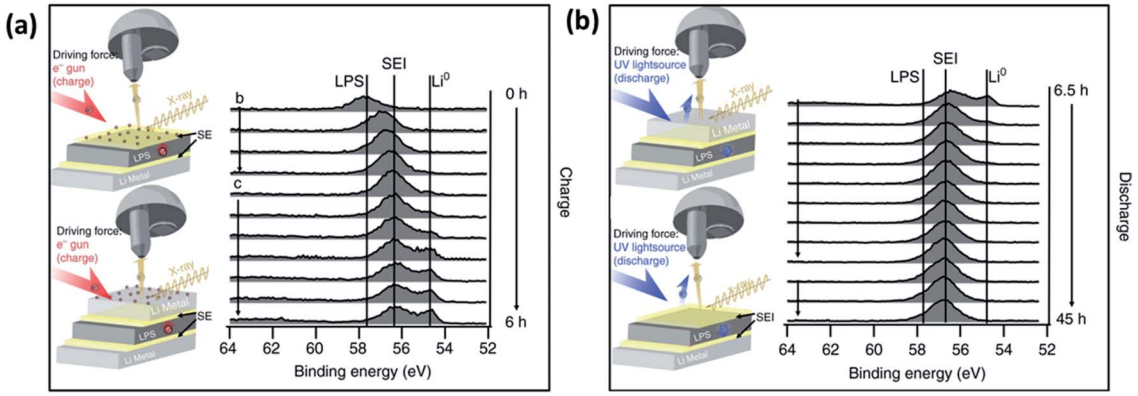

Fig. 27 *In situ* XPS set-up using a "virtual electrode" and the resulting spectra in (a) charge and (b) discharge. Reprinted from ref. 196, under a CC-BY license.

avoid sulphur sublimation. They observed the reduction of $Li_7P_3S_{11}$ with the formation of Li_2S and Li_3P (see Fig. 26). Their quantities increase fast before reaching a stable value. This stabilisation can be explained by the fact that the formed interphase was mainly made of Li_2S which has poor ionic and electronic conductivity. These results matched the electrochemical ones and showed that the interphase between $Li_7P_3S_{11}$ and Li metal can be considered as a stable SEI.[192] The same group also studied Na_3PS_4. They showed electrochemically that the interphase resistance increased significantly, becoming the dominant contribution of the overall resistance after 10 h of contact with Na metal. The XPS measurements showed that the quantity of decomposition products, Na_2S and Na_3P, increases and seems to approach a limit but no saturation was reached during the time of measurement which might be due to the sluggish reaction kinetics at low temperature. There was also a large error for the quantification of P because of its small quantity and low photoionisation cross-section.[193] They showed as well that Na-β″-Al_2O_3 is perfectly stable *versus* Na metal.[193] Zhang *et al.* showed that $Na_3Zr_2Si_2PO_{12}$ would form a stable SEI with Na. In their study, only a small amount of Zr and Si got reduced. The stabilisation of the interphase was also shown by impedance spectroscopy. After 15 min of contact between $Na_3Zr_2Si_2PO_{12}$ and Na, the interphase resistance stabilised and remained stable up to 30 days.[194] The *in situ* XPS technique was also used to study the reaction between LiPSON and Li. It was observed that upon Li deposition, the signal for P and N decreased while that for Li_2O and Li_2S increased. From this, it could be concluded that the interphase that was formed in this case consists mainly of Li_2O and Li_2S rather than Li_3N and Li_3P as in the case of LiPON.[188,195]

Wood *et al.* proposed a different *in situ* XPS technique using what they called a "virtual electrode" (see Fig. 27). They build a cell made of Li_3PS_4 solid electrolyte pressed on a Li foil. Then they used a flux of low-energy electrons to attract Li^+ ions at the bare electrolyte surface where they were reduced. This layer of Li could be removed applying UV photons ejecting valence electrons from Li metal. The formation of Li^+ at the surface drove the Li^+ migration towards the Li foil on the back of the stack. Using this technique, they could show the formation of an interphase made of Li_2S and Li–P species but they had a problem of oxygen contamination.[196]

4.1.5 *Operando* measurements. Some studies have demonstrated very challenging *operando* XPS measurements.[197–199] Of course, ASSBs have the advantage to resist ultra-high vacuum, even though it was discussed previously that sulphide-based solid electrolytes might need to be cooled down to avoid sulphur sublimation. Still, the fabrication of cells that can be cycled inside the analysis chamber of the XPS instrument remains a challenge as it can be difficult already not under *operando* conditions. Secondly, if the investigator tries to characterise an interphase, this interphase cannot be determined from the side of a cell as the analyser spot area is often large and would collect signal from other components of the battery. The interphase needs to be on a large surface facing the analyser. For instance, to look at the interphase between an active material and the solid electrolyte, the analyser should face the top of a composite electrode made of SE, active material and carbon additive to have both good electronic and ionic conductivity. Jaegermann *et al.* designed a sample holder for micro batteries shown in Fig. 28a. The sample holder could be improved to have a better electrical contact with the cathode as it can have low electronic conductivity which would induce an inhomogeneous current density.[200] Wu *et al.* developed an advanced cell allowing the cycling of an ASSB under pressure (Fig. 28b). This is needed to obtain better electrochemical cycling. The ASSB is previously pressed in an isolative cylinder which is then placed between the two current collectors. One of the current collectors is the XPS sample holder grounded to the spectrometer and the second one has a slit to allow direct measurement of the electrode underneath.[182]

In 2000, Tonti *et al.* performed *operando* XPS measurements by coating Na-β″-Al_2O_3 on TiS_2. They cycled the cell using a thin graphite layer as counter electrode. They observed the intercalation of Na and after several cycles, the irreversible formation of Na_2S and some Na metal.[201] Tonti *et al.* repeated the experiment and this time they tried to measure the electrochemical potential of the TiS_2 electrode from the XPS measurements.

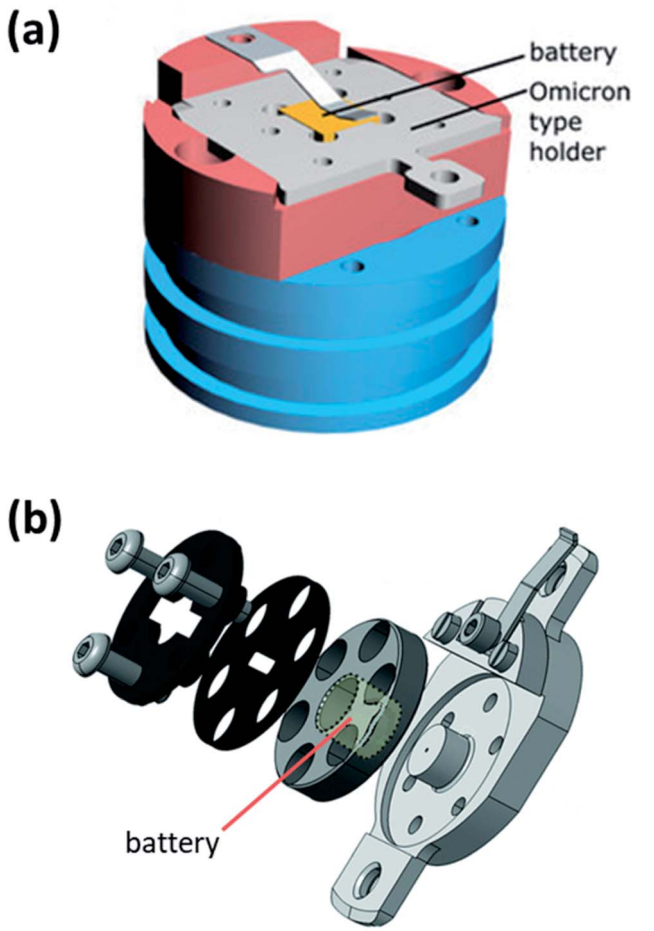

Fig. 28 Different set-ups used for operando XPS. (a) Sample holder for micro-batteries. Reprinted from ref. 200, with permission from AIP Publishing. (b) Sample holder for bulk ASSBs. Reprinted from ref. 182.

They used the shift of the binding energy upon cycling to determine a chemical potential of the Na ions and could correlate it with the actual potential of the TiS_2 electrode.[202] The same group prepared an ASSB using a pellet of homemade NASICON ($Na_{3.3}Sc_{0.3}Zr_{1.7}(SiO_4)_2(PO_4)$) with a thin film of Na_x-CoO_2 cathode deposited by pulsed laser deposition (PLD). On the other side, a Pt counter electrode was sputtered. They observed that during cycling, the asymmetric signal due to different crystallographic positions for Na was decreasing as it was removed from the material during charge and increased again during discharge. From the Co 2p spectra, it was possible to see a shoulder growing next to the Co^{3+} signal. This shoulder was due to the formation of Co^{4+} during desodiation of the cathode. This kind of measurement allows the characterisation of the bulk active material without being affected by an SEI formation.[200] It could be corroborated with other kinds of measurements to determine the complex electrochemical mechanisms. Wu *et al.* performed *operando* XPS on a classical ASSB made of pressed stacks of the different constituents of the battery. They used a glass electrolyte made of $(Li_2S)_3$–P_2S_5 (LPS), LCO composite cathode and lithium-indium alloy as anode. The cathode was a composite electrode made of a mixture of LPS, LCO and VGCF (vapour grown carbon nanofiber). The anode was made of two parts, the In–Li alloy separated from the solid electrolyte by a composite buffer layer made of In, LPS and VGCF. They performed the measurements during potentiostatic steps because of the time required to acquire the XPS spectra (see Fig. 29). For both S 2p and P 2p spectra a shoulder was observed upon cycling. These shoulders were due to the oxidation of the solid electrolyte with the formation of polysulphides, *i.e.* change in phosphorous environment from PS_4^{3-} to P_2S_x, and the polymerization reaction of PS_4^{3-} tetrahedrons through the formation of bridging P–S–P and P–S–S–P bonds. The intensity of the shoulders decreased upon delithiation, confirming the redox-activity of the decomposition products. They also observed a shift of the binding energy upon cycling. This shift could be used to gain information on the possible overpotential experienced by the surface of the different materials in the working electrode (WE). It is interesting to note that the *operando* XPS could allow to have a quite precise idea of what is the actual potential at which the oxidation of a solid electrolyte happens as the decomposition products are directly probed. They measured a linear correlation between the applied voltage and the binding energy shift. They could determine that all the conductive species were following the applied working electrode voltage change. The solid electrolyte surface, on the other hand, did not follow the applied voltage change, as it is insulating and thus not in electronic equilibrium with the working electrode. Another experiment performed without VGCF in the working electrode showed that the LCO still did not experience an overpotential and thus a working electrode without carbon could be used to increase the energy density and decrease the decomposition of the solid electrolyte as LCO has a lower specific surface area than VGCF.[182] Liu *et al.* also performed *operando* measurements to study the interphase stability of LLZO against LFP ($LiFePO_4$). They observed a shift in binding energy proportional to the applied voltage as described by Wu *et al.* The interphase between LLZO and LFP was stable as no evolution of the spectra was observed upon cycling, even after 100 cycles.[186]

4.2 Liquid electrolyte systems

4.2.1 The importance of APXPS. While traditional UHV XPS has been an indispensable tool to gain a further understanding of the redox processes and surface reactions occurring at various battery interfaces, these measurements can only probe the solid phases, and cannot represent the 'true' battery environment. Hence, to fully understand the complex solid/liquid interfaces in a battery, there is a need for measurements at higher pressures, which would allow for probing the full interface, including also the liquid phase. Furthermore, this should ideally be combined with a setup designed for electrochemical cycling during the XPS measurements. These *in situ*/*operando* measurements would enable studies of the kinetics and dynamics of battery interphases and the interfacial processes, as compared to the static conditions during an UHV measurement.

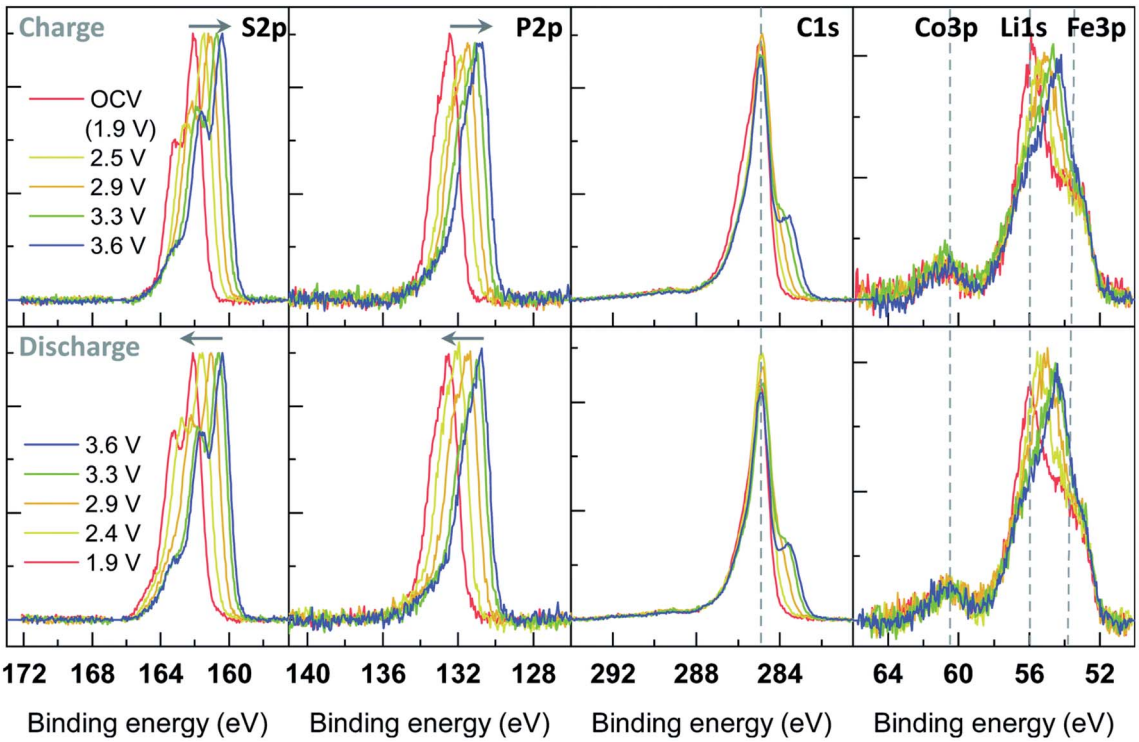

Fig. 29 Operando XPS experimental results during potentiostatic measurement of a working electrode made of 45 wt% LCO, 50 wt% amorphous $(Li_2S)_3$–P_2S_5 and 5 wt% VGCF cycled *vs.* $InLi_x$. Reprinted from ref. 182.

A first step towards achieving this was realized when XPS instruments were developed to allow for measurements at near-ambient pressures. With near-ambient pressures both gases and most liquids can be kept stable within the analysis chamber, making it possible to probe solid/gas, liquid/gas and solid/liquid interfaces of importance for many different research areas, including catalysis, environmental science and electrochemistry.[203–206] In this review focus is placed on how APXPS can be used for electrochemical applications, and in particular for the study of liquid electrolyte/electrode interfaces in batteries. Important improvements of the instruments and methodology are presented, and different methods to investigate the solid/liquid interfaces as well as important results are highlighted. Although several successful studies have already been performed on solid/liquid interfaces, these measurements remain very challenging. A continued development of the instruments and methodology is necessary to further enhance the signal from the interface, in order to facilitate *operando* measurements on 'real' batteries.

4.2.2 APXPS instrumentation and methodology development. The first XPS measurements on liquids were performed already in the 70's by the Siegbahn group.[207–209] In this setup a liquid beam kept at the vapour pressure of the liquid was used as sample, while a differential pump was used to maintain a low pressure in the electron spectrometer. In their early papers Siegbahn *et al.* lists some main requirements to probe a liquid, which are valid still today. One of the main challenges highlighted is the trade-off between high pressures and high signal-to-noise ratio for APXPS measurements. To avoid that a large percentage of the photoelectrons are scattered before detection, the distance the electrons need to travel in elevated pressures (~mbar range) has to be limited. The relation between slit aperture, maximum pressure and signal intensity is extensively discussed by Ogletree *et al.*[210] From this work, some general instrument design questions are addressed. The smaller the aperture, the higher the pressure in the analysis chamber can be. However, to avoid a large loss of photoelectrons, the aperture should be around the same size as the beam spot. Additionally, the pressure will decrease close to the aperture due to the differential pumping. This limits how close the sample can be placed to the aperture of the analyser. In this regard, the sample should be placed at a distance equal to (or longer than) two times the slit diameter, to ensure that the pressure around the sample is close to the base pressure in the chamber. From the relationships between slit width, sample distance and pressure, follows that the slit width (and thus sample distance) should be in the same order of magnitude as the IMFP of the photoelectrons to maximize the signal while keeping the desired pressure in the chamber.

Today, APXPS instruments are available both in-house[212] and at synchrotron facilities.[213] A typical instrument design is shown in Fig. 30.[211] Considering the discussion above, the aperture size R is usually in the order of 0.1–1 mm, allowing for pressures up to ~100 mbar.[214,215] Synchrotron light with well-focused beams has allowed for decreasing the slit width without losing many photoelectron counts. In addition to this, the differential pumping stages have been developed with the addition of electron lenses, to make sure the electrons are focused on the

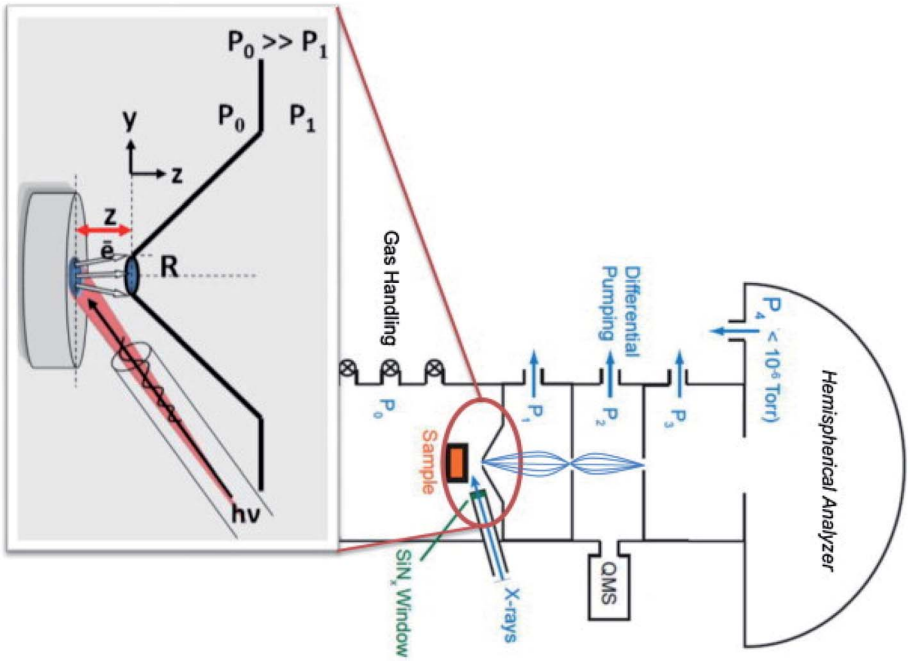

Fig. 30 A schematic illustration of an APXPS instrument. Reprinted from ref. 211, with permission from Elsevier.

analyser openings. In this way, significantly higher count rates can be realized, despite the small apertures. These developments have allowed for increasing the maximum pressures available by several orders of magnitude compared to the first instruments.[216–218]

Using this type of setup, several measurements on solid/gas and liquid/gas interfaces have been realized. However, since several of the instruments available use soft X-rays (<2000 eV) solid/liquid interfaces remains a challenge to access due to the limited IMFP of electrons through liquids (in the order of nm). Thus, to be able to probe the interface, either the liquid layer or the solid layer must be very thin. The most common approach to achieve this for electrochemical measurements is the 'dip-and-pull' approach,[214,219] where the solid sample (electrode) is immersed in the liquid (electrolyte) and then slowly pulled up to create a thin liquid meniscus.[220] If the wetting between the solid sample and the liquid is favourable (the contact angle is small) a measurement point at the end of the meniscus will exist where the liquid is thin enough to see through. An alternative way to probe the solid/liquid interface is to use a thin solid membrane that can be probed through to see also the bulk liquid.[221] In both cases, it is important that the setup can be made as realistic as possible, to gain the most useful results.

Once a solid/liquid interface has been created, the final step for *operando* measurements on batteries is to design a setup where also electrochemical measurements can be performed. This can relatively easily be realized building on the dip-and-pull method. To create an electrochemical cell, an electrolyte beaker is placed in the APXPS chamber (commonly on a bottom plate connected to a manipulator), and then three electrodes are connected to an electrode housing attached to a top manipulator. The electrode housing can then be then lowered to immerse the electrodes in the electrolyte, creating a working electrochemical cell. To create the solid/liquid interface to be measured, the electrodes are dipped in the electrolyte and then slowly retracted from the beaker. The electrode of interest (usually the working electrode) is put in front of the analyser, with the counter and reference electrode mounted behind it. This setup is schematically illustrated in Fig. 31. While APXPS instrument are becoming more commonplace, the capability of performing electrochemical measurements simultaneously is not readily available. Currently, there are only a few beamlines in the world with an electrochemical setup allowing for *operando* APXPS measurements of solid/liquid interfaces.[214,222]

4.2.3 APXPS measurements. To be able to successfully probe a solid/liquid interface, it is important to first have characterized both the solid and the liquid phases individually. Various solid electrodes used in batteries have already been thoroughly investigated by traditional ultra-high vacuum XPS. Liquid measurements of battery electrolytes are more scarce, but with the development of APXPS instruments, these measurements are becoming more common, and different electrolytes have been probed both using static droplets and liquid jet setups.[223–225]

Due to its sensitivity towards different chemical environments, APXPS is a highly useful tool to investigate the electronic structure of the solvated ions in different electrolyte solvents. El Kazzi *et al.*[224] use a liquid jet setup to show that the ion electronic structure changes as a result from different solvation environments, depending on the solvent used. Also, smaller amounts of additives can change the ion electronic structure, which can be crucial for electrical double layer (EDL) and SEI formation. In addition, Maibach *et al.*[225] investigate a static liquid droplet, and show that the presence of salt changes the

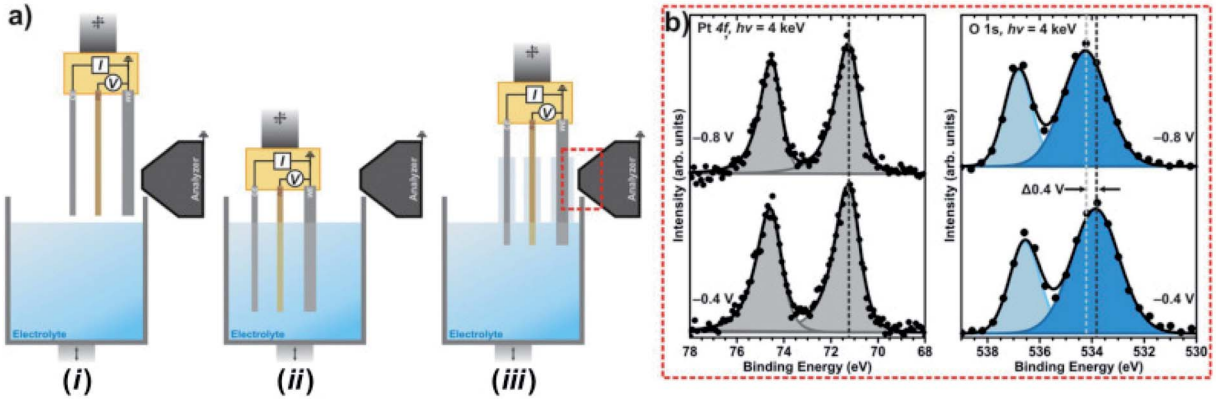

Fig. 31 (a) Illustration of the electrolyte beaker and electrode housing used for the dip-and-pull method. (b) Pt 4f and O 1s spectra recorded at two different voltages. A shift in energy is seen for the O 1s peak stemming from the electrolyte, while the Pt signal (stemming from the working electrode) remains fixed. Reproduced under CC-BY licence from ref. 214.

stability of the drop and affect the solvation of hydrocarbons. It is also seen that the ions are accumulated at the surface, forming an ion concentration gradient towards the bulk of the drop.

Since APXPS not only can probe the chemical environment and oxidation state of an element, but also changes in electron electrochemical potential differences, it is an optimal tool to study the reactions occurring in an electrochemical cell during cycling. For example, Favaro *et al.*[219] have shown that APXPS can be used to study the EDL built up at any charged surface. In this experiment a polycrystalline gold working electrode is used together with a water based 0.1–80.0 mM potassium hydroxide with 1.0 M pyrazine electrolyte. Using the dip-and-pull methodology, a thin liquid meniscus is created (~30 nm), allowing for probing the solid/liquid interface. The solid/liquid interface is probed at different applied voltages to the WE. As indicated in Fig. 32, the full width half maximum (FWHM) of the spectroscopic peaks can be correlated to the voltage drop. This is explained by a relative shift in BE of the liquid water depending on the local electrochemical potential, that will vary within the EDL. Favaro *et al.*[219] also show that the measured FWHM correlates well with electrochemical measurements of the double layer capacitance, and can also be used to localize the point of zero charge.

Another study investigating the solid/liquid interface *operando* is performed by Axnanda *et al.*[214] This study is pioneering

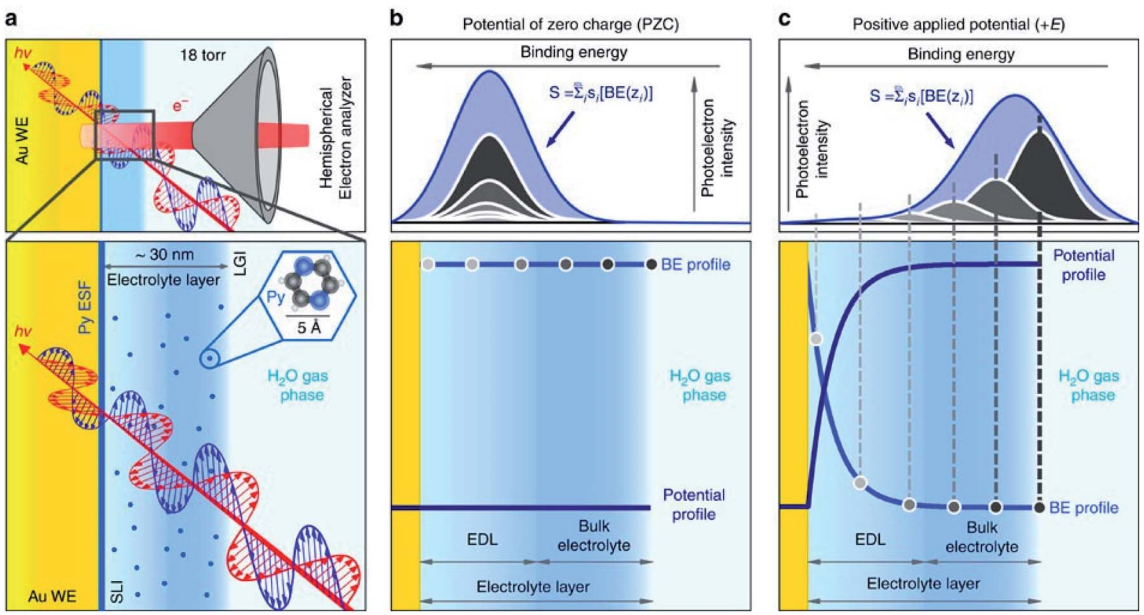

Fig. 32 (a) Schematic illustration of the measurement setup. (b) At the point of zero charge, there is no charged layer at the gold electrode/electrolyte interface, and the binding energy is the same throughout the electrolyte. (c) When a voltage is applied to the electrode, an EDL is formed, resulting in a voltage gradient over the EDL layer. This gradient can be studied by the increased FWHM of the electrolyte peak measured by APXPS. Reproduced under CC-BY licence from ref. 219.

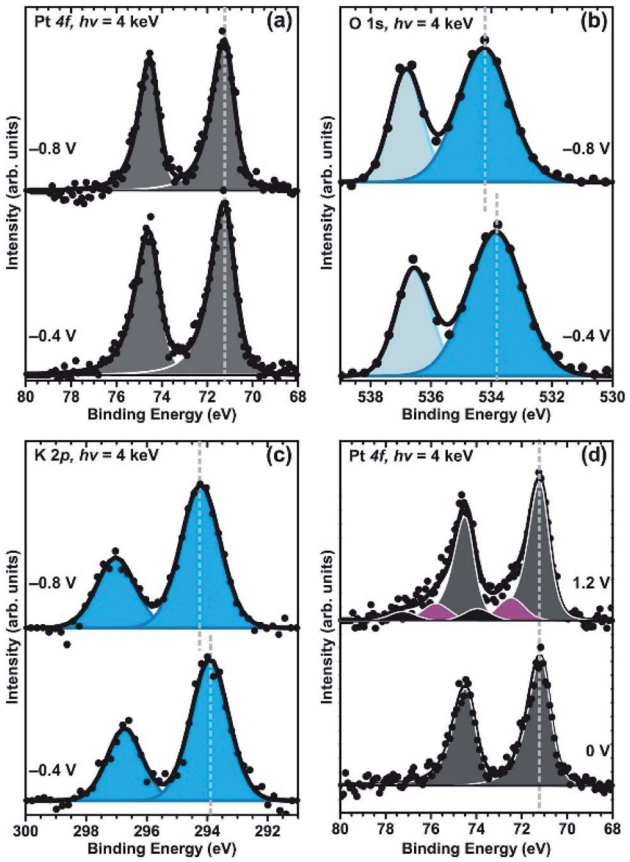

Fig. 33 APXPS spectra of Pt 4f (a) and (d) O 1s (b), and K 2p (c) core levels. The relative shifts of the electrolyte peaks (both salt and solvent) confirm the conductivity of the liquid layer, and the oxidation of the Pt electrode can be identified through the high binding energy peaks in (d). Reproduced under CC-BY licence from ref. 214.

in showing the electrochemical functionality of the thin liquid meniscus. The thickness and electrochemical properties of the liquid meniscus is in this study investigated for a platinum working electrode and a water based 6 M KF solution as electrolyte. The authors compare the intensity of the Pt peak before and after the dip-and-pull procedure to estimate the liquid layer thickness, which is calculated to 13 nm. Further, simulations of a model interface are used to estimate the optimal photon energy to maximize the signal from the interface, which in this case would be approximately 4 keV. To confirm that the electrolyte layer is conductive and in contact with the bulk electrolyte the shifts in BE of the PE peaks stemming from the electrolyte components are studied, as shown in Fig. 33(b) and (c). Finally, the functionality of the thin electrolyte layer is tested by holding the voltage of the Pt WE at an oxygen evolution reaction potential while measuring XPS *operando*. Although improvements in signal-to-noise ratio is required to fully analyse the oxidation of the platinum electrode, new higher BE peaks can be identified, as seen in Fig. 33(d), showing that the Pt can be oxidized during the APXPS measurements, and that the thin electrolyte layer is electrochemically active and functional.

From the many studies performed on SEI layers *ex situ*, it is known that these interphases are highly complex and consists of different degradation products stemming from electrode side reactions, electrolyte reduction and salt degradation. Since the interphase layer is made up by reactions between the solid and liquid, it is challenging to extract the signal stemming from the interphase, especially since the signal is attenuated by the liquid layer. To enhance the signal from the interphase as much as possible, it is useful to be able to tune the photon energy. Depending on the thickness of the liquid electrolyte layer, photon energies corresponding to tender X-rays (2–7 keV) are usually preferable.[226]

In addition, to be able to form a thin liquid layer, the contact angle between the solid and liquid has to be small. To achieve this the surface geometry as well as the sample composition is important. Hence, for some material combinations where liquid droplets are formed on the solid surface rather than thin films, it might not be possible to probe the solid/liquid interface with the dip-and-pull method. For battery materials this can be an issue for porous composite electrodes, which are generally used in commercial batteries to ensure a well-functioning ion transport. The pores improve the wetting of the material, which in the case of APXPS can cause the whole electrode to become soaked and thereby prevent probing the solid underneath the (too thick) liquid layer. This can be avoided by using dense thin film electrodes, only consisting of the active material (no conductive additives or binder). Thus, to study the solid/liquid interface directly the wetting properties need to be carefully considered.

In two recent papers by Källquist *et al.* the potential differences over the solid/liquid interface are probed for a model system,[227] and for a battery cell consisting of LTO as WE, LCO as CE and a Li metal as RE.[228] In these studies, results from probing only the liquid (not the interface) are presented and discussed. It is shown that during charge transfer over the solid/liquid interface, the shifts seen in kinetic energy of the electrolyte peaks deviates from a 1 eV/V slope, expected during EDL charging (*i.e.* when no charge transfer occurs). The results show that the electron electrochemical potential of the electrolyte is changed *versus* the RE, indicating an excess of charges in the electrolyte while the battery is cycled. It is suggested that the driving force for the change in electron electrochemical potential of the electrolyte stems from the movement of Li-ions over the interface, in order to equilibrate the Li-ion electrochemical potential. Finally, it is seen that the shifts in kinetic energy of the electrolyte peaks depend on the reactions occurring at the interface, where a phase transition reaction, single phase reaction, or pure EDL-charging gives substantially different shifts. This is illustrated in Fig. 34.

Using *operando* APXPS it is thus possible to follow the electron electrochemical potential of the electrolyte directly (which cannot be achieved by pure electrochemical measurements). Furthermore, it is possible to gain insights of the changes in Li chemical potential of the WE depending on the shifts of the electrolyte peaks as a function of WE voltage. This information can be highly useful to further understand the kinetics of the redox reactions occurring at the solid/liquid interface.

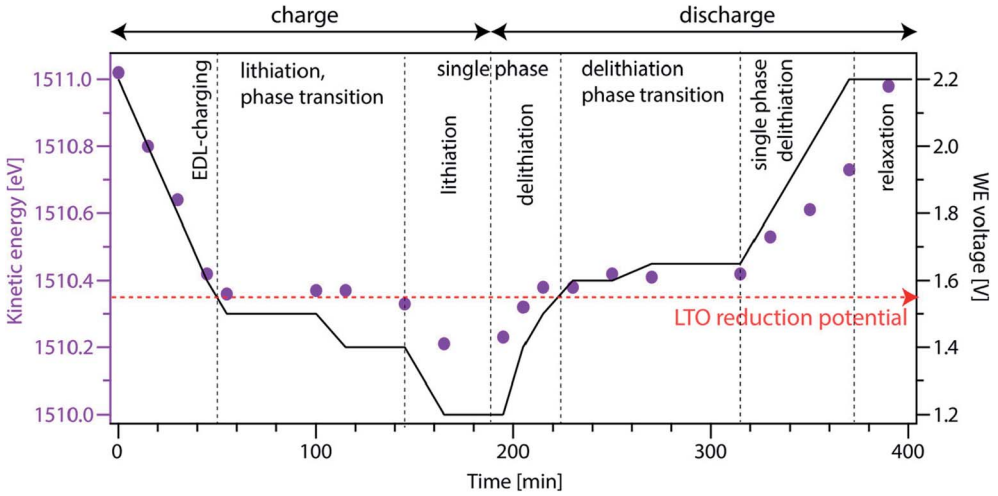

Fig. 34 Kinetic energy of the electrolyte peaks as a function of time (purple dots) and WE voltage as a function of time (black line). The kinetic energy shifts of the electrolyte are different depending on the type of reactions occurring at the WE/electrolyte interface. Reproduced under CC-BY licence from ref. 228.

So far, *operando* APXPS measurements on solid/liquid interfaces of battery systems are scarce, and recognized as highly challenging measurements due to the thickness limitation inherent to the APXPS technique, while the cell still needs to be functional from an electrochemical perspective. Today, numerous *operando* studies have been performed on solid-state batteries (see Section 4.1.5) and *operando* studies have also been successfully performed on ionic liquids (facilitated by their low vapour pressure).[229] These studies show that *operando* (AP)XPS has unique capabilities to provide information on oxidation state, potential differences and surface layer formation during battery cycling. In addition, the measurements of bulk liquid phases show that there are in principle nothing preventing *operando* APXPS studies of solid/liquid interfaces, although the slow ionic transport in a nm thin meniscus needs to be considered when interpreting the results and kinetics of the system. Proof of concept *operando* measurements have also been published in the paper by Zhu *et al.*,[222] where a thin film LCO electrode is used to successfully probe the solid/liquid interface during battery cycling using an APXPS setup at MAX IV. Based on these promising studies, it is our strong belief that these emerging measurements will become more and more common in the coming years.

5 Summary and perspectives

The use of XPS for routine measurements of battery materials has increased significantly in recent years, particularly in the past decade. This is most definitely a result of increasing research focus within the battery field, but likely also due to a realisation that interfacial studies of batteries are necessary in understanding their performance and to advance the knowledge. XPS has proven itself to be the go-to technique for battery interface studies. A basic characterisation of battery materials already comes with its own challenges, especially involving some important considerations to make when measuring samples *ex situ* (*i.e.* sample storage, washing). However, many XPS instruments allow for more complicated experiments to be performed as well, including angle-resolved XPS and sputter-etching. Therefore, XPS has been shown to be a highly versatile and multi-faceted technique that can be used to explore battery materials in a number of different ways.

In this review we have focused on some of the experimental and analysis considerations that should be made, especially for battery materials that are often very reactive when exposed to the atmosphere and due to their often-complex composite structures. We have opted to present a snapshot of the latest uses of XPS in the advancing lithium-ion battery field, as well as how it is helping to overcome challenges posed by new technologies beyond lithium-ion. For many such technologies, XPS is an invaluable tool to study the interfacial reactions of electrodes when in contact with the electrolyte. This is especially true for the upcoming SIBs, which suffer from instabilities at the interfaces much more than what is considered for LIBs.

XPS offers the possibility to gain a large amount of information about a sample, covering not only the chemical composition, structure and thickness of a surface layer, but also oxidation states of transition metals and other elements in the bulk material structure. Depth profiles studying both the surface and bulk regions can be created using various methodologies, but particularly interesting is to use synchrotron radiation where the photon energy can be varied to probe multiple depths. This expands the information gained about the sample to determine, for example, the structure of a surface layer or to understand the charge compensation mechanisms for an active material.

The technique itself is also under constant development, and innovative new *in situ* or *operando* methodologies to study solid-state batteries present exciting ways to advance the understanding of how materials in such systems function and what are their limitations. Likewise, for liquid electrolyte systems, ambient-pressure methodologies being developed

offer an excellent way to study the fundamental reactions between electrode materials and various components of a liquid electrolyte.

The use of XPS to study battery materials and the development of the technique itself is helping to advance the battery field and push the limits of existing and next-generation technologies. It is helping to answer questions about battery interfaces, both from a very fundamental point of view, whilst also allowing investigations from a highly applied and industrial perspective. It is expected that work from both standpoints will become even more widespread and thorough in the future, in order to address the challenges posed with regard to battery interface chemistry. With advances in high throughput experimentation, we expect that even larger amounts of data that are collected during measurements will require novel analysis methodologies. This will likely include the use of machine learning algorithms and extensive libraries of reference compounds, as well as advanced computational methods to rationalise experimental data by prediction of interfacial reactions in batteries. This will certainly become more relevant with increasingly complex systems, which perhaps involve materials coatings, mixed/composite active materials, and electrolytes with even more components than currently. Fundamental studies of the electrolyte reactions at electrode surfaces are becoming more important than ever as we seek stable interfaces. We expect, therefore, that ambient-pressure measurements for *in situ* or *operando* experiments will become increasingly relevant and will improve the understanding of electrolyte decomposition in 'real' battery systems. Likewise, as the interest in solid-state batteries grows, *operando* XPS on such systems will become more routine. This is something, however, that still requires a large amount of development.

While we are only just seeing the initial growth of XPS studies for battery materials, there remains many avenues for continued development of the technique and potential for major breakthroughs in the battery field.

List of abbreviations

18C6 (cyclic ether)	1,4,7,10,13,16-Hexaoxacyclooctadecane
AFM	Atomic force microscopy
ALS	Advanced light source
APXPS	Ambient-pressure X-ray photoelectron spectroscopy
ASSB	All-solid-state battery
BE	Binding energy
BESSY	Berlin electron storage ring society for synchrotron radiation
C222 (cyclic ether)	4,7,13,16,21,24-Hexaoxa-1,10-diazabicyclo hexacosane
CE	Counter electrode
CEI	Cathode electrolyte interphase
CVS	Chemical vapour synthesis
CPE	Constant phase element
DAISY-BAT	DArmstadt Integrated SYstem for BATtery Research
DAISY-MAT	DArmstadt Integrated SYstem for MATerials Research
DEC	Diethyl carbonate
DMC	Dimethyl carbonate
EC	Ethylene carbonate
EDL	Electrical double layer
EDS	Energy-dispersive X-ray spectroscopy
EELS	Electron energy loss spectroscopy
EMC	Ethyl methyl carbonate
ESCA	Electron spectroscopy for chemical analysis
EXAFS	Extended X-ray absorption fine structure
FEC	Fluoroethylene carbonate
FWHM	Full width half maximum
FY	Fluorescence yield
G1	Monoglyme; dimethoxyethane
G2	Diglyme; bis(2-methoxyethyl) ether
G3	Triglyme; triethylene glycol dimethyl ether
G4	Tetraglyme; tetraethylene glycol dimethyl ether
GCIS	Gas cluster ion sputtering
GI-XRD	Grazing incidence X-ray diffraction
GPE	Gel polymer electrolyte
HAXPES	Hard X-ray photoelectron spectroscopy
IHP	Inner Helmholtz plane
IMFP	Inelastic mean free path
KIB	Potassium-ion battery
LAGP	$Li_{1.6}Al_{0.5}Ge_{1.5}(PO_4)_3$
LATTP	$Li_{1.6}Al_{0.5}Ti_{0.95}Ta_{0.5}(PO_4)_3$
LCO	$LiCoO_2$
LFP	$LiFePO_4$
LGPS	$Li_{10}GeP_2S_{12}$
LIB	Lithium-ion battery
LiBOB	Lithium bis(oxalato)borate
LiODFB	Lithium difluoro(oxalato)borate
LiPON	Lithium phosphorus oxynitride
LiPSON	Lithium phosphorous sulfuric oxynitride
LLTO	$La_{0.56}Li_{0.33}TiO_3$
LLZO	$Li_7La_3Zr_2O_{12}$
LNMO	$LiNi_{0.5}Mn_{1.5}O_4$
LPS	$(Li_2S)_3$–P_2S_5
LTO	$Li_4Ti_5O_{12}$
MCI	Mixed conducting interphase
MOCVD	Metal organic chemical vapour deposition
NASICON	$Na_{3.3}Sc_{0.3}Zr_{1.7}(SiO_4)_2(PO_4)$
NCA	$LiNi_{1-x-y}Co_xAl_yO_2$
NMC	$LiNi_{1-x-y}Co_xMn_yO_2$
OCV	Open circuit voltage
OHP	Outer Helmholtz plane
PAN	Polyacrylonitrile
PC	Propylene carbonate
PCL	Polycaprolactone
PEO	Polyethylene oxide
PES	Photoelectron spectroscopy
PLD	Pulsed laser deposition
PTMC	Poly(trimethylene carbonate)
PVDF	Polyvinylidene fluoride
PVN	Poly(vinylene carbonate-acrylonitrile)
RE	Reference electrode
SEI	Solid electrolyte interphase
SEM	Scanning electron microscopy

SIB	Sodium-ion battery
SOXPES	Soft X-ray photoelectron spectroscopy
SPE	Solid polymer electrolyte
SPM	Scanning probe microscopy
TEM	Transmission electron microscopy
TEY	Total electron yield
TFSA	Bis(trifluoromethylsulfonyl)amide
TFSI	Bis(trifluoromethanesulfonyl)imide
TMSPi	Tris(trimethylsilyl) phosphite
ToF-SIMS	Time of flight – secondary ion mass spectrometry
TPP-2M	Equation of Tanuma, Powell, and Penn
UHV	Ultra-high vacuum
VC	Vinylene carbonate
VGCF	Vapour grown carbon nanofibres
WE	Working electrode
XANES	X-ray absorption near-edge structure
XAS	X-ray absorption spectroscopy
XPS	X-ray photoelectron spectroscopy
XRR	X-ray reflectivity

Conflicts of interest

There are no conflicts of interest to declare.

Acknowledgements

The authors acknowledge funding from the BIG-MAP project. This project has received funding from the European Union's Horizon 2020 research and innovation programme under grant agreement No. 957189. The project is part of BATTERY 2030+, the large-scale European research initiative for inventing the sustainable batteries of the future. Financial support from ST and UP for Energy to the Ångström Advanced Battery Centre is also acknowledged.

References

1 H. D. Yoo, E. Markevich, G. Salitra, D. Sharon and D. Aurbach, *Mater. Today*, 2014, **17**, 110–121.
2 J. B. Goodenough and K. S. Park, *J. Am. Chem. Soc.*, 2013, **135**, 1167–1176.
3 T. Placke, R. Kloepsch, S. Dühnen and M. Winter, *J. Solid State Electrochem.*, 2017, **21**, 1939–1964.
4 J. Xu, F. Lin, M. M. Doeff and W. Tong, *J. Mater. Chem. A*, 2017, **5**, 874–901.
5 A. Manthiram, J. C. Knight, S.-T. Myung, S.-M. Oh and Y.-K. Sun, *Adv. Energy Mater.*, 2016, **6**, 1501010.
6 E. Peled and S. Menkin, *J. Electrochem. Soc.*, 2017, **164**, A1703–A1719.
7 J. Li, C. Ma, M. Chi, C. Liang and N. J. Dudney, *Adv. Energy Mater.*, 2015, **5**, 1401408.
8 Y. Xiao, Y. Wang, S.-H. Bo, J. C. Kim, L. J. Miara and G. Ceder, *Nat. Rev. Mater.*, 2020, **5**, 105–126.
9 A. El Kharbachi, O. Zavorotynska, M. Latroche, F. Cuevas, V. Yartys and M. Fichtner, *J. Alloys Compd.*, 2020, **817**, 153261.
10 C. P. Grey and D. S. Hall, *Nat. Commun.*, 2020, **11**, 6279.
11 Y. Tian, G. Zeng, A. Rutt, T. Shi, H. Kim, J. Wang, J. Koettgen, Y. Sun, B. Ouyang, T. Chen, Z. Lun, Z. Rong, K. Persson and G. Ceder, *Chem. Rev.*, 2021, **121**, 1623–1669.
12 M. Á. Muñoz-Márquez, D. Saurel, J. L. Gómez-Cámer, M. Casas-Cabanas, E. Castillo-Martínez and T. Rojo, *Adv. Energy Mater.*, 2017, **7**, 1700463.
13 A. J. Naylor, M. Carboni, M. Valvo and R. Younesi, *ACS Appl. Mater. Interfaces*, 2019, **11**, 45636–45645.
14 A. Ponrouch, J. Bitenc, R. Dominko, N. Lindahl, P. Johansson and M. R. Palacin, *Energy Storage Mater.*, 2019, **20**, 253–262.
15 R. Dominko, J. Bitenc, R. Berthelot, M. Gauthier, G. Pagot and V. Di Noto, *J. Power Sources*, 2020, **478**, 229027.
16 M. T. Lee, H. Liu and D. Brandell, *Batteries Supercaps*, 2020, **3**, 1370–1376.
17 M. A. Rahman, X. Wang and C. Wen, *J. Electrochem. Soc.*, 2013, **160**, A1759–A1771.
18 C. R. Birkl, M. R. Roberts, E. McTurk, P. G. Bruce and D. A. Howey, *J. Power Sources*, 2017, **341**, 373–386.
19 K. Edström, T. Gustafsson and J. O. Thomas, *Electrochim. Acta*, 2004, **50**, 397–403.
20 A. M. Tripathi, W. N. Su and B. J. Hwang, *Chem. Soc. Rev.*, 2018, **47**, 736–751.
21 R. Hausbrand, G. Cherkashinin, M. Fingerle and W. Jaegermann, *J. Electron Spectrosc. Relat. Phenom.*, 2017, **221**, 65–78.
22 A. J. Cowan and L. J. Hardwick, *Annu. Rev. Anal. Chem.*, 2019, **12**, 323–346.
23 M. Gauthier, T. J. Carney, A. Grimaud, L. Giordano, N. Pour, H. H. Chang, D. P. Fenning, S. F. Lux, O. Paschos, C. Bauer, F. Maglia, S. Lupart, P. Lamp and Y. Shao-Horn, *J. Phys. Chem. Lett.*, 2015, **6**, 4653–4672.
24 J. Lu, T. Wu and K. Amine, *Nat. Energy*, 2017, **2**, 17011.
25 T. Waldmann, A. Iturrondobeitia, M. Kasper, N. Ghanbari, F. Aguesse, E. Bekaert, L. Daniel, S. Genies, I. J. Gordon, M. W. Löble, E. De Vito and M. Wohlfahrt-Mehrens, *J. Electrochem. Soc.*, 2016, **163**, A2149–A2164.
26 Y. Yuan, K. Amine, J. Lu and R. Shahbazian-Yassar, *Nat. Commun.*, 2017, **8**, 1–14.
27 J. Wu, M. Fenech, R. F. Webster, R. D. Tilley and N. Sharma, *Sustainable Energy Fuels*, 2019, **3**, 1623–1646.
28 M. Mirolo, D. Leanza, L. Höltschi, C. Jordy, V. Pelé, P. Novák, M. El Kazzi and C. A. F. Vaz, *Anal. Chem.*, 2020, **92**, 3023–3031.
29 I. V. Veryovkin, C. E. Tripa, A. V. Zinovev, S. V. Baryshev, Y. Li and D. P. Abraham, *Nucl. Instrum. Methods Phys. Res., Sect. B*, 2014, **332**, 368–372.
30 T. Sui, B. Song, J. Dluhos, L. Lu and A. M. Korsunsky, *Nano Energy*, 2015, **17**, 254–260.
31 S. M. Bak, Z. Shadike, R. Lin, X. Yu and X. Q. Yang, *NPG Asia Mater.*, 2018, **10**, 563–580.
32 P. Ghigna and E. Quartarone, *JPhys Energy*, 2021, **3**, 032006.
33 S. M. Bhaway, Z. Qiang, Y. Xia, X. Xia, B. Lee, K. G. Yager, L. Zhang, K. Kisslinger, Y. M. Chen, K. Liu, Y. Zhu and B. D. Vogt, *ACS Nano*, 2017, **11**, 1443–1454.

34 A. V. Llewellyn, A. Matruglio, D. J. L. Brett, R. Jervis and P. R. Shearing, *Condens. Matter*, 2020, **5**, 1–28.
35 C. Cao, H. G. Steinrück, B. Shyam, K. H. Stone and M. F. Toney, *Nano Lett.*, 2016, **16**, 7394–7401.
36 H. Rensmo and H. Siegbahn, *Chimia*, 2015, **69**, 22–29.
37 C. J. Powell and A. Jablonski, *Nucl. Instrum. Methods Phys. Res., Sect. A*, 2009, **601**, 54–65.
38 C. J. Powell and A. Jablonski, *NIST Electron Inelastic-Mean-Free-Path Database, Version 1.2, SRD 71*, National Institute of Standards and Technology, Gaithersburg, MD, 2010.
39 B. F. Spencer, S. Maniyarasu, B. P. Reed, D. J. H. Cant, R. Ahumada-Lazo, A. G. Thomas, C. A. Muryn, M. Maschek, S. K. Eriksson, T. Wiell, T. L. Lee, S. Tougaard, A. G. Shard and W. R. Flavell, *Appl. Surf. Sci.*, 2021, **541**, 148635.
40 C. Kalha, N. K. Fernando, P. Bhatt, F. O. L. Johansson, A. Lindblad, H. Rensmo, L. Z. Medina, R. Lindblad, S. Siol, L. P. H. Jeurgens, C. Cancellieri, K. Rossnagel, K. Medjanik, G. Schonhense, M. Simon, A. X. Gray, S. Nemsak, P. Lomker, C. Schlueter and A. Regoutz, *J. Phys.: Condens. Matter*, 2021, **33**, 233001.
41 T. L. Lee and D. A. Duncan, *J. Synchrotron Radiat.*, 2018, **31**, 16–22.
42 O. Sambalova, E. Billeter, J. Mann, T. Miyayama, D. Burnat, A. Heel, D. Bleiner and A. Borgschulte, *Surf. Interface Anal.*, 2020, **52**, 811–817.
43 K. Ciosek Högström, *The Complex Nature of the Electrode/Electrolyte Interfaces in Li-ion Batteries: Towards Understanding the Role of Electrolytes and Additives Using Photoelectron Spectroscopy*, PhD thesis, Uppsala University, 2014.
44 M. R. Linford, V. S. Smentkowski, J. T. Grant, C. R. Brundle, P. M. A. Sherwood, M. C. Biesinger, J. Terry, K. Artyushkova, A. Herrera-Gómez, S. Tougaard, W. Skinner, J. J. Pireaux, C. F. McConville, C. D. Easton, T. R. Gengenbach, G. H. Major, P. Dietrich, A. Thissen, M. Engelhard, C. J. Powell, K. J. Gaskell and D. R. Baer, *Microsc. Microanal.*, 2019, **26**, 1–2.
45 D. R. Baer, K. Artyushkova, C. Richard Brundle, J. E. Castle, M. H. Engelhard, K. J. Gaskell, J. T. Grant, R. T. Haasch, M. R. Linford, C. J. Powell, A. G. Shard, P. M. A. Sherwood and V. S. Smentkowski, *J. Vac. Sci. Technol., A*, 2019, **37**, 031401.
46 B. Philippe, M. Hahlin, K. Edström, T. Gustafsson, H. Siegbahn and H. Rensmo, *J. Electrochem. Soc.*, 2016, **163**, A178–A191.
47 V. Shutthanandan, M. Nandasiri, J. Zheng, M. H. Engelhard, W. Xu, S. Thevuthasan and V. Murugesan, *J. Electron Spectrosc. Relat. Phenom.*, 2019, **231**, 2–10.
48 A. M. Haregewoin, A. S. Wotango and B. J. Hwang, *Energy Environ. Sci.*, 2016, **9**, 1955–1988.
49 E. Peled, *J. Electrochem. Soc.*, 1979, **126**, 2047–2051.
50 X. Yu and A. Manthiram, *Energy Environ. Sci.*, 2018, **11**, 527–543.
51 E. Peled, D. Golodnitsky and G. Ardel, *J. Electrochem. Soc.*, 1997, **144**, L208–L210.
52 K. Edström, M. Herstedt and D. P. Abraham, *J. Power Sources*, 2006, **153**, 380–384.
53 E. Peled, *J. Power Sources*, 1983, **9**, 253–266.
54 R. Jung, R. Morasch, P. Karayaylali, K. Phillips, F. Maglia, C. Stinner, Y. Shao-Horn and H. A. Gasteiger, *J. Electrochem. Soc.*, 2018, **165**, A132–A141.
55 W. M. Dose, I. Temprano, J. P. Allen, E. Björklund, C. A. O'Keefe, W. Li, B. L. Mehdi, R. S. Weatherup, M. F. L. De Volder and C. P. Grey, *ACS Appl. Mater. Interfaces*, 2022, **14**, 13206–13222.
56 K. W. Schroder, H. Celio, L. J. Webb and K. J. Stevenson, *J. Phys. Chem. C*, 2012, **116**, 19737–19747.
57 S. Malmgren, K. Ciosek, R. Lindblad, S. Plogmaker, J. Kühn, H. Rensmo, K. Edström and M. Hahlin, *Electrochim. Acta*, 2013, **105**, 83–91.
58 A. Sharafi, S. Yu, M. Naguib, M. Lee, C. Ma, H. M. Meyer, J. Nanda, M. Chi, D. J. Siegel and J. Sakamoto, *J. Mater. Chem. A*, 2017, **5**, 13475–13487.
59 D. Aurbach, I. Weissman, A. Schechter and H. Cohen, *Langmuir*, 1996, **12**, 3991–4007.
60 J. D. Schneider, D. B. Agocs and A. L. Prieto, *Chem. Mater.*, 2020, **32**, 8091–8096.
61 F. A. Stevie, R. Garcia, J. Shallenberger, J. G. Newman and C. L. Donley, *J. Vac. Sci. Technol., A*, 2020, **38**, 063202.
62 S. Rensfelt, *XPS-analysis of the SEI in lithium batteries: An investigation of the effect of storage on the solid electrolyte interphase of lithium ion batteries*, Bachelor thesis, Uppsala University, 2017.
63 R. Mogensen, D. Brandell and R. Younesi, *ACS Energy Lett.*, 2016, **1**, 1173–1178.
64 L. A. Ma, A. J. Naylor, L. Nyholm and R. Younesi, *Angew. Chem., Int. Ed.*, 2021, **60**, 4855–4863.
65 M. Moshkovich, Y. Gofer and D. Aurbach, *J. Electrochem. Soc.*, 2001, **148**, E155.
66 L. Somerville, J. Bareño, P. Jennings, A. McGordon, C. Lyness and I. Bloom, *Electrochim. Acta*, 2016, **206**, 70–76.
67 R. Fong, U. von Sacken and J. R. Dahn, *J. Electrochem. Soc.*, 1990, **137**, 2009–2013.
68 P. Verma, P. Maire and P. Novák, *Electrochim. Acta*, 2010, **55**, 6332–6341.
69 S. Malmgren, K. Ciosek, M. Hahlin, T. Gustafsson, M. Gorgoi, H. Rensmo and K. Edström, *Electrochim. Acta*, 2013, **97**, 23–32.
70 S. Mukherjee, P. K. Santra and D. D. Sarma, *Hard X-ray Photoelectron Spectroscopy (HAXPES)*, Springer International Publishing, Cham, 2016, vol. 59.
71 C. Weiland, A. K. Rumaiz, P. Pianetta and J. C. Woicik, *J. Vac. Sci. Technol., A*, 2016, **34**, 030801.
72 B. Philippe, R. Dedryvère, J. Allouche, F. Lindgren, M. Gorgoi, H. Rensmo, D. Gonbeau and K. Edström, *Chem. Mater.*, 2012, **24**, 1107–1115.
73 K. Ciosek Högström, S. Malmgren, M. Hahlin, H. Rensmo, F. Thébault, P. Johansson and K. Edström, *J. Phys. Chem. C*, 2013, **117**, 23476–23486.
74 D. Leinen, A. Fernández, J. P. Espinós and A. R. González-Elipe, *Surf. Interface Anal.*, 1993, **20**, 941–948.

75 G. Panzner, B. Egert and H. P. Schmidt, *Surf. Sci.*, 1985, **151**, 400–408.
76 C. Chaneliere, J. L. Autran, R. A. B. Devine and B. Balland, *Mater. Sci. Eng., R*, 1998, **22**, 269–322.
77 E. Lewin, J. Counsell and J. Patscheider, *Appl. Surf. Sci.*, 2018, **442**, 487–500.
78 N. Sanada, A. Yamamoto, R. Oiwa and Y. Ohashi, *Surf. Interface Anal.*, 2004, **36**, 280–282.
79 C. M. Goodwin, Z. E. Voras and T. P. BeebeJr, *J. Vac. Sci. Technol., A*, 2018, **36**, 051507.
80 R. Simpson, R. G. White, J. F. Watts and M. A. Baker, *Appl. Surf. Sci.*, 2017, **405**, 79–87.
81 M. A. Isaacs, J. Davies-Jones, P. R. Davies, S. Guan, R. Lee, D. J. Morgan and R. Palgrave, *Mater. Chem. Front.*, 2021, **5**, 7931–7963.
82 M. Jiang, X. Wu, Q. Zhang, D. L. Danilov, R. A. Eichel and P. H. L. Notten, *Electrochim. Acta*, 2021, **398**, 139316.
83 J. Kim, F. Buchner and R. J. Behm, *Phys. Chem. Chem. Phys.*, 2018, **20**, 18319–18327.
84 A. M. Kia, J. Speulmanns, S. Bönhardt, J. Emara, K. Kühnel, N. Haufe and W. Weinreich, *Appl. Surf. Sci.*, 2021, **564**, 150457.
85 D. R. Baer, K. Artyushkova, H. Cohen, C. D. Easton, M. Engelhard, T. R. Gengenbach, G. Greczynski, P. Mack, D. J. Morgan and A. Roberts, *J. Vac. Sci. Technol., A*, 2020, **38**, 031204.
86 G. H. Major, T. G. Avval, B. Moeini, G. Pinto, D. Shah, V. Jain, V. Carver, W. Skinner, T. R. Gengenbach, C. D. Easton, A. Herrera-Gomez, T. S. Nunney, D. R. Baer and M. R. Linford, *J. Vac. Sci. Technol., A*, 2020, **38**, 061204.
87 K. N. Wood and G. Teeter, *ACS Appl. Energy Mater.*, 2018, **1**, 4493–4504.
88 F. Lindgren, D. Rehnlund, I. Källquist, L. Nyholm, K. Edström, M. Hahlin and J. Maibach, *J. Phys. Chem. C*, 2017, **121**, 27303–27312.
89 J. Maibach, F. Lindgren, H. Eriksson, K. Edström and M. Hahlin, *J. Phys. Chem. Lett.*, 2016, **7**, 1775–1780.
90 R. Azmi, V. Trouillet, M. Strafela, S. Ulrich, H. Ehrenberg and M. Bruns, *Surf. Interface Anal.*, 2018, **50**, 43–51.
91 M. C. Biesinger, L. W. M. Lau, A. R. Gerson and R. S. C. Smart, *Appl. Surf. Sci.*, 2010, **257**, 887–898.
92 M. C. Biesinger, B. P. Payne, A. P. Grosvenor, L. W. M. Lau, A. R. Gerson and R. S. C. Smart, *Appl. Surf. Sci.*, 2011, **257**, 2717–2730.
93 A. Andersson, A. Henningson, H. Siegbahn, U. Jansson and K. Edström, *J. Power Sources*, 2003, **119–121**, 522–527.
94 H. Liu, Y. Yang and J. Zhang, *J. Power Sources*, 2006, **162**, 644–650.
95 D. P. Abraham, R. D. Twesten, M. Balasubramanian, I. Petrov, J. McBreen and K. Amine, *Electrochem. Commun.*, 2002, **4**, 620–625.
96 J. Eom, M. G. Kim and J. Cho, *J. Electrochem. Soc.*, 2008, **155**, A239.
97 X. Zheng, X. Li, Z. Wang, H. Guo, Z. Huang, G. Yan and D. Wang, *Electrochim. Acta*, 2016, **191**, 832–840.
98 N. V. Faenza, L. Bruce, Z. W. Lebens-Higgins, I. Plitz, N. Pereira, L. F. J. Piper and G. G. Amatucci, *J. Electrochem. Soc.*, 2017, **164**, A3727–A3741.
99 A. Grenier, H. Liu, K. M. Wiaderek, Z. W. Lebens-Higgins, O. J. Borkiewicz, L. F. J. Piper, P. J. Chupas and K. W. Chapman, *Chem. Mater.*, 2017, **29**, 7345–7352.
100 M. Wood, J. Li, R. E. Ruther, Z. Du, E. C. Self, H. M. Meyer, C. Daniel, I. Belharouak and D. L. Wood, *Energy Storage Mater.*, 2020, **24**, 188–197.
101 Q. Li, Y. Wang, X. Wang, X. Sun, J. N. Zhang, X. Yu and H. Li, *ACS Appl. Mater. Interfaces*, 2020, **12**, 2319–2326.
102 Z. Liu, *Acta Phys.-Chim. Sin.*, 2019, **35**, 1293–1294.
103 C. Yan, R. Xu, Y. Xiao, J. Ding, L. Xu, B. Li and J. Huang, *Adv. Funct. Mater.*, 2020, **30**, 1909887.
104 I. Takahashi, H. Kiuchi, A. Ohma, T. Fukunaga and E. Matsubara, *J. Phys. Chem. C*, 2020, **124**, 9243–9248.
105 Q. Li, Y. Wang, X. Wang, X. Sun, J. N. Zhang, X. Yu and H. Li, *ACS Appl. Mater. Interfaces*, 2020, **12**, 2319–2326.
106 H. Wang, X. Li, F. Li, X. Liu, S. Yang and J. Ma, *Electrochem. Commun.*, 2021, **122**, 106870.
107 W. Li, A. Dolocan, P. Oh, H. Celio, S. Park, J. Cho and A. Manthiram, *Nat. Commun.*, 2017, **8**, 1–10.
108 B. Huang, D. Liu, L. Zhang, K. Qian, K. Zhou, X. Cai, F. Kang and B. Li, *ACS Appl. Energy Mater.*, 2019, **2**, 7403–7411.
109 L. Madec, R. Petibon, J. Xia, J.-P. Sun, I. G. Hill and J. R. Dahn, *J. Electrochem. Soc.*, 2015, **162**, A2635–A2645.
110 C. Xu, F. Jeschull, W. R. Brant, D. Brandell, K. Edström and T. Gustafsson, *J. Electrochem. Soc.*, 2018, **165**, A40–A46.
111 A. K. Haridas, Q. A. Nguyen, T. Terlier, R. Blaser and S. L. Biswal, *ACS Appl. Mater. Interfaces*, 2021, **13**, 2662–2673.
112 H. Q. Pham, M. T. Nguyen, M. Tarik, M. El Kazzi and S. Trabesinger, *ChemSusChem*, 2021, **14**, 2461–2474.
113 Y. Li, W. Li, R. Shimizu, D. Cheng, H. N. Nguyen, J. Paulsen, S. Kumakura, M. Zhang and Y. S. Meng, *Adv. Energy Mater.*, 2022, **12**, 2103033.
114 H. Liu, A. J. Naylor, A. S. Menon, W. R. Brant, K. Edström and R. Younesi, *Adv. Mater. Interfaces*, 2020, **7**, 2000277.
115 I. Källquist, A. J. Naylor, C. Baur, J. Chable, J. Kullgren, M. Fichtner, K. Edström, D. Brandell and M. Hahlin, *Chem. Mater.*, 2019, **31**, 6084–6096.
116 I. Källquist, J. F. Martin, A. J. Naylor, C. Baur, M. Fichtner, J. F. Colin, D. Brandell, K. Edström and M. Hahlin, *J. Phys. Chem. C*, 2020, **124**, 12956–12967.
117 A. J. Naylor, I. Källquist, D. Peralta, J.-F. Martin, A. Boulineau, J.-F. Colin, C. Baur, J. Chable, M. Fichtner, K. Edström, M. Hahlin and D. Brandell, *ACS Appl. Energy Mater.*, 2020, **3**, 5937–5948.
118 C. Baur, I. Källquist, J. Chable, J. H. Chang, R. E. Johnsen, F. Ruiz-Zepeda, J.-M. Ateba Mba, A. J. Naylor, J. M. Garcia-Lastra, T. Vegge, F. Klein, A. R. Schür, P. Norby, K. Edström, M. Hahlin and M. Fichtner, *J. Mater. Chem. A*, 2019, **7**, 21244–21253.
119 C. Zhan, T. Wu, J. Lu and K. Amine, *Energy Environ. Sci.*, 2018, **11**, 243–257.
120 H. Liu, X. Zhang, X. He, A. Senyshyn, A. Wilken, D. Zhou, O. Fromm, P. Niehoff, B. Yan, J. Li, M. Muehlbauer,

J. Wang, G. Schumacher, E. Paillard, M. Winter and J. Li, *J. Electrochem. Soc.*, 2018, **165**, A1886–A1896.
121 H. Liu, J. Wang, X. Zhang, D. Zhou, X. Qi, B. Qiu, J. Fang, R. Kloepsch, G. Schumacher, Z. Liu and J. Li, *ACS Appl. Mater. Interfaces*, 2016, **8**, 4661–4675.
122 M. A. Cambaz, B. P. Vinayan, S. A. Pervez, R. E. Johnsen, H. Geßwein, A. A. Guda, Y. V. Rusalev, M. K. Kinyanjui, U. Kaiser and M. Fichtner, *Chem. Mater.*, 2019, **31**, 7941–7950.
123 M. Ochida, Y. Domi, T. Doi, S. Tsubouchi, H. Nakagawa, T. Yamanaka, T. Abe and Z. Ogumi, *J. Electrochem. Soc.*, 2012, **159**, A961–A966.
124 W. Liu, J. Li, W. Li, H. Xu, C. Zhang and X. Qiu, *Nat. Commun.*, 2020, **11**, 3629.
125 M. A. Cabañero Martínez, N. Boaretto, A. J. Naylor, F. Alcaide, G. D. Salian, F. Palombardini, E. Ayerbe, M. Borras and M. Casas-Cabanas, *Adv. Energy Mater.*, 2022, 2201264.
126 C. Sångeland, J. Mindemark, R. Younesi and D. Brandell, *Solid State Ionics*, 2019, **343**, 115068.
127 C. Xu, B. Sun, T. Gustafsson, K. Edström, D. Brandell and M. Hahlin, *J. Mater. Chem. A*, 2014, **2**, 7256–7264.
128 P. Wang, J. Chai, Z. Zhang, H. Zhang, Y. Ma, G. Xu, H. Du, T. Liu, G. Li and G. Cui, *J. Mater. Chem. A*, 2019, **7**, 5295–5304.
129 R. Rajagopalan, Y. Tang, X. Ji, C. Jia and H. Wang, *Adv. Funct. Mater.*, 2020, **30**, 1909486.
130 B. John, V. Anoopkumar and T. D. Mercy, *ACS Appl. Energy Mater.*, 2020, **3**, 9478–9492.
131 K. M. Abraham, *ACS Energy Lett.*, 2020, **5**, 3544–3547.
132 N. Tapia-Ruiz, A. R. Armstrong, H. Alptekin, M. A. Amores, H. Au, J. Barker, R. Boston, W. R. Brant, J. M. Brittain, Y. Chen, M. Chhowalla, Y. S. Choi, S. I. R. Costa, M. C. Ribadeneyra, S. A. Cussen, E. J. Cussen, W. I. F. David, A. V. Desai, S. A. M. Dickson, E. I. Eweka, J. D. Forero-Saboya, C. P. Grey, J. M. Griffin, P. Gross, X. Hua, J. T. S. Irvine, P. Johansson, M. O. Jones, M. Karlsmo, E. Kendrick, E. Kim, O. V. Kolosov, Z. Li, S. F. L. Mertens, R. Mogensen, L. Monconduit, R. E. Morris, A. J. Naylor, S. Nikman, C. A. O'Keefe, D. M. C. Ould, R. G. Palgrave, P. Poizot, A. Ponrouch, S. Renault, E. M. Reynolds, A. Rudola, R. Sayers, D. O. Scanlon, S. Sen, V. R. Seymour, B. Silván, M. T. Sougrati, L. Stievano, G. S. Stone, C. I. Thomas, M. M. Titirici, J. Tong, T. J. Wood, D. S. Wright and R. Younesi, *JPhys Energy*, 2021, **3**, 031503.
133 F. Allgayer, J. Maibach and F. Jeschull, *ACS Appl. Energy Mater.*, 2022, **5**, 1136–1148.
134 S. Kaushik, K. Kubota, J. Hwang, K. Matsumoto and R. Hagiwara, *ACS Appl. Mater. Interfaces*, 2022, **14**, 14302–14312.
135 Z. Wang, W. Zhuo, J. Li, L. Ma, S. Tan, G. Zhang, H. Yin, W. Qin, H. Wang, L. Pan, A. Qin and W. Mai, *Nano Energy*, 2022, **98**, 107243.
136 G. Zhang, J. Li, Y. Fan, Y. Liu, P. Zhang, X. Shi, J. Ma, R. Zhang and Y. Huang, *Energy Storage Mater.*, 2022, **51**, 559–567.
137 T. Hosaka, A. Noda, K. Kubota, K. Chiguchi, Y. Matsuda, K. Ida, S. Yasuno and S. Komaba, *ACS Appl. Mater. Interfaces*, 2022, **14**, 23507–23517.
138 Q. Zhang, Z. Wang, X. Li, H. Guo, W. Peng, J. Wang and G. Yan, *J. Power Sources*, 2022, **541**, 231726.
139 P. Canepa, G. Sai Gautam, D. C. Hannah, R. Malik, M. Liu, K. G. Gallagher, K. A. Persson and G. Ceder, *Chem. Rev.*, 2017, **117**, 4287–4341.
140 Y. Liang, H. Dong, D. Aurbach and Y. Yao, *Nat. Energy*, 2020, **5**, 646–656.
141 R. Mogensen, J. Maibach, W. R. Brant, D. Brandell and R. Younesi, *Electrochim. Acta*, 2017, **245**, 696–704.
142 C. Bommier, D. Leonard, Z. Jian, W. F. Stickle, P. A. Greaney and X. Ji, *Adv. Mater. Interfaces*, 2016, **3**, 1600449.
143 M. A. Muñoz-Márquez, M. Zarrabeitia, E. Castillo-Martínez, A. Eguía-Barrio, T. Rojo and M. Casas-Cabanas, *ACS Appl. Mater. Interfaces*, 2015, **7**, 7801–7808.
144 K. Li, J. Zhang, D. Lin, D. W. Wang, B. Li, W. Lv, S. Sun, Y. B. He, F. Kang, Q. H. Yang, L. Zhou and T. Y. Zhang, *Nat. Commun.*, 2019, **10**, 725.
145 P. Bai, Y. He, P. Xiong, X. Zhao, K. Xu and Y. Xu, *Energy Storage Mater.*, 2018, **13**, 274–282.
146 C. Wang, L. Wang, F. Li, F. Cheng and J. Chen, *Adv. Mater.*, 2017, **29**, 1702212.
147 J. Maibach, F. Jeschull, D. Brandell, K. Edström and M. Valvo, *ACS Appl. Mater. Interfaces*, 2017, **9**, 12373–12381.
148 Y. Lei, D. Han, J. Dong, L. Qin, X. Li, D. Zhai, B. Li, Y. Wu and F. Kang, *Energy Storage Mater.*, 2020, **24**, 319–328.
149 A. J. Naylor, M. Carboni, M. Valvo and R. Younesi, *ACS Appl. Mater. Interfaces*, 2019, **11**, 45636–45645.
150 C. Chen, M. Wu, Y. Wang and K. Zaghib, *J. Power Sources*, 2019, **444**, 227310.
151 J. D. Forero-Saboya, D. S. Tchitchekova, P. Johansson, M. R. Palacín, A. Ponrouch, J. D. Forero-Saboya, D. S. Tchitchekova, M. R. Palacín, A. Ponrouch and P. Johansson, *Adv. Mater. Interfaces*, 2022, **9**, 2101578.
152 D. Tripathy, M. H. Viswanatha, H. Makri Nimbegondi Kotresh, P. V. Babu and S. Sampath, *ACS Appl. Mater. Interfaces*, 2022, **14**, 26671–26681.
153 D. Zhang, D. Du, J. Zhang, Z. Feng and T. Sun, *J. Electrochem. Soc.*, 2022, **169**, 040530.
154 X. Wang, X. Zhang, G. Zhao, H. Hong, Z. Tang, X. Xu, H. Li, C. Zhi and C. Han, *ACS Nano*, 2022, **16**, 6093–6102.
155 M. Matsui, H. Kuwata, D. Mori, N. Imanishi and M. Mizuhata, *Front. Chem.*, 2019, **7**, 1–10.
156 S. B. Son, T. Gao, S. P. Harvey, K. X. Steirer, A. Stokes, A. Norman, C. Wang, A. Cresce, K. Xu and C. Ban, *Nat. Chem.*, 2018, **10**, 532–539.
157 A. Ponrouch, C. Frontera, F. Bardé and M. R. Palacín, *Nat. Mater.*, 2016, **15**, 169–172.
158 M. Wang, C. Jiang, S. Zhang, X. Song, Y. Tang and H. M. Cheng, *Nat. Chem.*, 2018, **10**, 667–672.
159 S. J. Richard Prabakar, A. B. Ikhe, W. B. Park, K. C. Chung, H. Park, K. J. Kim, D. Ahn, J. S. Kwak, K. S. Sohn and M. Pyo, *Adv. Sci.*, 2019, **6**, 1902129.
160 J. L. White, F. S. Gittleson, M. Homer and F. El Gabaly, *J. Phys. Chem. C*, 2020, **124**, 16508–16514.

161 Z. Zhang, X. Wang, Y. Bai and C. Wu, *Green Energy Environ.*, 2021, **7**, 606–635.
162 R. A. House, U. Maitra, L. Jin, J. G. Lozano, J. W. Somerville, N. H. Rees, A. J. Naylor, L. C. Duda, F. Massel, A. V. Chadwick, S. Ramos, D. M. Pickup, D. E. McNally, X. Lu, T. Schmitt, M. R. Roberts and P. G. Bruce, *Chem. Mater.*, 2019, **31**, 3293–3300.
163 L. A. Ma, F. Massel, A. J. Naylor, L. C. Duda and R. Younesi, *Commun. Chem.*, 2019, **2**, 125.
164 G. Assat, D. Foix, C. Delacourt, A. Iadecola, R. Dedryvère and J.-M. Tarascon, *Nat. Commun.*, 2017, **8**, 2219.
165 G. Assat and J.-M. Tarascon, *Nat. Energy*, 2018, **3**, 373–386.
166 D. Foix, M. Sathiya, E. McCalla, J.-M. Tarascon and D. Gonbeau, *J. Phys. Chem. C*, 2016, **120**, 862–874.
167 S. Han, Y. Xia, Z. Wei, B. Qiu, L. Pan, Q. Gu, Z. Liu and Z. Guo, *J. Mater. Chem. A*, 2015, **3**, 11930–11939.
168 M. Sathiya, K. Ramesha, G. Rousse, D. Foix, D. Gonbeau, A. S. Prakash, M. L. Doublet, K. Hemalatha and J.-M. Tarascon, *Chem. Mater.*, 2013, **25**, 1121–1131.
169 M. Sathiya, G. Rousse, K. Ramesha, C. P. Laisa, H. Vezin, M. T. Sougrati, M.-L. Doublet, D. Foix, D. Gonbeau, W. Walker, a S. Prakash, M. Ben Hassine, L. Dupont and J.-M. Tarascon, *Nat. Mater.*, 2013, **12**, 827–835.
170 A. J. Naylor, E. Makkos, J. Maibach, N. Guerrini, A. Sobkowiak, E. Björklund, J. G. Lozano, A. S. Menon, R. Younesi, M. R. Roberts, K. Edström, M. S. Islam and P. G. Bruce, *J. Mater. Chem. A*, 2019, **7**, 25355–25368.
171 K. Luo, M. R. Roberts, R. Hao, N. Guerrini, D. M. Pickup, Y.-S. Liu, K. Edström, J. Guo, A. V Chadwick, L. C. Duda and P. G. Bruce, *Nat. Chem.*, 2016, **8**, 684–691.
172 K. Shimoda, T. Minato, K. Nakanishi, H. Komatsu, T. Matsunaga, H. Tanida, H. Arai, Y. Ukyo, Y. Uchimoto and Z. Ogumi, *J. Mater. Chem. A*, 2016, **4**, 5909–5916.
173 T. Famprikis, P. Canepa, J. A. Dawson, M. S. Islam and C. Masquelier, *Nat. Mater.*, 2019, **18**, 1278–1291.
174 W. D. Richards, L. J. Miara, Y. Wang, J. C. Kim and G. Ceder, *Chem. Mater.*, 2016, **28**, 266–273.
175 S. Wenzel, T. Leichtweiss, D. Krüger, J. Sann and J. Janek, *Solid State Ionics*, 2015, **278**, 98–105.
176 K.-Y. Yang, I.-C. Leu, K.-Z. Fung, M.-H. Hon, M.-C. Hsu, Y.-J. Hsiao and M.-C. Wang, *J. Mater. Res.*, 2008, **23**, 1813–1825.
177 J. Auvergniot, A. Cassel, D. Foix, V. Viallet, V. Seznec and R. Dedryvère, *Solid State Ionics*, 2017, **300**, 78–85.
178 J. Auvergniot, A. Cassel, J. B. Ledeuil, V. Viallet, V. Seznec and R. Dedryvère, *Chem. Mater.*, 2017, **29**, 3883–3890.
179 F. Han, T. Gao, Y. Zhu, K. J. Gaskell and C. Wang, *Adv. Mater.*, 2015, **27**, 3473–3483.
180 X. Wu, M. El Kazzi and C. Villevieille, *J. Electroceram.*, 2017, **38**, 207–214.
181 R. Koerver, F. Walther, I. Aygün, J. Sann, C. Dietrich, W. G. Zeier and J. Janek, *J. Mater. Chem. A*, 2017, **5**, 22750–22760.
182 X. Wu, C. Villevieille, P. Novák and M. El Kazzi, *Phys. Chem. Chem. Phys.*, 2018, **20**, 11123–11129.
183 S. Jacke, J. Song, G. Cherkashinin, L. Dimesso and W. Jaegermann, *Ionics*, 2010, **16**, 769–775.
184 J. Song, S. Jacke, G. Cherkashinin, S. Schmid, Q. Dong, R. Hausbrand and W. Jaegermann, *Electrochem. Solid-State Lett.*, 2011, **14**, A189.
185 M. Haruta, S. Shiraki, T. Ohsawa, T. Suzuki, A. Kumatani, Y. Takagi, R. Shimizu and T. Hitosugi, *Solid State Ionics*, 2016, **285**, 118–121.
186 Z. Liu, G. Li, A. Borodin, X. Liu, Y. Li and F. Endres, *J. Solid State Electrochem.*, 2019, **23**, 2107–2117.
187 E. K. W. Andersson, C. Sångeland, E. Berggren, F. O. L. Johansson, D. Kühn, A. Lindblad, J. Mindemark and M. Hahlin, *J. Mater. Chem. A*, 2021, **9**, 22462–22471.
188 A. Schwöbel, R. Hausbrand and W. Jaegermann, *Solid State Ionics*, 2015, **273**, 51–54.
189 P. Hartmann, T. Leichtweiss, M. R. Busche, M. Schneider, M. Reich, J. Sann, P. Adelhelm and J. Janek, *J. Phys. Chem. C*, 2013, **117**, 21064–21074.
190 S. Wenzel, S. Randau, T. Leichtweiß, D. A. Weber, J. Sann, W. G. Zeier and J. Janek, *Chem. Mater.*, 2016, **28**, 2400–2407.
191 A. I. Inozemtseva, V. A. Vizgalov, O. O. Kapitanova, G. Panin, J. J. Velasco Vélez, D. M. Itkis, D. Y. Usachov and L. V. Yashina, *J. Electrochem. Soc.*, 2020, **167**, 110533.
192 S. Wenzel, D. A. Weber, T. Leichtweiss, M. R. Busche, J. Sann and J. Janek, *Solid State Ionics*, 2016, **286**, 24–33.
193 S. Wenzel, T. Leichtweiss, D. A. Weber, J. Sann, W. G. Zeier and J. Janek, *ACS Appl. Mater. Interfaces*, 2016, **8**, 28216–28224.
194 Z. Zhang, S. Wenzel, Y. Zhu, J. Sann, L. Shen, J. Yang, X. Yao, Y.-S. Hu, C. Wolverton, H. Li, L. Chen and J. Janek, *ACS Appl. Energy Mater.*, 2020, **3**, 7427–7437.
195 F. Michel, M. Becker, J. Janek and A. Polity, *Phys. Status Solidi A*, 2020, **257**, 1900336.
196 K. N. Wood, K. X. Steirer, S. E. Hafner, C. Ban, S. Santhanagopalan, S.-H. Lee and G. Teeter, *Nat. Commun.*, 2018, **9**, 2490.
197 M. Mirolo, X. Wu, C. A. F. Vaz, P. Novák and M. El Kazzi, *ACS Appl. Mater. Interfaces*, 2021, **13**, 2547–2557.
198 K. Hikima, K. Shimizu, H. Kiuchi, Y. Hinuma, K. Suzuki, M. Hirayama, E. Matsubara and R. Kanno, *J. Am. Chem. Soc.*, 2022, **144**, 236–247.
199 H. Kiuchi, K. Hikima, K. Shimizu, R. Kanno, F. Toshiharu and E. Matsubara, *Electrochem. Commun.*, 2020, **118**, 106790.
200 C. Guhl, P. Kehne, Q. Ma, F. Tietz, L. Alff, P. Komissinskiy, W. Jaegermann and R. Hausbrand, *Rev. Sci. Instrum.*, 2018, **89**, 073104.
201 D. Tonti, C. Pettenkofer and W. Jaegermann, *Electrochem. Solid-State Lett.*, 2000, **3**, 220–223.
202 D. Tonti, C. Pettenkofer and W. Jaegermann, *J. Phys. Chem. B*, 2004, **108**, 16093–16099.
203 L. Trotochaud, A. R. Head, O. Karslioğlu, L. Kyhl and H. Bluhm, *J. Phys.: Condens. Matter*, 2017, **29**, 053002.
204 C. H. Wu, R. S. Weatherup and M. B. Salmeron, *Phys. Chem. Chem. Phys.*, 2015, **17**, 30229–30239.
205 E. J. Crumlin, Z. Liu, H. Bluhm, W. Yang, J. Guo and Z. Hussain, *J. Electron Spectrosc. Relat. Phenom.*, 2015, **200**, 264–273.

206 X. Liu, W. Yang and Z. Liu, *Adv. Mater.*, 2014, **26**, 7710–7729.
207 H. Siegbarn, L. Asplund, P. Kelfve, K. Hamrin, L. Karlsson and K. Siegbahn, *J. Electron Spectrosc. Relat. Phenom.*, 1974, **5**, 1059–1079.
208 H. Siegbahn and K. Siegbahn, *J. Electron Spectrosc. Relat. Phenom.*, 1973, **2**, 319–325.
209 H. Siegbahn, L. Asplund, P. Kelfve and K. Siegbahn, *J. Electron Spectrosc. Relat. Phenom.*, 1975, **7**, 411–419.
210 D. F. Ogletree, H. Bluhm, G. Lebedev, C. S. Fadley, Z. Hussain and M. Salmeron, *Rev. Sci. Instrum.*, 2002, **73**, 3872.
211 E. J. Crumlin, H. Bluhm and Z. Liu, *J. Electron Spectrosc. Relat. Phenom.*, 2013, **190**, 84–92.
212 C. Arble, M. Jia and J. T. Newberg, *Surf. Sci. Rep.*, 2018, **73**, 37–57.
213 A. Shavorskiy, O. Karslioglu, I. Zegkinoglou and H. Bluhm, *J. Synchrotron Radiat.*, 2014, **27**, 14–23.
214 S. Axnanda, E. J. Crumlin, B. Mao, S. Rani, R. Chang, P. G. Karlsson, M. O. M. Edwards, M. Lundqvist, R. Moberg, P. Ross, Z. Hussain and Z. Liu, *Sci. Rep.*, 2015, **5**, 1–12.
215 J. J. Velasco-Vélez, V. Pfeifer, M. Hävecker, R. Wang, A. Centeno, A. Zurutuza, G. Algara-Siller, E. Stotz, K. Skorupska, D. Teschner, P. Kube, P. Braeuninger-Weimer, S. Hofmann, R. Schlögl and A. Knop-Gericke, *Rev. Sci. Instrum.*, 2016, **87**, 053121.
216 Y. Takagi, T. Nakamura, L. Yu, S. Chaveanghong, O. Sekizawa, T. Sakata, T. Uruga, M. Tada, Y. Iwasawa and T. Yokoyama, *Appl. Phys. Express*, 2017, **10**, 076603.
217 D. E. Starr, M. Favaro, F. F. Abdi, H. Bluhm, E. J. Crumlin and R. van de Krol, *J. Electron Spectrosc. Relat. Phenom.*, 2017, **221**, 106–115.
218 M. Salmeron and R. Schlögl, *Surf. Sci. Rep.*, 2008, **63**, 169–199.
219 M. Favaro, B. Jeong, P. N. Ross, J. Yano, Z. Hussain, Z. Liu and E. J. Crumlin, *Nat. Commun.*, 2016, **7**, 1–8.
220 W. N. Hansen, *J. Electroanal. Chem.*, 1983, **150**, 133–140.
221 R. Endo, D. Watanabe, M. Shimomura and T. Masuda, *Appl. Phys. Lett.*, 2019, **114**, 173702.
222 S. Zhu, M. Scardamaglia, J. Kundsen, R. Sankari, H. Tarawneh, R. Temperton, L. Pickworth, F. Cavalca, C. Wang, H. Tissot, J. Weissenrieder, B. Hagman, J. Gustafson, S. Kaya, F. Lindgren, I. Kallquist, J. Maibach, M. Hahlin, V. Boix, T. Gallo, F. Rehman, G. D'Acunto, J. Schnadta and A. Shavorskiy, *J. Synchrotron Radiat.*, 2021, **28**, 624–636.
223 P. M. Dietrich, L. Gehrlein, J. Maibach and A. Thissen, *Crystals*, 2020, **10**, 1–13.
224 M. El Kazzi, I. Czekaj, E. J. Berg, P. Novák and M. A. Brown, *Top. Catal.*, 2016, **59**, 628–634.
225 J. Maibach, I. Källquist, M. Andersson, S. Urpelainen, K. Edström, H. Rensmo, H. Siegbahn and M. Hahlin, *Nat. Commun.*, 2019, **10**, 3080.
226 M. Favaro, F. Abdi, E. Crumlin, Z. Liu, R. van de Krol and D. Starr, *Surfaces*, 2019, **2**, 78–99.
227 I. Källquist, F. Lindgren, M. T. Lee, A. Shavorskiy, K. Edström, H. Rensmo, L. Nyholm, J. Maibach and M. Hahlin, *ACS Appl. Mater. Interfaces*, 2021, **13**, 32989–32996.
228 I. Källquist, T. Ericson, F. Lindgren, H. Chen, A. Shavorskiy, J. Maibach and M. Hahlin, *ACS Appl. Mater. Interfaces*, 2022, **14**, 6465–6475.
229 W. Wang, Y. Wang, C. H. Wang, Y. W. Yang and Y. C. Lu, *Energy Storage Mater.*, 2021, **36**, 341–346.